Assessing Shoreline Change Associated with the Cape Jaffa Marina, South Australia

By

Marcio Daniel DaSilva

Thesis
Submitted to Flinders University
for the degree of

Masters of Geospatial Information Science
College of Science and Engineering
21/10/2019

TABLE OF CONTENTS

LIST OF FIGURES

LIST OF TABLES

SUMMARY

The coastal zone is a dynamic area which can experience substantial change in short time periods which are in turn associated with weather events and with more substantial long-term morphological trends. The monitoring of shoreline change represents a significant area of interest for coastal communities and management programs responsible for coastal preservation. This research provides a case study focused around the Cape Jaffa Marina in South Australia, assessing shoreline change associated with a constructed canal estate and adjacent coast. The research is comprised of a GIS based analysis of shoreline change utilising (i) Aerial imagery from 1975 to 2005 which provides information of the prevalent morphological coastal trends before the construction of the canal estate, (ii) satellite imagery collected by the CubeSat satellite constellations, Planetscope and RapidEye, to assess the decade since construction, and (iii) Unmanned Aerial Vehicle (UAV) surveys to assess localised morphological change. The shoreline change was assessed in the Digital Shoreline Analysis System (DSAS) extension of ESRI's ArcGIS (2019) to provide statistics on the net shoreline change and the rates of change of the past few decades. UAV surveys conducted on three separate dates provide high-resolution orthomosaics that have been used to assess shoreline change at a finer-scale (>2 cm pixel) and provide an accuracy assessment for the automated shoreline extraction from the multi-spectral satellite imagery. The results provide a case study of a historically pro-gradational sandy coastline experiencing substantial amounts of alongshore transport, the corresponding barrier effects of coastal infrastructure, and the resulting significant morphological changes to the Cape Jaffa shoreline. The image analysis workflow developed here, based on best-practice remote sensing methods, presents a potentially useful methodology to be applied for an automated shoreline change monitoring program with rapid response capability from the high spatial and temporal resolutions with a relatively low-cost data access of the CubeSat constellations.

DECLARATION

I certify that this thesis does not incorporate without acknowledgment any material previously submitted for a degree or diploma in any university; and that to the best of my knowledge and belief it does not contain any material previously published or written by another person except where due reference is made in the text.

ACKNOWLEDGEMENTS

I would like to thank my supervisors, Graziela Miot da Silva and Patrick Hesp whose guidance through this study has been immeasurably helpful. Their constructive advice and unwavering support has without a doubt made me grow to be a better person.

I'd like to further thank the Geospatial Sciences Department at Flinders University for its support, both to the staff members present and past and the whole College of Science and Engineering for its help along the way. Special thanks to David Bruce whose curious nature challenged me to continue and follow the rabbit hole that is problem solving within a research environment. Additional thanks to Robert Keane whose leadership for the GIS department has been inestimably beneficial for myself, the others who will come after me into the program and the entire geospatial industry for the state of South Australia. Thanks to Claire Moore who has graciously provided insightful opinions on all things spatial that I've been working on over the past year.

I'm incredibly grateful to Planet Labs, who provided the access to high resolution satellite imagery for this study. Thanks to the Tidal Unit of the Bureau of Meteorology for providing historical hindcast data and maintaining a world class monitoring network that is freely available to the public. Thanks to Mapland, part of the State Government of South Australia, for providing the aerial imagery from its archive.

I'd like to give special thanks to my parents whose commitment to service and positive change, both in their professional and private lives, has shown me a stalwart example of what humans should strive to be.

Finally, I'd like to publicly appreciate my partner, Jill, whose love and support has got me through these past few years. We found each other over 3 years ago in Southern Mexico and I'm so happy to have made the decision to pursue a life with her.

1. INTRODUCTION

The dynamic nature of coastal environments is a result of the interactions of normal and storm wave and wind events, storm surges and tidal behaviour (Boak & Turner, 2005). The physical structure of a beach reflects its morphological response to natural forcing including storm systems and wave energy. Moreover, the sediment budget of sandy beaches is the net amount of output and input sand into a system, where shifts of supply in the sediment budget are an environmental indicator of alterations to coastal processes (Ruiz-Beltran et al., 2019). Fluctuations in the sediment budget are attributed to natural processes and anthropogenic pressures, and influence beach morphology causing spatial shifts of the shoreline over time (Silva et al., 2014). Rapid change to the shoreline can occur as a result of extreme weather events which also represent one of the greatest threats affecting the coastal environment and local communities according to the Global Risk Report (2019). In a world where climate change is altering weather patterns and the drive for valuable real estate is further pushing coastal development, adaptive monitoring responses and understanding coastal systems needs to inform better coastal management (Nicholls et al., 2013; Sytnik et al., 2018).

Urban development of coastal areas often requires defence strategies that ensure shoreline stabilisation and proper management of the associated surf-beach-dune systems (Defeo et al., 2009). Canal and port estates represent a possibility for developers looking to maximise waterfront realty while simultaneously providing a sheltered inlet from wave energy. The practicality of their construction, management and integration within coastal and estuarine systems presents a litany of issues in both the long and short-term, challenging their economic viability and ecological harmony (Stocker et al., 2016). Studies that have explored the ecological and morphological effects of canal estates in coastal areas (Harvey & Stocker, 2015; Massey et al., 1976; Nuttal, 1991; Westman, 1975) suggest that common management issues arise from sedimentation, eutrophication, coastal stability, habitat destruction and a restriction of public access. Stocker's et al. (2016) research underlies the implicit threat that these coastal developments will face from sea level rise and the associated effects of climate change as the individual projects attempt to balance economic benefits and environmental liability issues. The management of canal estates and

coastal infrastructure relies on accurate data sets that provide measurements of detailed morphological change and estimated changes in the sediment budget to inform engineering and management responses (Turner et al., 2006). These measurements can be acquired from the historical record by analysing the past positions of shorelines and through adaptive and responsive monitoring that tracks changes after they occur.

Examination of the historical record of a coastal system offers one way to assess past behaviour and provides the basis for predictions into the future. A source of relatively recent historical data is through aerial photographs which have been widely collected since the early 20th century (Li, 2002). Various studies have successfully utilised analytical photogrammetry techniques to evaluate shoreline proxies on aerial photographs (Carrasco et al., 2012; Chaaban et al., 2012; Del Rio, 2013; Fletcher et al., 2003; Ford, 2013; González-Villanueva et al., 2012; Hapke 2013; Sytnik et al., 2018; Tsokos et al., 2018). Traditional methods for estimating the position of shoreline proxies on aerial photographs are explained by Ruggerio (2013), with geo-referencing the aerial photographs, interpreting the shoreline indicators and then digitising the shoreline position. While aerial photography provides one source of high-resolution imagery that can extend into the past, its inconsistent re-visit time (which is dependent on repeat flights) has encouraged researchers to utilise satellite systems with reliable re-visit times and on-going collection programs to monitor contemporary change (Aplin et al., 1997; Sytnik et al., 2018; Tsokos et al., 2018; Wulder et al., 2004; Yang et al., 2019).

The use of imagery collected by satellite systems has been extensively documented in studies of temporal changes in shoreline position (Fisher et al., 2016; Kelly & Gontz, 2018; Li & Gong 2016; Zhai et al., 2015). Multi-spectral satellite imagery provides data that can be evaluated to provide insights of change over time at the landscape level. Additionally, the range of data collected with multi-spectral sensors can be outside of the visible spectrum that traditional aerial photogrammetry is based on. The utilisation of sensors that collect additional electromagnetic radiation not visible to the human eye can increase the reliability and efficiency of shoreline extraction while simultaneously decreasing the subjectivity of traditional manual shoreline delineation (Liu & Jezek, 2004). Earth observation capabilities from satellites have improved significantly in terms of spectral, spatial and temporal resolution since the first Land Remote

Sensing Satellite (Landsat) was launched in 1972 (Houborg & McCabe, 2018b). Recent developments with CubeSat satellite technology have further improved the temporal and spatial resolution of imagery allowing subtle changes over short periods of time to be identified (Wicaksono & Lazuardi, 2018) and present a promising alternative to the coarser spatiotemporal resolution of established methods of large-scale monitoring of landscapes. Although the benefits from Earth observations sourced from CubeSat technology shows potential, recent studies (Cooley et al., 2017; Houborg & McCabe, 2018a; Houborg & McCabe, 2018b; Wicaksono & Lazuardi, 2018) have highlighted the limitations from utilising smaller and relatively inexpensive sensors which cannot achieve the same radiometric quality or consistency as established satellite systems. Furthermore, improvements in a multi-temporal analysis can be achieved with pre-processing steps aimed at reducing atmospheric interference (Cooley et al., 2017; Wicaksono & Hafizt, 2018). An exploration of the best practices for the specific sensors for ensuring geometric and atmospheric fidelity in a multi-temporal analysis is presented in Appendix 1.

The dynamic morphological response of coastal environments to waves and storm events (Wright & Thom, 1977) presents a challenge for traditional topographic surveys to monitor landscape scale changes (Guisado-Pintado et al., 2019). Although the conventional techniques of measuring beach change with direct and in-situ observations are a well-established method that provide relatively high accuracy results (2 to 6 cm vertical) (Casella et al., 2016; Lee et al., 2013), the advent of low-cost Unmanned Aerial Vehicle (UAV) technology provides a repeatable technique of measuring coastal morphology that provides similar levels of accuracy (Casella et al., 2016). Additionally, UAVs can cover a wider area in a shorter period of time in comparison to land based surveys and produce high-resolution images that can be further compiled and analysed with photogrammetric techniques. The past decade has seen widespread use of UAVs to collect high-resolution imagery that is then utilised to create 3D representations of landscapes or high-resolution 2D imagery for further analysis (Colomina & Molina, 2014; Drummond et al., 2015). One product of UAV surveys is the generation of high-resolution orthomosaic images, with pixel sizes varying with camera specifications and flight height (James et al., 2017). Researchers have produced image mosaics with <2 cm pixel sizes, suitable for monitoring local changes with a high degree of accuracy (Clark, 2017; Duffy et al., 2018). Recent research has utilised drones for

numerous coastal surveying projects such as the evaluation of morphological change within coastal systems (Duffy et al., 2018; Quentin et al., 2019; Scarelli et al. 2017), in the assessment of short-term storm erosion on sandy beaches (Casella et al., 2016; Ierodiaconou et al., 2016; Turner et al., 2016), the long-term monitoring of coastal study sites (Clark, 2017; Gonçalves & Henriques, 2015; Johannes et al., 2012) and to delineate shoreline proxies to inform a temporal analysis (Albuquerque et al., 2018; Čermáková et al., 2016; Yoon-Kyung et al., 2019). The inclusion of manually surveyed Ground Control Points (GCPs) provides the models created from Structure from Motion (SfM) photogrammetry a higher degree of accuracy when compared with aerial surveys conducted without GCPs, and ensures that measurements are reliable and comparable (Clark, 2017; James et al., 2017; Joyce et al., 2018). Recent research (Gray et al., 2018) has successfully employed the high-resolution images produced from UAV surveys to validate the classifications from satellite imagery. The ability to rapidly deploy UAVs and conduct high-resolution surveys presents an opportunity to validate spatiotemporally varying data such as shoreline proxies that have been collected from coarser spatial resolution satellite imagery.

In this study, 8 kms of shoreline adjacent to a canal estate is analysed with different remote sensing methods to explore the barrier effects of the estate's structures on the littoral drift (Brayshaw & Lemckert, 2012; Carter, 1988; Komar, 1998) on a low-wave energy reflective beach on South Australia's Southeast coast (Figure 1). This study provides an investigation of shoreline change before and after coastal development and offers a method for on-going monitoring of high-resolution shoreline position at a high-temporal scale with CubeSat satellite technology. CubeSat technology is an area of continuous technologic advancement, with upgrades within existing and forthcoming Earth observation multi-satellite constellations signifying a continued improvement in spatial and temporal resolutions. Here, shoreline change is analysed over 3 different time periods with satellite sourced observations; over the course of a decade, a year and a winter storm season with the objective of developing an operational framework for automated image processing. The aim of this work is to show how the long-term term trends of shoreline change in the region were disrupted following coastal development with an examination of the trends of shoreline change at the medium- and short-term temporal scales. The following work utilises UAV technology to validate the automated shoreline extraction from the satellite systems that is based on established

remote sensing techniques. The validation from the high-resolution UAV surveys are presented here and support the expansion of these methods to further monitor shoreline change along sandy coasts. The methods presented in this work enables the extraction of important information for coastal and shoreline managers at a high temporal frequency and detail level, allowing for both short and long-term shoreline position monitoring and associated trends.

2. STUDY AREA

This study is focused on the Cape Jaffa marina and the 8 kms of adjacent beaches to the east and west. Cape Jaffa is located 315 kilometres to the south-east from the capital of South Australia, Adelaide. The Cape Jaffa marina was completed in 2008 with two rock training walls or groynes constructed for shoreline stabilisation and to provide an inlet protected from wave energy (Figure 1) These modifications have interrupted the natural longshore transport, similar to groynes in other parts of the world that have caused unintended shoreline change issues (Brayshaw & Lemckert, 2012; Komar, 1998). Maintenance of the marina has resulted in numerous issues for the residents and stakeholders involved, including the accretion of sand on the western side of the groynes, erosion of the beach on the eastern edge and sediment build up periodically blocking vessel access to the marina.

Just to the south of the Coorong region, the coastal system around Cape Jaffa is dominated by sandy beaches with characteristic low-wave energy reflective beaches that are backed by low foredune ridges (Short & Hesp, 1982). The beaches surrounding Cape Jaffa are primarily composed of carbonate-rich (91% carbonate) fine-grained sand, derived from the nearshore inner shelf (Short, 2019). The morphology of the area surrounding Lacepede Bay is shaped by a lack of deep-water wave energy, resulting in secondary sources of marine energy exerting their control on morphodynamics (Short & Hesp, 1980). Short and Hesp (1980) state that the shape of Lacepede Bay and the corresponding morphology of its beaches is thought to be shaped by the near-shore currents that facilitate the transport of sand waves which are often connected to the subaerial beach face and produce large protrusions of the shoreline. Shoreline sand waves are features that migrate with the littoral drift and often resemble cusps or undulations of the shore (Ashton & Murray, 2006; Ribas et al., 2013).

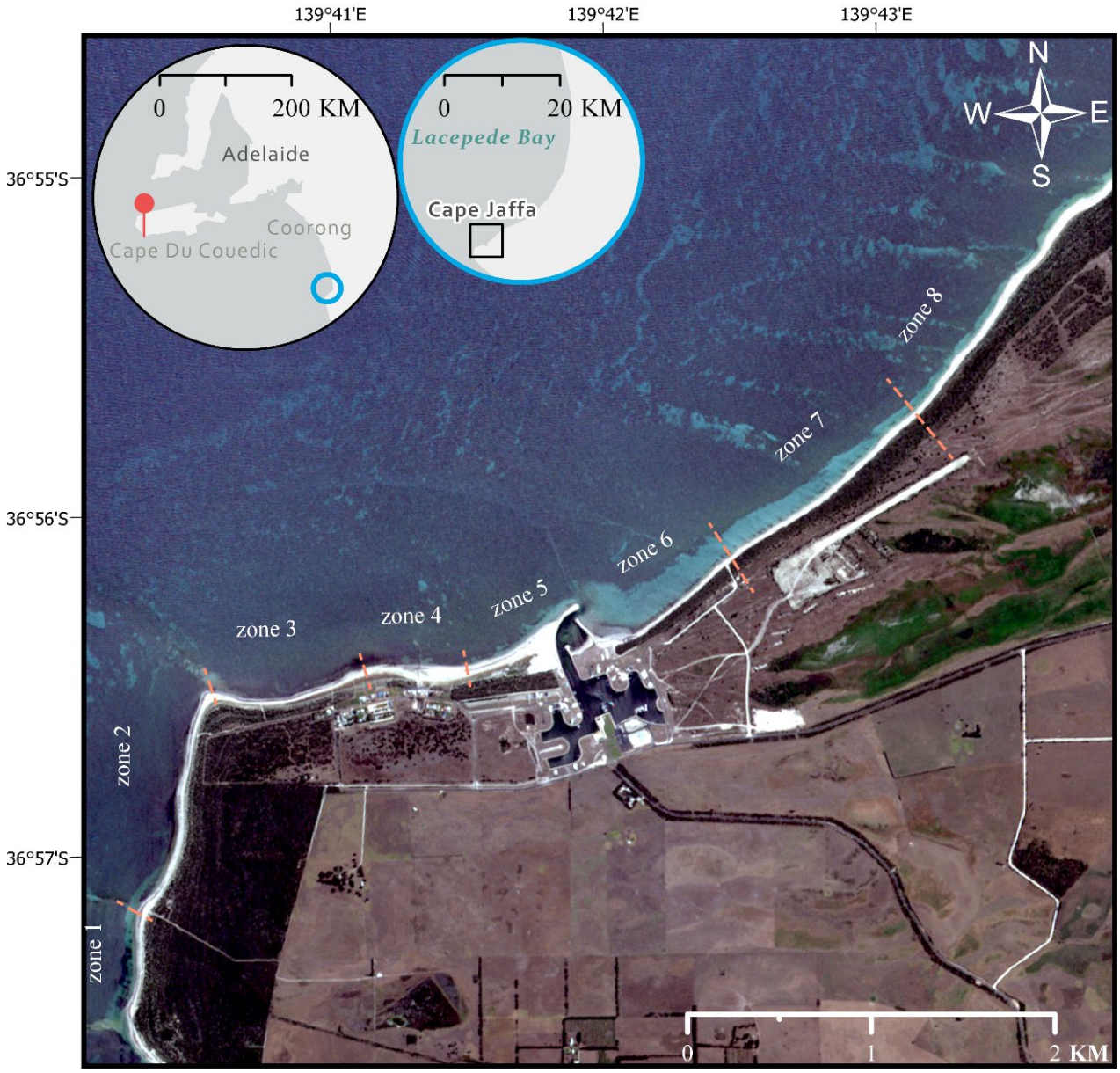

Figure 1 The extent of the shoreline analysed for this study is presented in this RapidEye satellite image, collected on 24 January 2019. Zones 1 -8 indicate area of subsequent analysis. Zone boundaries are indicated with the dashed lines and will be used throughout the rest of this study.

The coastal processes of the area are dominated by the Southern Ocean swell, micro-tides and shelf waves (Short, 2019). Short and Hesp (1984) summarise the typical wave conditions of the South East coast. Much of the year (62%) is dominated by a southwest swell of 2-4 metres with observations of high waves (>4m) less than 6%, with low to moderate waves observed at other times (31%). Short and Hesp (1984) report that the wave climate, similar to the prevailing wind direction, is a persistent year-round southwest swell with peaks occurring between April to September. The region is microtidal with mean spring high tides of 1.2 m (Bourman, 2016). The dominant direction of the littoral drift is northeast along the coastline (Planning SA, 2005) with sand

and seagrass carried alongshore. Short (2019) suggests that since 2008 when the marina was finished, an estimated 10,000 m^3 per annum of sediment has been moving north alongshore with a build-up of ~120,000 m^3 of sand on the western side of the constructed groynes. A significant seagrass community is located in the sheltered waters of Lacepede Bay off the coast of Cape Jaffa (Bonifacio & Pisanu, 2012). The life cycle of seagrass involves shedding old leaves, referred to as seagrass wrack (Lavery et al., 2013) which is often suspended in the littoral drift and deposited onto the shoreline where it accumulates and disperses across the beaches.

3. METHODOLOGY

3.1 Shoreline Definition

Following the work of previous shoreline change research (Dolan et al., 1980; Sytnik et al., 2018), shorelines are interpreted as a dynamic boundary between water and land surfaces that can be assessed as an indicator of morphological trends. In this study, the wet/dry boundary, also referred to as the instantaneous water line (IWL), and the edge of vegetation (EV) were chosen as shoreline proxies for change analysis, these proxies are illustrated with Figure 2. The decision to assess the wet/dry line was made given the local morphological and tidal conditions of the beaches surrounding the study site. The IWL has been shown to be a reliable indicator for multi-temporal shoreline change analysis in micro-tidal and low-gradient beaches which are typical for the region surrounding Cape Jaffa (Crowell et al., 1991; Ruiz-Beltran et al., 2019; Serafim & Bonetti, 2017; Sytnik et al., 2018). Specific to the range of tidal observations in this study, the low-declivity beaches suggest a minimal difference in location of water line proxies (>2 m). Careful consideration to wave energy, sourced from significant wave height observations and through interpretation of high-resolution aerial imagery, precluded the inclusion of aerial and satellite imagery where wave run up could be interpreted as proxy change. The edge of vegetation (EV) has been included in this analysis as well to provide a stable shoreline proxy that is able to be evaluated without the consideration of wave height or tidal variations (Ford, 2013) as this information was not readily available for all historical aerial imagery.

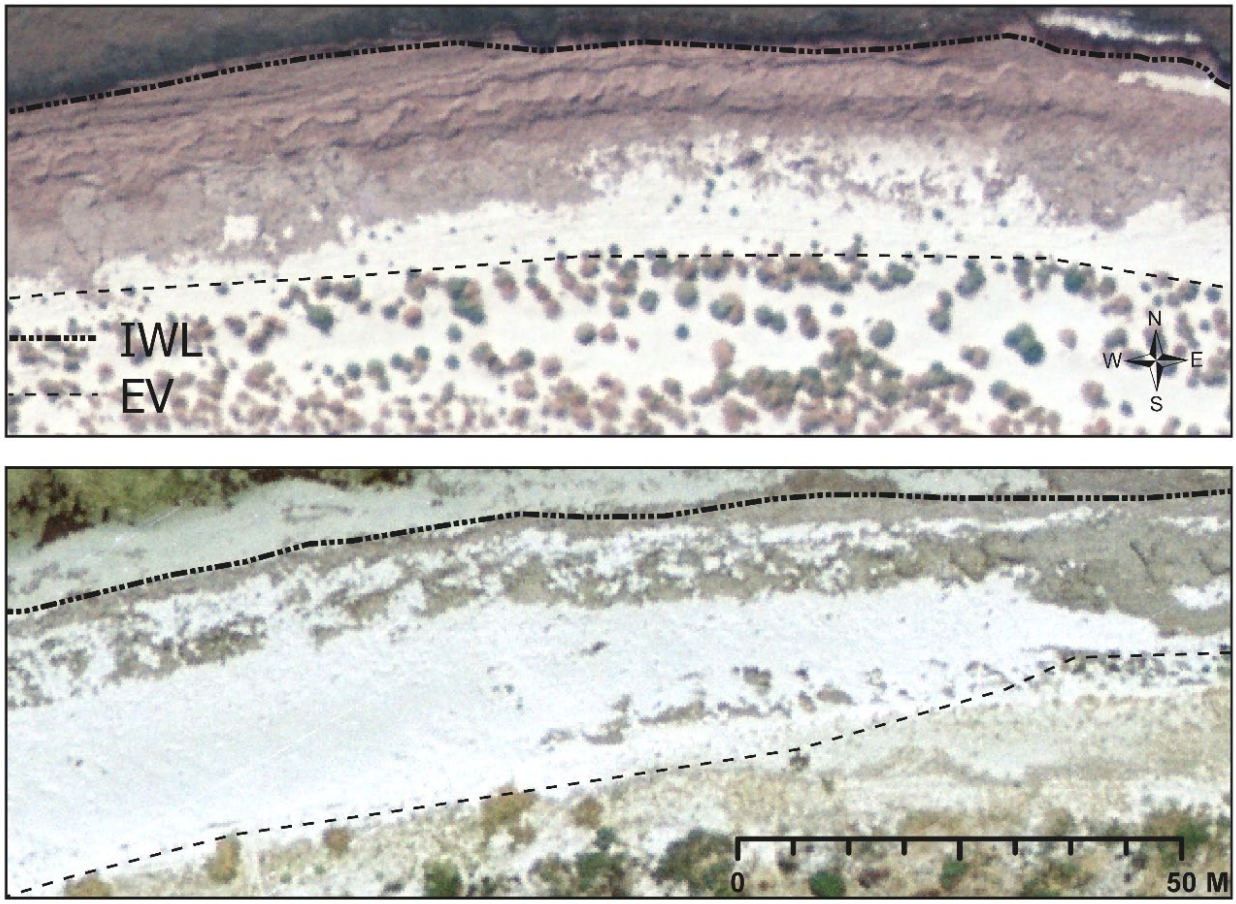

Figure 2 Example of the instantaneous water line (IWL), across the wet/dry boundary in sand and seagrass. The edge of vegetation (EV) corresponds to the last line of visible vegetation from aerial imagery, images from top to bottom are 1995/1975.

3.2 Aerial Imagery

3.2.1 Aerial Image Acquisition

Shoreline change before the construction of the Cape Jaffa Marina was assessed with imagery collected by airborne photography that was provided by the State Government of South Australia. Imagery of the study area was analysed from 5 dates, ranging from 1975 to 2005 (Table 1), to examine shoreline change over the past few decades. Tidal estimations and observations of significant wave height at time of image collection are indicators of atypical littoral conditions and are included within this study to identify and reduce potential sources of error. Specific tidal measurements were not contemporaneously collected for the time period, so tidal estimates were generated with a hindcast conducted by the Tidal Unit of the Bureau of Meteorology. Measurements of significant wave height commenced in November 2000 at the Cape du Couedic

waverider buoy off the southwestern tip of Kangaroo island by the Bureau of Meteorology and did not cover the timespan of this historical investigation.

Table 1 Information on airplane collected photographs from 1975-2005. The estimation of tidal level at time of image collection was generated with a hindcast from the Bureau of Meteorology.

Date	Tide (m)	Wave Height (m)	Pixel Size (m)
25/02/1975	.84	1:10000	.2
4/03/1987	.97	1:16000	.33
28/04/1995	.96	1:10000	.2
14/07/2000	1.3	1:10000	.2
14/03/2005	.9	1:40000	.8

3.2.2 Aerial Imagery Shoreline Interpretation

Aerial imagery was analysed to derive the shoreline changes and morphological trends across the decades pre-dating the construction of the marina. The imagery was geo rectified within the remote sensing software, ERDAS Imagine 2018, utilising operator identified GCPs of static objects across the time series. Due to the scale and extent of some images (1975, 1995 and 2000) and lack of fixed points along parts of the coastline, additional images to cover the study area were co-registered to a source image that was geo-referenced over an area with sufficient fixed objects. The RMS error was kept below a single pixel and visual checks of fixed objects across the imagery ensured an accurate georeferenced model.

Shorelines were digitised corresponding to the visible features within the imagery. The IWL was digitised according to the instantaneous water line which was interpreted to be the visible wet/dry line within sandy areas of the imagery and across the wet/dry line within accumulations of seagrass wrack (Figure 2). The EV was digitised as an indicator of shoreline to provide an additional shoreline proxy that is independent of daily weather specific variations of wave energy and tidal variations.

3.3 Satellite Imagery

3.3.1 Satellite Imagery Acquisition

Planet labs (2018) supplied the satellite imagery for this study through their education and research program. The satellite imagery was used to explore the inter and intra- annual change of

the shoreline surrounding Cape Jaffa. Two satellite observations systems were utilised, RapidEye and PlanetScope.

Table 2 Information specific to satellites utilised for this study. Sourced from Planet (2018)

Sensor	Bands	Total Satellites	Pixel (m)	Temporal Resolution
RapidEye	BGR, Red-Edge, NIR	5	5-6.5	5.5 days
PlanetScope	BGR, NIR	~170	3-4	Daily

3.3.1.1 RapidEye

Imagery was analysed from the RapidEye satellite system to assess the shoreline change over the past decade since construction of the canal estate was completed. The RapidEye constellation consists of five satellites launched in 2008 with individual satellites measuring less than one cubic metre and equipped with identical sensors (Planet 2018). Planet further specifies that the constellation orbits at 630 kilometres above the Earth's surface by a sun-synchronous orbit. The imagery has a spectral resolution that ranges from blue (440-510 nm), green (520-590 nm), red (630-685 nm), red-edge (690-730) to the Near Infrared (NIR) (760-850 nm) as shown in Table 2. Cloudless images outside of the winter season were chosen following the suggestions from Leatherman (2003) and Pajak and Leatherman (2002) to minimise the seasonal short-term variations that can occur as a result of severe storms on a longer-term trend analysis. The imagery was provided at level 3A which has been orthorectified and with radiometric and sensor corrections applied. The provided images (Table 3) were resampled to 5 m pixel size and was analysed in a World Geodetic System 1984 (WGS84) horizontal datum with a Universal Transverse Mercator (UTM) map projection specific to the region (zone 54). Tide predictions were generated from the Tidal Unit at the Bureau of Meteorology for the specific time of the image and significant wave height was sourced from the Cape du Couedic waverider buoy.

Table 3 Dates of RapidEye imagery utilised to assess shoreline change pre-construction of the Marina. Estimation of tidal level at time of photo collection provided by the Bureau of Meteorology and significant wave height sourced from the Cape du Couedic waverider buoy.

Date	Tide (m)	Wave Height (m)
20/04/2009	.8	2.02
27/11/2012	.67	2.77
2/01/2013	.48	1.63
1/04/2014	.6	2.13
16/10/2017	.91	1.66
24/01/2019	.57	1.90

3.3.1.2 PlanetScope

Imagery from PlanetScope, presented in Table 4 and 5, was analysed to illustrate the shoreline trends over the course of a year and over the course of the late autumn/winter storm season. The PlanetScope system consists of ~130 individual 'dove' satellites that are described by Planet (2018) as CubeSat 3U form factor (10 cm x 10 cm x 30 cm). The satellites provide imagery with a ground sample distance (GSD) of 3-4 meters orbiting at 400-475 kilometres above the earth's surface, following a sun-synchronous orbit and the orbit of the International Space Station. PlanetScope imagery has a spectral resolution that ranges from blue (455-515 nm), green (500-590 nm), red (590-670 nm) and NIR (780-860 nm) (Table 2). This study utilised PlanetScope Ortho Scene Products (level 3B) which were provided orthorectified, scaled to Top of Atmosphere (TOA) radiance, resampled to 3m and projected to WGS84 (zone 54). The capabilities of radiometric calibration and atmospheric corrections range across the constellation as new satellites with improved hardware are periodically launched (Cooley et al., 2017; Planet, 2018).

Table 4 Date of PlanetScope 4 band imagery used to assess shoreline change over the course of a year and their corresponding tidal measurement at time of image capture from the Bureau of Meteorology and significant wave height from Cape du Couedic waverider buoy.

Date	Tide (m)	Wave Height (m)
21/04/2018	.7	1.8
22/06/2018	.8	2.4
28/08/2018	.8	1.4
30/09/2018	.61	2.9
30/11/2018	.9	2.8
24/01/2019	.6	1.9
26/02/2019	.15	2.4
28/03/2019	.22	1.8
16/05/2019	.9	2.59

Table 5 Date of PlanetScope 4 band imagery utilised to analyse change over a winter storm season and their corresponding tidal measurement from the Bureau of Meteorology and significant wave height from Cape du Couedic waverider buoy.

Date	Tide (m)	Wave Height (m)
21/04/2018	.7	1.8
09/05/2018	.7	3.5
22/06/2018	.8	2.4
13/07/2018	1.3	2.2
14/08/2018	.6	3.9
22/08/2018	1	1.6

3.3.2 Image Pre-Processing

Cooley et al. (2017) suggests that Planet's image calibration, which can be inconsistent as a result of its selection of varying quality and inexpensive sensors across a multi-satellite constellation, could result in a significant source of error in a temporal analysis if not addressed. Thus, atmospheric and geometric corrections were applied to individual images to reduce sources of possible classification error arising from the varying temporal effects of atmosphere (Houborg & McCabe, 2018a; Liu et al., 2012; Wicaksono & Hafizt, 2018), and potential geolocation errors arising from inconsistent georeferencing (Scheffler et al., 2017).

RapidEye imagery was pre-processed utilising the metadata provided from Planet (2018) that is specific to individual images and environmental conditions at time of collection. The Rapid Atmospheric Correction in ERDAS imagine 2018 was used to convert raw digital number (DN) values to ground reflectance values to minimise atmospheric interference. First, the radiance values are converted to TOA reflectance values and then scaled to ground-level reflectance values. This process is done by adjusting the imagery for radiometric variations caused by incident sun energy and by performing atmospheric corrections for the effects of light scatter and absorption utilising image specific statistics (Hexagon Geospatial, 2018).

Through the use of a Python script written for this research (Appendix 2), individual PlanetScope images were scaled to TOA reflectance by coefficients provided by Planet (2018). Planet had previously released a surface reflectance (SR) product that utilises the 6S radiative transfer model with atmospheric observations from MODIS (Planet 2018), but data exploration done as part of this research found the SR product produced inconsistent values for thresholding. Additionally, the SR product was not available for all dates chosen as per the time period, so image specific atmospheric correction was performed. The dark object subtraction method, developed by Chavez (1988, 1996), was chosen as it has been successfully shown to reduce the effects of atmosphere in temporal studies utilising remotely sensed data (Ahmed et al., 2018; Cooley et al., 2017; Mancino et al., 2014; Ozturk & Sesli 2015; Song et al., 2001; Wicaksono & Lazuardi, 2018; Wicaksono & Hafizt 2018). Following the results from Wicaksono and Hafizt (2018), the median value of an area of interest (AOI) per specific band was observed from a chosen dark object over optically deep and calm water and subtracted from the TOA reflectance scaled image to produce

ground-level reflectance values. The median value of the representative dark object was chosen as exploratory observations of the minimum value was shown to be detecting scanner noise.

During the data evaluation process done as part of this research, certain images were found to have the NIR and RGB bands mis-registered within the image. Multiple images that had mis-registered multi-spectral bands were compared and found to have variable levels of geo-referencing errors ranging from 5-20 metres in inconsistent directions, suggesting significant issues occurring in the geo-referencing workflows currently utilised by Planet. These geometric inconsistencies are of particular concern for a study, such as this one, which is investigating change over time at a high spatial resolution (sub 10 m). Images found to have mis-registered NIR bands were therefore excluded from the study. Imagery found to have consistent registration across all bands from RapidEye and PlanetScope were co-registered to the earliest image within the specific time series to act as a master image. Co-registering standardises the spatial reference of georeferenced images and helps to address the displacements that exist between images as a result of inter or intra-sensoral mis-registration (Scheffler et al., 2017) and is a vital step in spatiotemporal studies to avoid image misalignments (Behling et al., 2014). Co-registering was performed in ArcGIS Pro (2019) with visual checks of static features across the images to ensure a precise match and the RMS error was kept below .5 pixels.

3.3.3 Image Analysis and Shoreline Extraction

For each individual RapidEye and PlanetScope satellite image, the waterline was extracted in an automated process utilising an adaptive thresholding method on the NIR band. Multi-temporal image analysis requires adaptive thresholds for segmenting an image (Dhanjal-Adams 2016; Liu & Jezek, 2004; Murray et al., 2012; Sagar et al., 2017; Sousa et al., 2018) due to the varying nature of atmospheric noise and interference (Liu et al., 2012). Although atmospheric correction methods have been shown to minimise the temporal variations in atmosphere, correction techniques are recognised to be imperfect (Ji et al., 2009). The exploration into the inconsistencies of global thresholds in a temporal analysis for remote sensing indices by Liu et al., (2012) suggests that the fluctuating conditions of the atmosphere inevitably result in inconsistent radiometric calibration and atmospheric correction. Adaptive thresholds for image segmentation and classifications of

landscape features ensures that the temporal effects of atmosphere do not result in misclassifications of pixels based on imperfect global thresholds (Liu & Jezek, 2004).

For this study, the individual bands of the imagery were extracted and masked to a buffer of the coastline to improve processing efficiency and improve classification, including area over shallow water and into the vegetated areas. The waterline extraction was carried out with a python script that adapted the Otsu (1979) method of adaptive thresholding for the NIR band. The histogram of NIR pixel values around the land-water boundary exhibits a bimodal Gaussian curve that locally adaptive thresholds can isolate and subsequently classify (Chen & Chang, 2009; Li & Gong, 2016; Sagar et al., 2017; Sousa et al., 2018). The distinct difference in reflectance values of shallow water and saturated seagrass wrack pixels can be observed in the large variation in the NIR (Band 4) in Figure 3. The Otsu thresholding technique is based on a histogram thresholding algorithm that maximises inter-class variance, partitions the imagery based on the land/water boundary and has been used extensively in waterline extraction studies (Cooley et al., 2017; Hagenaars et al., 2018; Heine et al., 2015; Li et al., 2013; Lu et al., 2011; Vos et al., 2019). The partitioned image was re-classified and the resulting land pixels had a majority filter and boundary clean applied to remove excess noise from the classification. The raster representation of land was then converted to a smoothed vector to represent the instantaneous waterline.

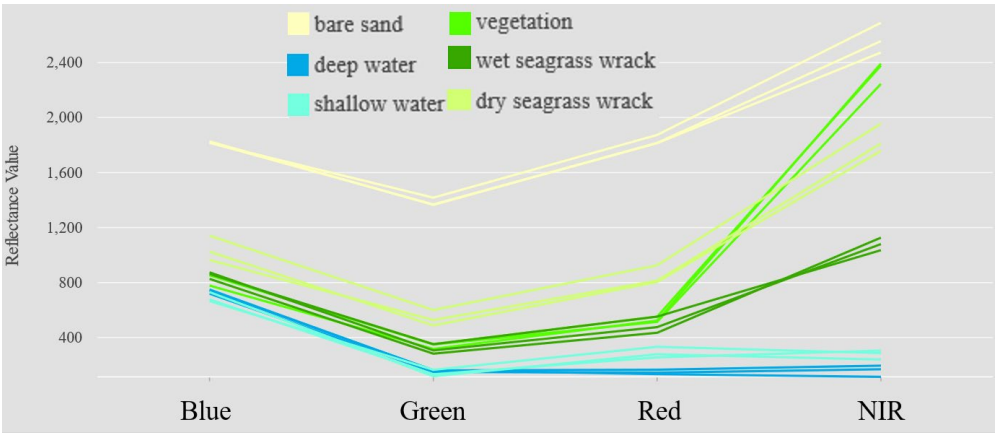

Figure 3 Spectral profile for the PlanetScope images for different land types within study area.

The EV was extracted from the imagery in a semi-automated process with the use of the Normalised Difference Vegetation Index (NDVI) index (Equation 1). The NDVI index has been

used extensively to monitor vegetation vigour and track its changes in various spatiotemporal research (Houborg & McCabe, 2018a; Massetti et al., 2016; Valderrama-Landeros et al., 2017). The shoreline area was masked to the land output of the waterline classification and further classified via an ISODATA unsupervised classification method into 4 classes. A re-classification eliminated sand pixels from the masked shoreline layer and a majority filter removed excess noise. Mis-classified stands of seagrass wrack outside of the edge boundary of vegetation were eliminated with the use of a minimum size threshold of 30,000 metres^3. Operator revision of the vector line representation of the EV was required where large build-ups of seagrass wrack accumulated and crossed the sand divide from near the water's edge to the vegetated areas. This occurred predominantly in front of the Cape Jaffa jetty and on the eastern edge of the marina. Visual interpretation based on the original image's was used to interpolate across from the correctly classified sides of EV.

$$NDVI = \frac{NIR-R}{NIR+R} \qquad \textbf{Equation 1}$$

3.4 UAV surveys

Three UAV Surveys were flown with a passive RGB camera over the beaches surrounding Cape Jaffa to provide high-resolution imagery for a change over time analysis and to validate the shorelines vectors automatically extracted from the remote-sensing workflows. Surveys were flown at 50m, with a resulting GSD of 1.16 - 1.24 cm (Table 6). The majority of the surveys were flown with the Mavic 2 Pro UAV that has a L1D-20c Hasselblad camera. The survey flown in April of 2019 had supplementary images collected with a Phantom 3 Professional with a FC300X Sony camera. Each survey contained at least 12 Global Navigation Satellite System (GNSS) measured GCPs that had been collected with targets across the study area in the Geocentric Datum of Australia 1994 (GDA94 Zone 54) coordinate system with an Earth Gravitational Model 1996 (EGM96) geoid model. Orthomosaics, processed in Pix4D a UAV photogrammetry software, were generated from imagery collected to the area west of the Cape Jaffa Marina.

Table 6 Date of UAV surveys flown at the Cape Jaffa Marina with average ground sample distance (GSD) per survey. Relevant tide and significant wave height measurements sourced from Bureau of Meteorology.

Date	Time	Tide (m)	Wave Height (m)	GSD (cm)
25/04/2019	14:50-17:20	1.1-1.1m	3.8-4.4	1.24
19/07/2019	9:26-12:48	.9-1.3m	3.3-3	1.19
30/08/2019	9:23-12:28	1-1.4m	2.1-2	1.16

3.4.1 UAV shoreline Interpretation

The UAV orthomosaics were utilised to assess morphological change at a sub-metre scale to the west of the Cape Jaffa Marina. Following the methods of Yang et al., (2019) the IWL shoreline proxy was digitised from the orthomosaics, with the visible wet/dry line interpreted from the imagery.

3.5 Shoreline Validation and Temporal Change

The automated shoreline extraction was validated with comparisons to other sensors at or near time of collection. On 24 January 2019, PlanetScope and RapidEye satellites collected an image within the same hour on a clear day over Cape Jaffa. These images were evaluated independently, and their classifications were compared for alignment with a measurement of difference between the extracted shoreline proxies.

Additionally, the orthomosaics and IWL shoreline proxies from the UAV surveys were employed to validate the automated shoreline extraction methods from PlanetScope imagery collected at or near the time of the UAV surveys. Although both surveys in July and August were flown with clear sky conditions at a time when Planet satellites are generally overhead and collecting imagery, neither occasion resulted in simultaneous satellite image capture and UAV survey. Planet does not provide a satellite prediction service and was unable to advise whether images would be collected on planned field site visits. Instead, UAV surveys were compared to shoreline proxies that were extracted from images taken within 48 hours that had similar tidal levels (<.1 m difference).

To assess shoreline change across the different time series the Digital Shoreline Analysis System version 5.0 (DSAS), which was developed by Thieler et al. (2009), was utilised to investigate shoreline change and produce rate of change statistics. The software extension provides a method of measuring the rates of change over time of cross-shore profiles set at a user

specified interval and has been used extensively in shoreline change studies (Oyedotun, 2014). In this study, transects were cast 50 m apart for the aerial and satellite imagery analysis and 5 metres apart for the UAV IWL comparison from baselines on the landward edge of the shoreline proxies. The statistics utilised to assess the morphological trends of the time series were the net shoreline movement (NSM), shoreline change envelope (SCE), linear regression rate (LRR) and the end point rate (EPR) calculated at a 95% confidence interval (CI). NSM provides a measurement of distance between the youngest and oldest shorelines along the transects, while the EPR is calculated by dividing the distance of the NSM by the time elapsed. SCE is the distance between the closest and farthest shorelines from a user delineated baseline within a data set and provides a statistic on the total variability of shoreline positions across the time series. To analyse the rates of change of the shoreline proxies, the LRR was chosen as it has been shown to be a statistically and robust quantitative indicator in shoreline studies with (>2) shoreline observations (Crowell et al., 1997; Sytnik et al., 2018). The LRR is derived by applying a least squares regression line to all shorelines across the time series and provides an estimate of the rate of change (metre/year) for the measured shoreline movement (Bheeroo et al., 2016; Sytnik et al., 2018). Although linear regression is a widely utilised statistical technique for interpreting shoreline movement (Crowell & Leatherman, 1999), it fails to account for differences in temporal trends such as seasonal variability or shoreline trend reversals (Hapke et al., 2010). To account for this, the average trends of the different time series (decade, inter/intra-annual and winter storm season) were calculated to showcase short-term and long-term shoreline change.

Following the work of Hapke et al., (2010) uncertainty associated with the shoreline proxies (U_p) within the different time series was calculated based off the square root of the sum of the uncertainty terms; the digitisation uncertainty (U_a) and georeferencing uncertainty (U_b). DSAS applies the user-defined estimations of uncertainty associated with the specified CI (95%) for the LRR and interprets the resulting fit of the time series to a linear trend of change between the earliest and latest date (Hapke et al., 2010). The confidence interval of linear regression (LCI) or the standard error of the slope with the specified CI describes the uncertainties of the reported regression rate (Himmelstoss et al., 2018) and is utilised in this study to interpret the significance of erosion/accretion trends. Transects are classified as having a statistically significant

erosion/accretion rate if their LRR value has a larger magnitude than the LCI value. Higher LCI rates suggest that the shoreline adjustment rates were not constant over time, with variable rates of change and trends, and that a resulting linear fit to the data would be poor.

The aerial photographs' shoreline proxies, the IWL and EV, were assessed with the use of NSM, SCE and EPR to illustrate the change in shoreline position across the time series and the LRR to provide the rates of change between dates in zones 1-5. The IWL from the year 2000 image was eliminated from the water line analysis due to a visual interpretation of high-wave energy and its collection date occurring within the winter-storm season, as per the suggestions from previous studies (Leatherman, 2003; Pajak & Leatherman, 2002; Sytnik et al., 2018). An additional analysis of the NSM of zones 6-8 was done for the earliest and latest image within the time series, 1975 and 2005, as sufficient imagery was not able to be acquired for the intervening years to calculate the rates of change. Uncertainty for the air photos displacement analysis was calculated off an estimated +/- 1 metre for U_b and +/- 2 metre U_a based off averaged RMS values, pixel sizes and estimates of tidal variation.

Satellite derived shoreline proxies were assessed in time series groups based on their relative orientation from the groynes, either on the eastern or western side of the Marina. This was done to provide an illustration of the barrier effects on the littoral drift and the subsequent erosional/accretional changes that have occurred. The IWL and EV were assessed for the RapidEye and intra-annual PlanetScope time series with the use of the NSM, SCE and EPR to illustrate the change in shoreline proxy position and with the LRR to provide a statistic for the rates of change. Uncertainty for the RapidEye derived shoreline proxies (U_p) and subsequent analysis was set as the sum of the square root of +/- 5 metre for U_b and +/- 10 metre U_a and +/- 3 metre for U_b and +/- 6 metre U_a, for the PlanetScope sourced proxies. These were based on the mean RMS values from co-registering the data series and results from UAV sourced shoreline validation.

The three IWLs derived from UAV Surveys were compared in a time series analysis to illustrate the area change experienced by the shoreline at a high-spatial scale over the course of a winter storm season. The statistics chosen (NSM and LRR) were based on similar shoreline change analysis utilising UAVs (Yoon-Kyung et al., 2019) and were evaluated to provide suggestions of shoreline change across the 800 m to the immediate west of the Cape Jaffa Marina.

An estimation of uncertainty (U_p) for the UAV surveys was set as the sum of the square root of +/- .1 metre for U_b and +/- .2 metres for U_a based off the average RMS values and pixel size.

4. RESULTS

To assess the variability in shoreline location over time, shoreline time series of pre- and post-construction of the Cape Jaffa Marina were analysed independently. Similarly, the shoreline time series that were derived from satellite information were split between illustrative time frames; across a decade, a year and a winter storm season. Both the Instantaneous Water Line (IWL) and Edge of Vegetation (EV) were analysed to show the different response of shoreline types across varying temporal scales. The variability in shoreline positions from the different time series was analysed statistically and illustrates accretional or erosional morphological trends at different time scales.

4.1 Shorelines detected by Aerial Imagery (1975-2005)

89 transects oriented transverse to the coast and set at 50 metre intervals were assessed to explore patterns of shoreline movement pre-construction of the marina, according the methodology employed for the DSAS analysis. Shoreline proxies considered here are the IWL and the EV with the resulting statistics from the DSAS analysis presented in Table 7. The Linear Regression Rate (LRR, rate of shoreline change in metres per year) for the EV and IWL across zones 1-6 are presented in Figure 4, zones 6-8 are not included as they did not have sufficient imagery to provide a rate of change analysis. Figures 5, 6 and 7 show the IWL shorelines from aerial imagery and the cross-shore transects classified based on their Net Shore Movement (NSM, the distance between the oldest and youngest shorelines) across zones 1-8. According to the analysis, zones 1 and 2 (Figure 7) on the western facing beaches experienced a trend of steady seawards advance with distinct peaks of sediment accretion related to sand wave dynamics (Ashton & Murray, 2006; Ribas et al., 2013).

The rate of change for the 30 years evaluated within this time series (zones 1-6) of the EV shows that the proxy has advanced at an average of .67 m per year (LRR) across a total average Shoreline Change Envelope (SCE) of 27.58 m. The End Point Rate (EPR) provides another estimate of the annual rate of change that is independent of shoreline positions between the youngest and oldest shoreline, of on average .78 m/yr. The comparison between the mean LRR

and EPR shows that rate of change has varied across the time series and its total Net Shore movement of an average 17.33 m. The majority of the EV and IWL transects have been classified as accretional by the EPR and the NSM statistics, with the erosional transects located within zones 6 and 7 (Figures 4, 5 & 6). The value of the standard error from the linear regression slope (LCI), which provides an indicator for the level of uncertainty reported for the fit of a linear regression model, for the EV it was .22 and suggested that 41 transects experienced statistically significant accretion. The IWL transects experienced a similar pattern of progradation with an average LRR rate of .6 m/yr across an average SCE of 21.17 m. The mean EPR was .58 m/yr with an average NSM of 17.33 m. The average LCI for the IWL was .27 with 18 transects experiencing a statistically significant accretion rate and none a statistically significant erosion rate.

Table 7 Statistics from DSAS of shorelines sourced from aerial imagery from 1975-2005 from zones 1-6. The IWL series had the 2000 waterline excluded from analysis. Statistics shown are Linear Regression Rate (LRR), End Point Rate (EPR), Shoreline Change Envelope (SCE), and Net Shore Movement (NSM). Total transects classified as Erosion (ER), Accretion (AC) according to IWL data.

	LRR (m/yr)		**EPR** (m/yr)		**SCE** (m)	**NSM** (m)	
	ER(10)	AC(79)	ER (9)	AC(80)		ER(9)	AC(80)
EV	-0.7 to -0.01	.08 to 1.6	-.62 to -.05	.02 to 1.8	5 to 54	-18.7 to -1.5	.6 to 54
IWL	-.33 to -.03	.01 to 2	-.4 to -.02	.01 to 2.1	4 to 64	-12.09 to -.5	.4 to 63.9

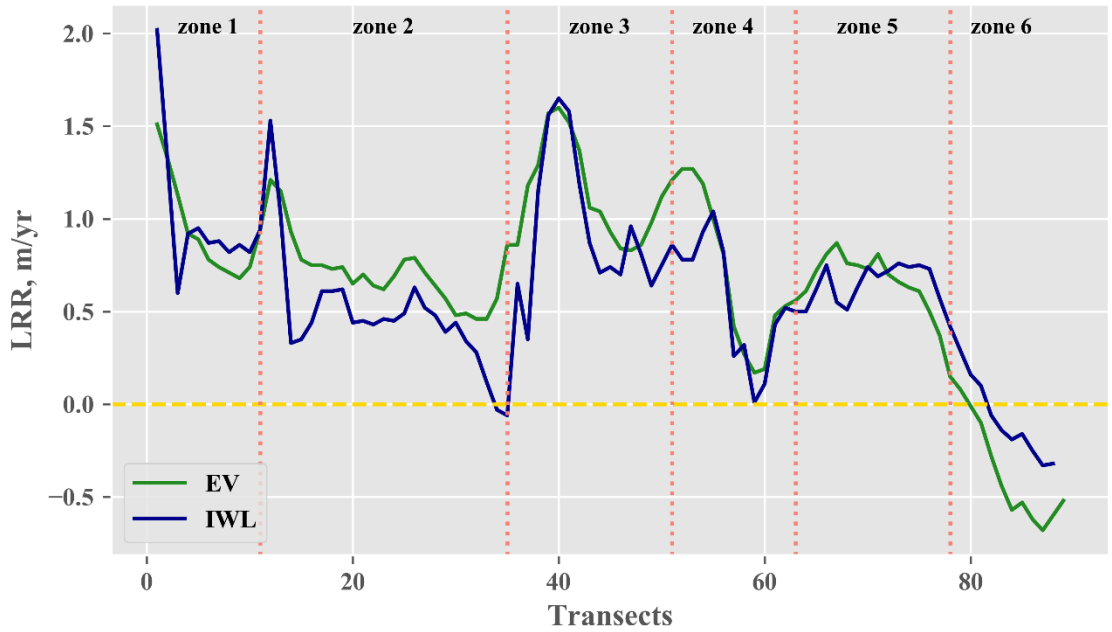

Figure 4 Rates of annual shoreline change based on the Linear Regression Rate (LRR) for the Instantaneous Water Line (IWL) and Edge of Vegetation (EV) sourced from aerial imagery, 1975-2005, pre-marina construction. Transects 1-89 represented West to East.

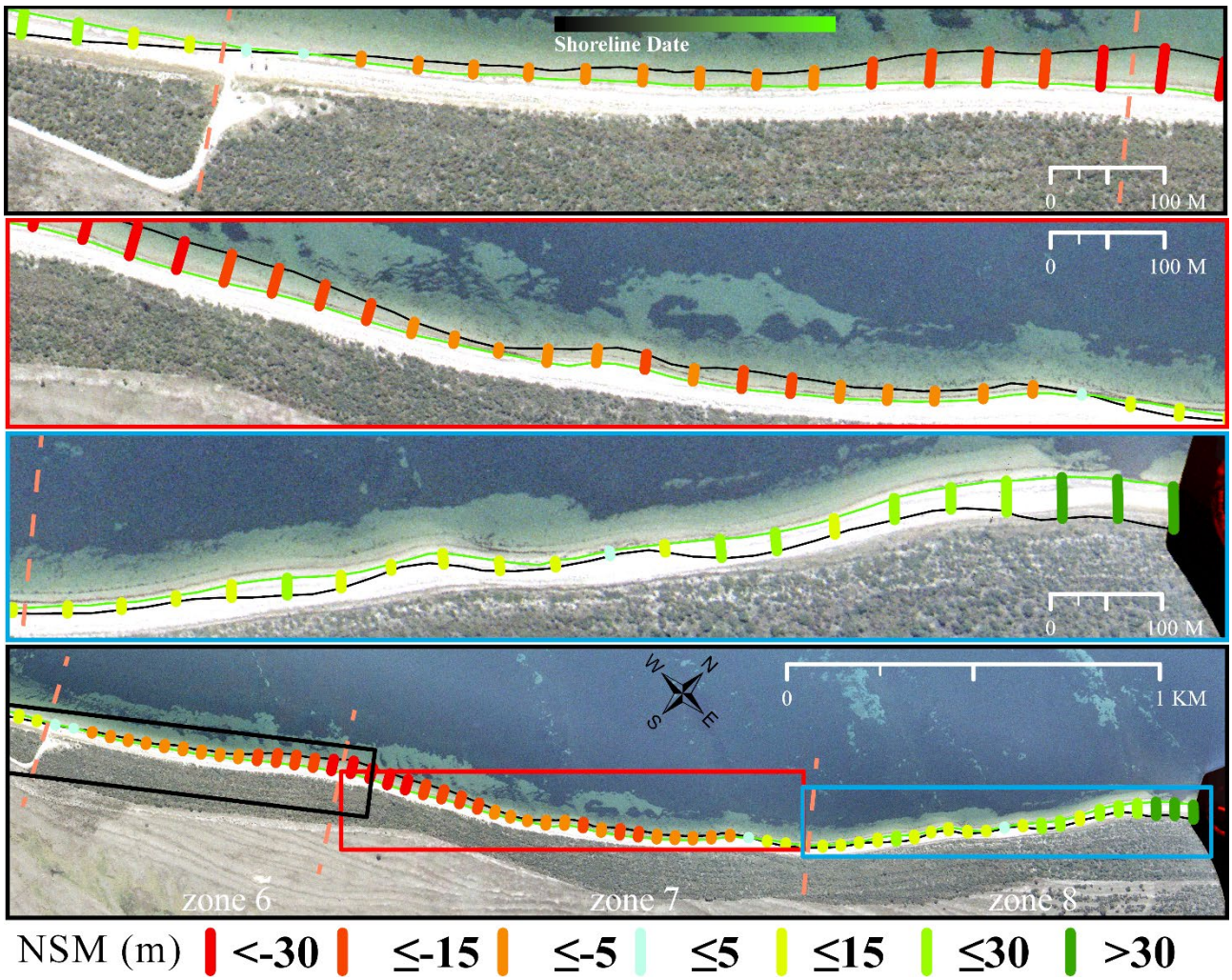

Figure 5 Instantaneous Water Line (IWL) shoreline proxies sourced from aerial imagery from 1975-2005, pre-marina construction. Shoreline proxies are presented from Black to Green, with oldest proxy within time series coloured black and most recent approaching light green. Transects reflect the Net Shore Movement (NSM) across the time series in zones 6-8. Base image is from 2005. Marina will be constructed on western edge of zone 6.

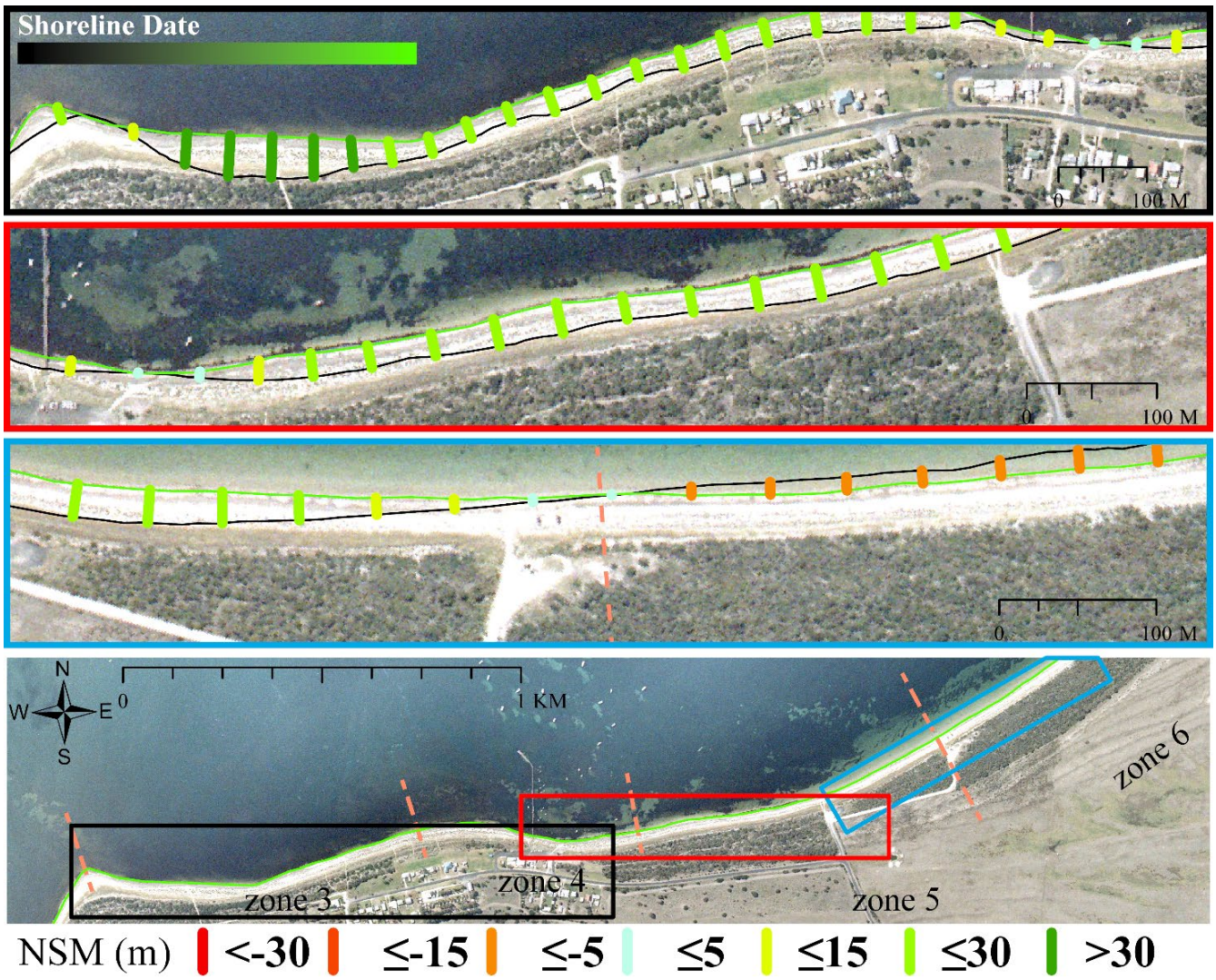

Figure 6 Instantaneous Water Line (IWL) shoreline proxies sourced from airplane collected imagery from 1975-2005. Transects reflect the Net Shore Movement (NSM) across the time series in zones 3-6. Base image is from 2005. Marina will be constructed at boundary between zone 5 and 6. Shoreline proxies are presented from Black to Green, with oldest proxy within time series coloured black and most recent approaching light green.

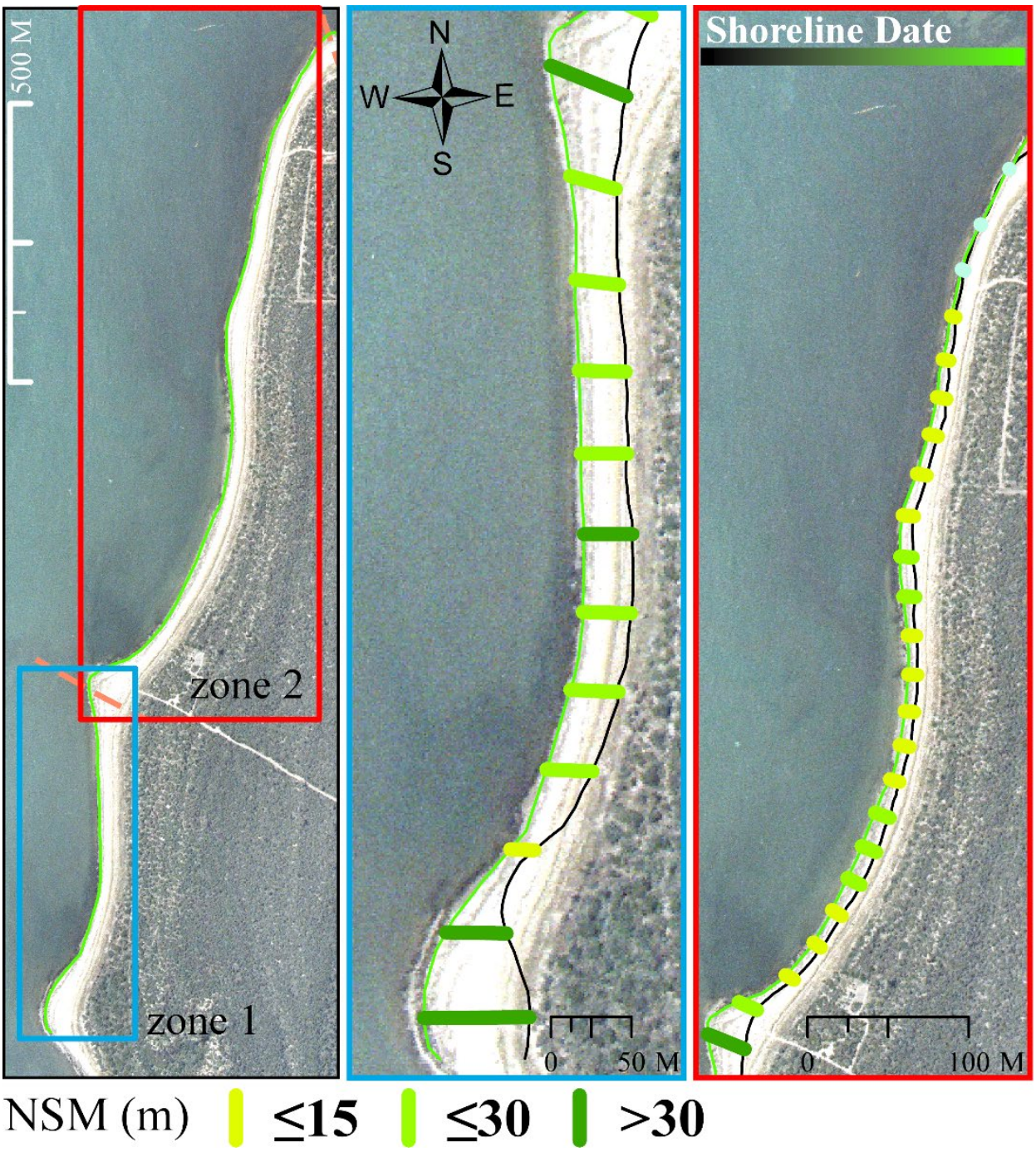

Figure 7 Instantaneous Water Line (IWL) shoreline proxies sourced from airplane collected imagery from 1975-2005. Transects reflect the Net Shore Movement (NSM) across the time series in zones 1 and 2. Base image is from 2005. Shoreline proxies are presented from Black to Green, with oldest proxy within time series coloured black and most recent approaching light green.

4.2 Shorelines detected by Satellite Imagery

4.2.1 Inter-Annual variation (2009-2019)

80 transects at 50 m intervals on the western edge of the marina and 68 on the eastern (Figure 1) were analysed with observations sourced from the RapidEye satellite constellation. The Linear Regression Rate (LRR) which illustrates the average rates of change across the time series

(m/yr) of the IWL and EV shorelines are shown in Figure 8. The shoreline changes experienced across the past decade in the study area are illustrated in Figures 9, 10 and 11 by the transects classified in terms of Net Shore Movement (NSM) of the Instantaneous Water Line (IWL) while the statistics regarding temporal changes are shown in Tables 8 and 9 for both the EV and IWL shorelines.

The shoreline to the east of the marina (zones 6-8) is mainly characterised by erosional transects with an average rate of change of -2.29 m/yr (LRR) for its EV and -3.03 m/yr for the IWL (Figure 8B). The relation between the steady negative LRR over a 10 year period and the resultant net erosion of the shoreline is illustrated in Figure 9, with the correspondingly high erosional (negative) LRR rates in Figure 8B shown in zones 6 and 7 reflected by the similarly higher negative NSM rates in Figure 9. The average End Point Rate (EPR) for the EV is -2.07 m/yr across a mean NSM of -20.69 M and it showed a slightly lower rate of retreat and erosional extent compared to the IWL (mean EPR of -2.88 m/yr across an average NSM of -28.81 m). The average measure of shoreline position variability (SCE) across the EV transects is 26.49 m and 32.41 m for the IWL. Overall, of the 66 EV cross-shore transects evaluated east of the marina, 52 were classified as erosional by the EPR and NSM statistics with only 14 categorised accretional (zone 8, Figure 1). The 68 transects of the IWL exhibited predominantly erosional trends (61) with 7 transects on the eastern most-part of the study area (Figure 9) classified as depositional. The LCI, which provides an indicator for the goodness of fit to a linear regression model in explaining the shoreline positions, for the EV was an average .56 and .82 for the IWL, suggesting that although there has been some variability in the shoreline pattern, most of the transects experienced a linear erosional trend. A majority of the transects, both EV (56) and IWL(49) experienced a statistically significantly erosion rate over the past decade, after the construction of the marina.

To the west of the marina, the transects closer to the groynes experienced a distinct progradational trend as shown by the net positive increases of the rate of change (LRR) and NSM as shown in Figure 8A and Figure 10, suggesting substantial accretion in zones 3-5. Zones 1 and 2 had a lower LRR and experienced a reduced range of NSM (Figure 11) indicating a more stable shoreline compared to zones 3-8. The distinct peaks of erosion shown in Figure 8A within zones 1 and 2, are transects across highly dynamic sand wave features. The rate of change across the

western part of the study area for the EV was 1.67 m/yr (LRR) and 1.25 m/yr for the IWL. The SCE showed that the shorelines varied between an average 26.63 m for the EV and 32.87 m for the IWL. The mean EPR, which provides a rate of change for the overall shoreline movement based on the youngest and oldest proxy within the time series was 1.89 m/yr in the EV transects and an average NSM of 18.71 m. Similarly, the IWL transects had an average EPR of 1.58 m/yr across a mean NSM of 15.77 m. Of the 80 IWL transects evaluated on the western side of the marina, 48 were categorized as accretional by the NSM and EPR with 67 of 72 EV transects characterised as accretional. The LCI showed that compared to the transects to the east of the marina, the EV and IWL on the west had a larger net positive regression rate and that its LCI value indicated greater variability in the shoreline trends (LCI is .64 for EV and 1.33 for the IWL). Subsequently, 28 EV transects were evaluated to have experienced statistically significant erosion with 19 of the IWL transects experiencing statistically significant accretion and 2 significant erosion.

Table 8 Statistics from the RapidEye shoreline time series to the east of the Cape Jaffa Marina, 2009-2019. Classified erosion and accretion transect refer to the statistics of the Instantaneous Water Line (IWL). Statistics shown are Linear Regression Rate (LRR), End Point Rate (EPR), Shoreline Change Envelope (SCE), and Net Shore Movement (NSM). Total transects classified as Erosion (ER), Accretion (AC) according to IWL data.

	LRR (m/yr)		**EPR (m/yr)**		**SCE (m)**	**NSM (m)**	
	Er (61)	Ac (7)	Er (61)	Ac (7)		Er (61)	Ac (7)
EV	-7.13 to -.01	.13 to 1.12	-7.58 to -.04	.06 to .97	5.74 to 75.8	-75.8 to -.39	.04 to 9.73
IWL	-7.85 to -.07	.18 to .62	-7.95 to -.06	.02 to .43	7.44 to 79.5	-79.5 to -.58	.17 to 4.29

Table 9 Statistics from the RapidEye shoreline time series to the west of the Cape Jaffa Marina, 2009-2019. Classified erosion and accretion transect refer to the statistics of the Instantaneous Water Line (IWL). Statistics shown are Linear Regression Rate (LRR), End Point Rate (EPR), Shoreline Change Envelope (SCE), and Net Shore Movement (NSM). Total transects classified as Erosion (ER), Accretion (AC) according to IWL data.

	LRR (m/yr)		**EPR** (m/yr)		**SCE** (m)	**NSM** (m)	
	Er (41)	Ac (39)	Er (32)	Ac (48)		Er (32)	Ac (48)
EV	-1.34 to -.09	.02 to 7.9	-.47 to -.1	.09 to 8.07	2.62 to 96	-4.65 to -1	.9 to 80.7
IWL	-4.9 to -.1	.2 to 9	-4.5 to -.04	.02 to 10.6	4.5 to 109.8	-44.8 to -.36	.18 to 106

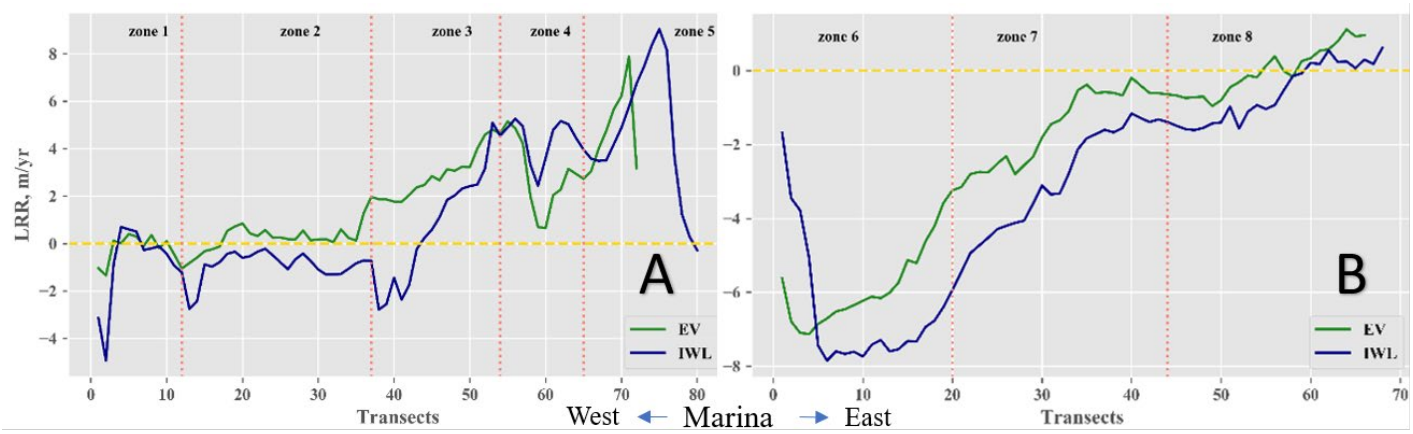

Figure 8 Transects of the Linear Regression Rate (LRR) for the Instaneous Water Line (IWL) and edge of Vegetation (EV) for the inter-annual Rapideye shoreline time series. Zones 1-5 shown in Plot A, located on the western side of the marina with transects 1-80 situated from East to West. Zones 6-8, shown in Plot B, for the eastern side of the marina.

.

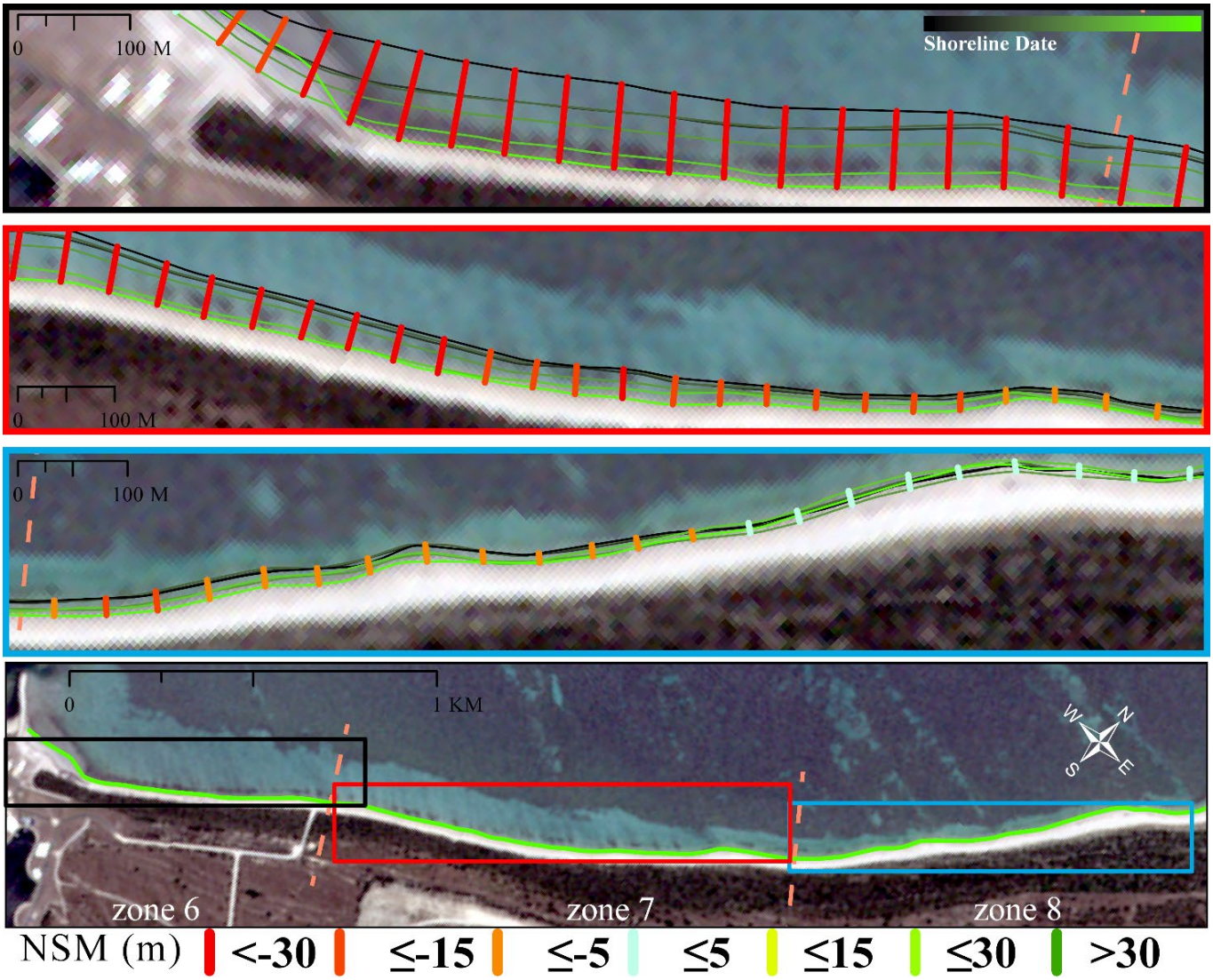

Figure 9 Instantaneous Water Line (IWL) shoreline proxies represented over a RapidEye image from 2019. Cross-shore transects represent the Net Shore Movement (NSM) and are illustrating kms of a mainly erosional shoreline. Shoreline proxies are presented from Black to Green, with oldest proxy within time series coloured black and most recent approaching light green.

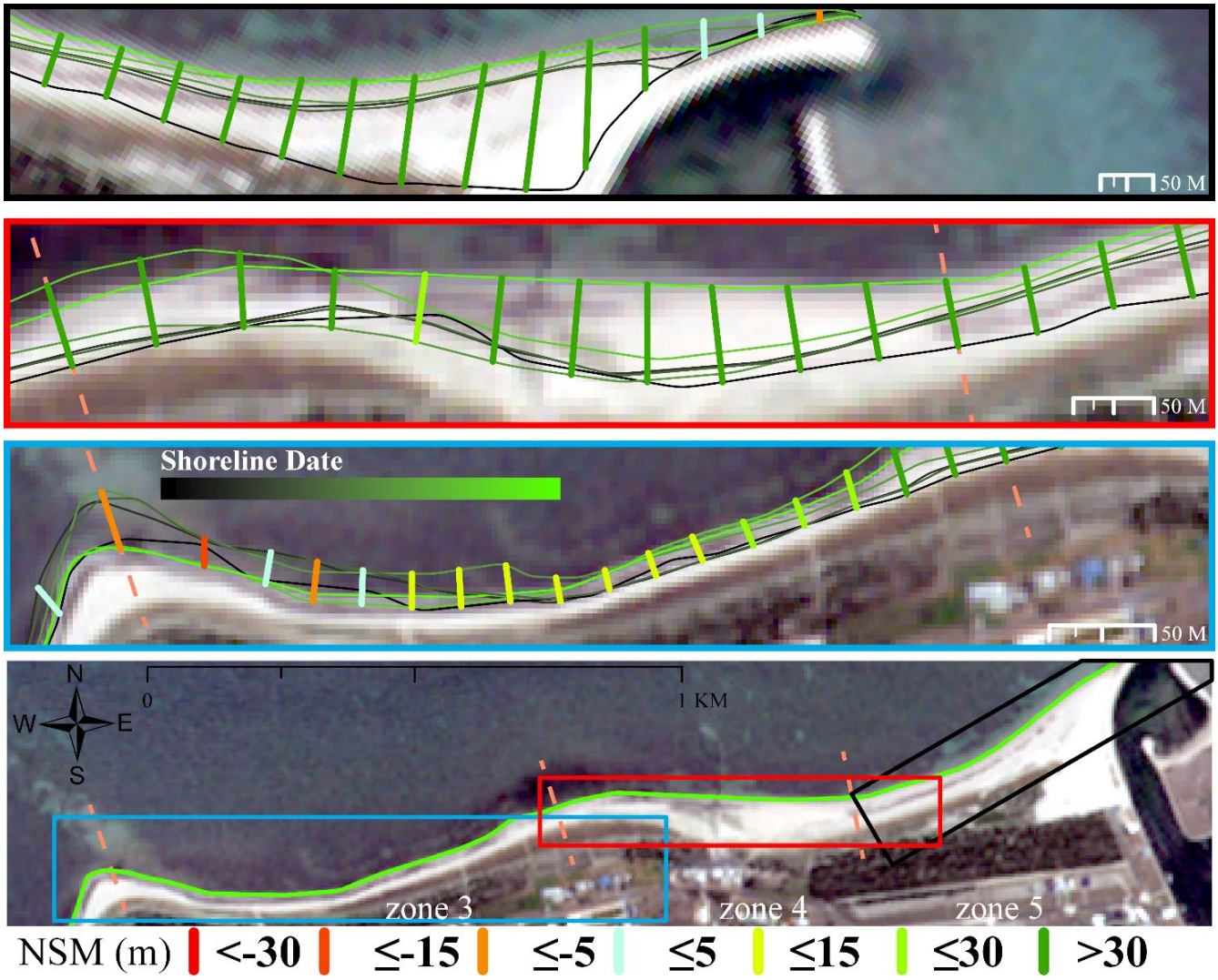

Figure 10 The Instantaneous Water Line (IWL) as derived from the RapidEye satellite imagery, illustrating the levels of Net Shore Movement (NSM) to the west of the Cape Jaffa Marina, zones 3-5, over the decade since construction (2009-2019). Shoreline proxies are presented from Black to Green, with oldest proxy within time series coloured black and most recent approaching light green.

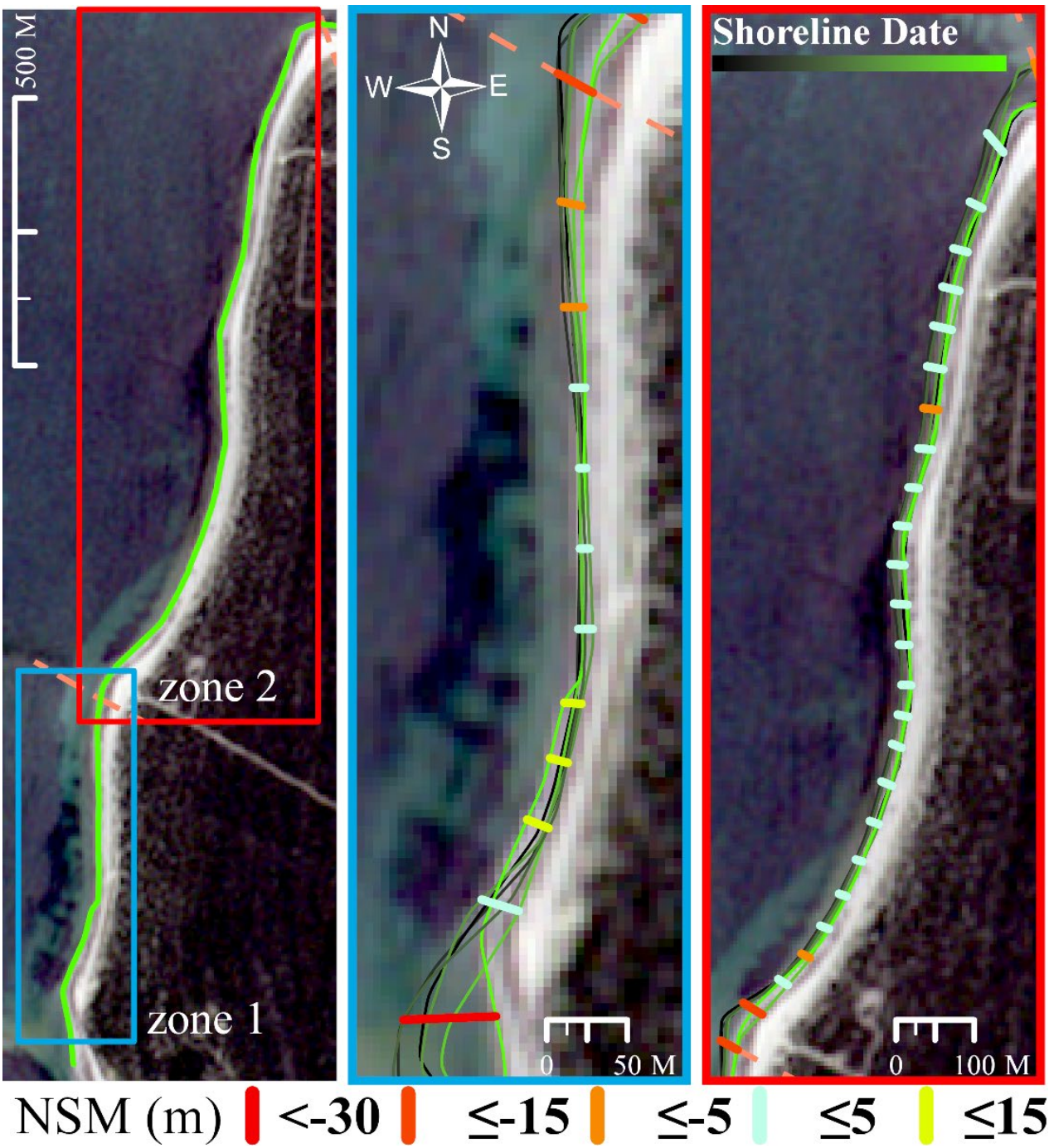

Figure 11 The Instantaneous Water Line (IWL) as derived from the RapidEye satellite imagery for zones 1 and 2, showing the Net Shore Movement (NSM) experienced for the time series (2009-2019). Shoreline proxies are presented from Black to Green, with oldest proxy within time series coloured black and most recent approaching light green.

4.2.2 Intra-Annual (21/04/2018 to 16/05/2019)

The range of the DSAS statistics from the 80 transects at 50 m intervals on the western edge of the marina (Table 10) and from the 69 transects on the eastern edge of the marina (Table 11) show the overall morphological trends of the analysed shorelines during ~1 year. The majority of the transects on the eastern side of the marina, displayed in Figure 12B and 13 show a shoreline experiencing significant erosion across the 3 km between zones 6 and 8. The spike in the Linear Regression Rate (LRR) and corresponding deposition shown in the Net Shore Movement (NSM) as exhibited in the first transects of zone 6 are a result of beach nourishment that occurred as a product of dredge works that occurred from August 2018 to clear sediment build up in the marina entrance. Conversely, the 5 kilometres of shoreline to the west of the marina show more variability between erosion and accretion trends and a less distinct erosional trend with significantly accretional transects mainly located in zone 4, as shown in figures 12A and 14. The NSM of the IWL for the zones 1 and 2 are shown (Figure 15) to have mainly been characterised by erosional cross-shore transects, with the largest negative NSM transect at the at the sand wave feature located at transect 1 (Fig 12 & 15).

Although the eastern edge of the marina received nourishment from August 2018 onwards, the majority of the cross-shore transects were classified as erosional. The average rates of change (LRR) on the eastern side of the marina is -4.48 m/yr for the Instantaneous Water Line (IWL) and -2.22 m/yr for the Edge of Vegetation (EV). The IWL showed that from the earliest transect to the oldest the average rate of change was an average of -8.97 m/yr (EPR) across an average Shoreline Change Envelope (SCE) of 16.85 m while the EV had a much reduced but still erosional trend (EPR average of -2.95 m/yr across a mean SCE of 6.83 m). The average NSM for the IWL was -9.47m and -3.59m for the EV. Of the 69 IWL transects, 64 were categorised erosional by the NSM and EPR with a similar percentage (93%) of erosional transects reported for the EV. The LCI averages were comparatively higher than previous time series due to the large variability of shoreline positions across a year, with an average LCI of 4 for the IWL and 1.95 for the EV. As a result of the large variability of the shoreline movement and corresponding high LCI, few (<4) of the IWL or EV shorelines experienced a statistically significant linear erosion/accretion rate.

While the western edge of the marina experienced an on average negative LRR for the IWL of -.38 m/yr, the EV experienced an average progradation of .97 m/yr (Figure 12A). The EPR of the IWL was recorded -5.57 m/yr over an average NSM of -5.95 m while the EV saw an average EPR of -.27 m/yr across an average NSM of -.29 m. The measure of variability showed that over the 80 transects evaluated, the SCE for the IWL was an average 18.03 m and 11.67 m for the EV. The spike in the LRR as seen in Figure 12A of the EV and the IWL was influenced by accretional transects located in zone 4 where a large in-fill of sand over the winter months resulted in a substantially pro-graded beach (Figure 14) with the EV following behind. Similar to the eastern part of the study area, the average LCI values were of a higher magnitude, 3.43 for the IWL and 2.46 for the EV, indicating that there was a highly variable rate of change and few transects experiencing statistically significant rates.

Table 10 Ranges of statistics compiled for the PlanetScope annual time series on the western side of the Cape Jaffa Marina, zones 1-5. Statistics shown are Linear Regression Rate (LRR), End Point Rate (EPR), Shoreline Change Envelope (SCE), and Net Shore Movement (NSM). Total transects classified as Erosion (ER), Accretion (AC) according to IWL data.

	LRR (m/yr)		**EPR (m/yr)**		**SCE (m)**	**NSM (m)**	
	Er (31)	Ac (49)	Er (68)	Ac (12)		Er (68)	Ac (12)
EV	-15 to -.2	.1 to 37.7	-28.9 to -.1	.5 to 32.5	4.2 to 38.9	-30.8 to -.1	.6 to 34.7
IWL	-27 to -.05	.17 to 40.93	-43 to -.1	.1 to 35.66	7.5 to 47.4	-46 to -.1	.1 to 38.1

Table 11 Ranges of statistics compiled for the PlanetScope images on the eastern side of the marina, zones 6-8. Statistics shown are Linear Regression Rate (LRR), End Point Rate (EPR), Shoreline Change Envelope (SCE), and Net Shore Movement (NSM). Total transects classified as Erosion (ER), Accretion (AC) according to IWL data.

	LRR (m/yr)		**EPR (m/yr)**		**SCE (m)**	**NSM (m)**	
	Er (62)	Ac (7)	Er (64)	Ac (5)		Er (64)	Ac (5)
EV	7 to -.1	.06 to 1.9	-8.6 to -.1	.1 to .77	3.2 to 12.8	-8.3 to -.1	.1 to .7
IWL	-12.7 to -.4	2.8 to 38	-18.9 to -1	.5 to 13	7 to 69	-20 to -.9	.6 to 13.9

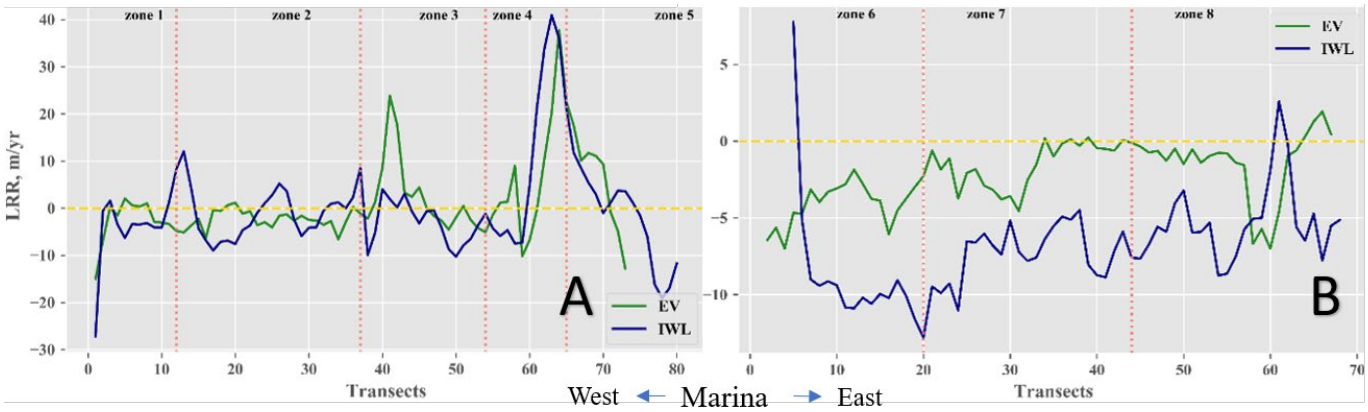

Figure 12 Comparison of the LRR of the EV and IWL for the intra-annual time series of shorelines sourced from PlanetScope imagery, represented by zones 1-5 (Plot A) to the west of the marina and zones 6-8 (Plot B) on the eastern side.

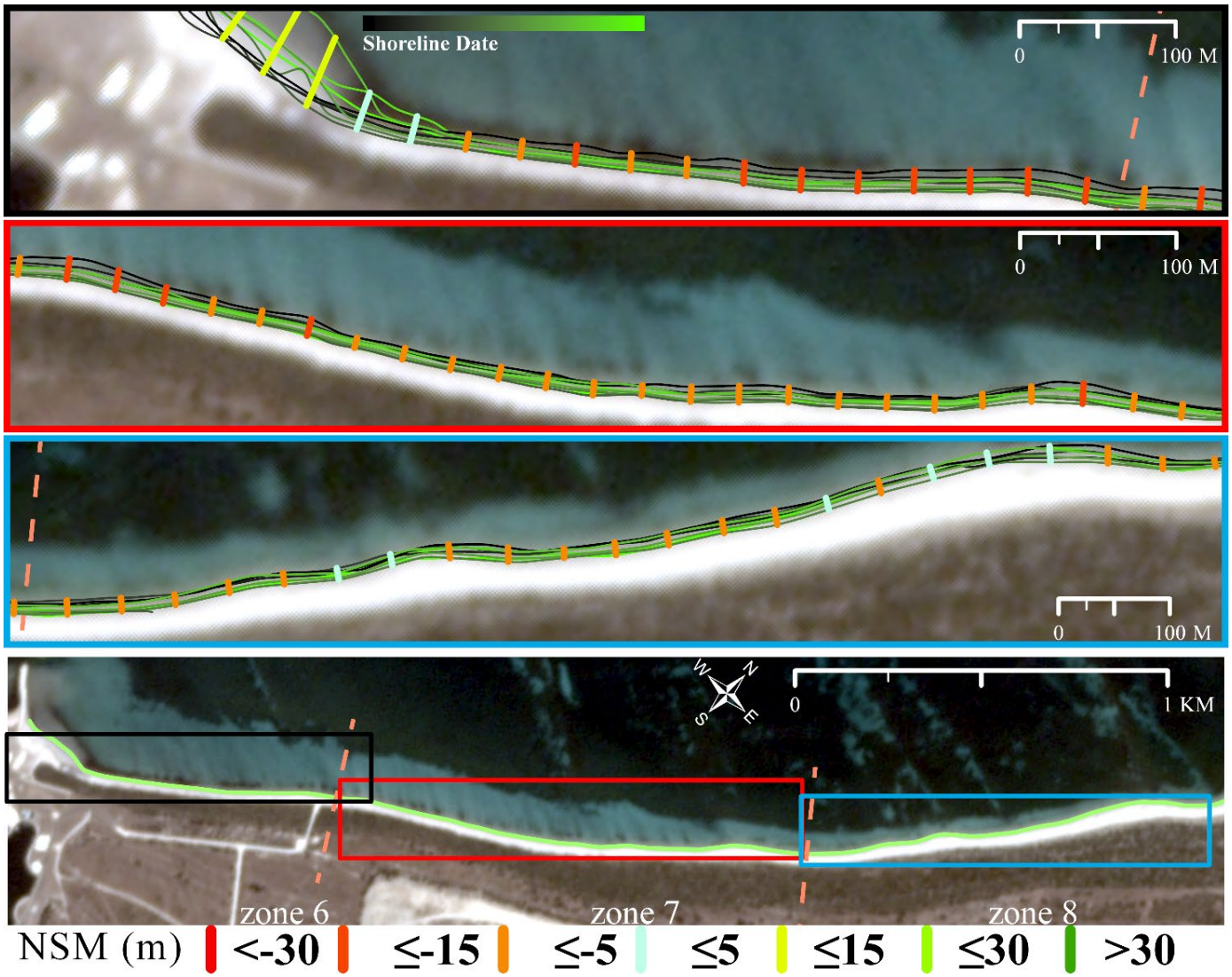

Figure 13 The 3 kilometres of beach to the east of the Cape Jaffa Marina. The transects of the NSM for the IWL represents the amount of change experienced over one year, with shades of green representing depositional transects while yellow to red represent erosional transects. Shoreline proxies are presented from Black to Green, with oldest proxy within time series coloured black and most recent approaching light green.

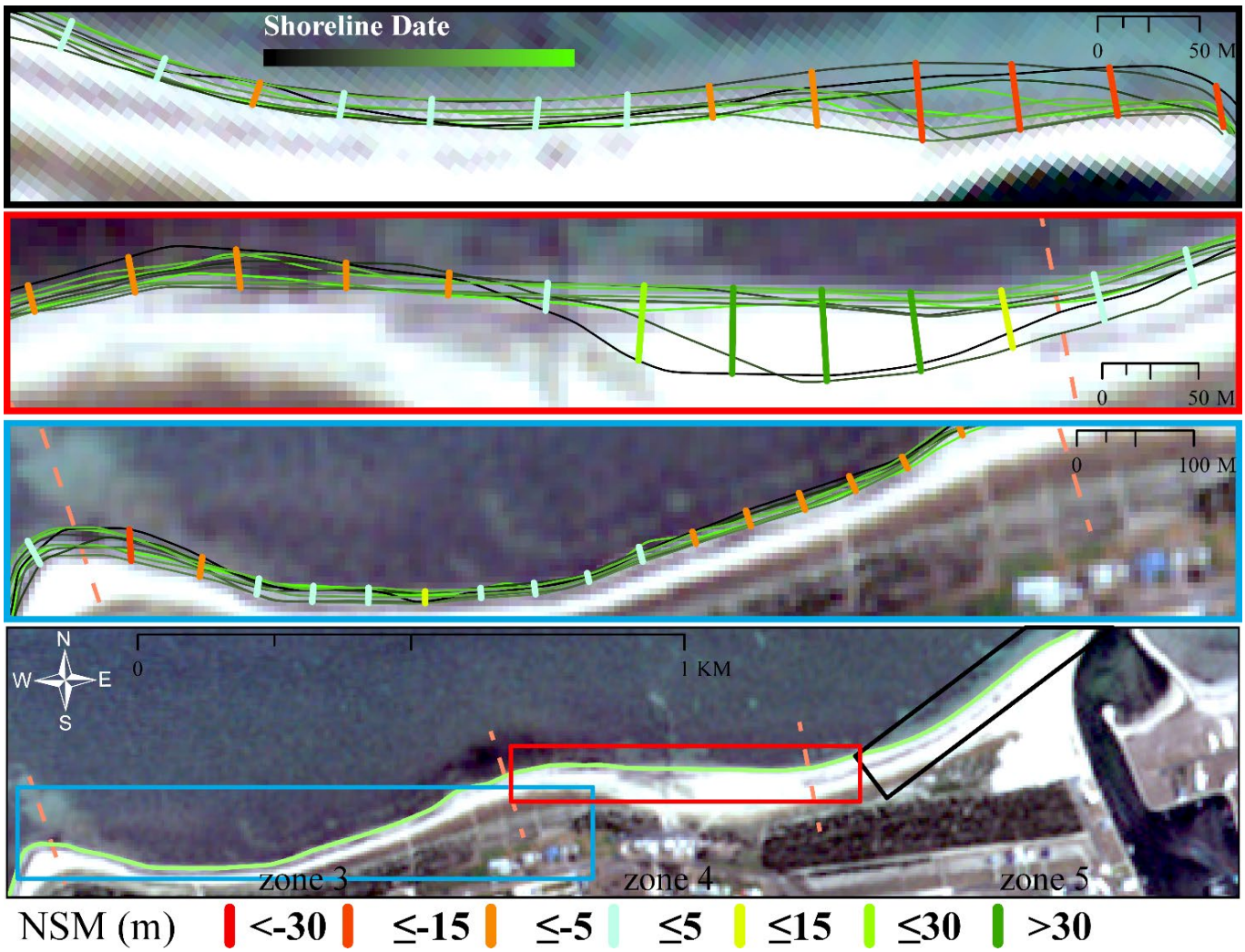

Figure 14 shows the resulting shoreline change to the west of the Cape Jaffa Marina. The IWL proxies as extracted from PlanetScope images from April 2018 to May 2019. The transects of the NSM for the IWL represents the amount of change experienced over one year, with shades of green representing depositional transects while yellow to red represent erosional transects. Shoreline proxies are presented from Black to Green, with oldest proxy within time series coloured black and most recent approaching light green.

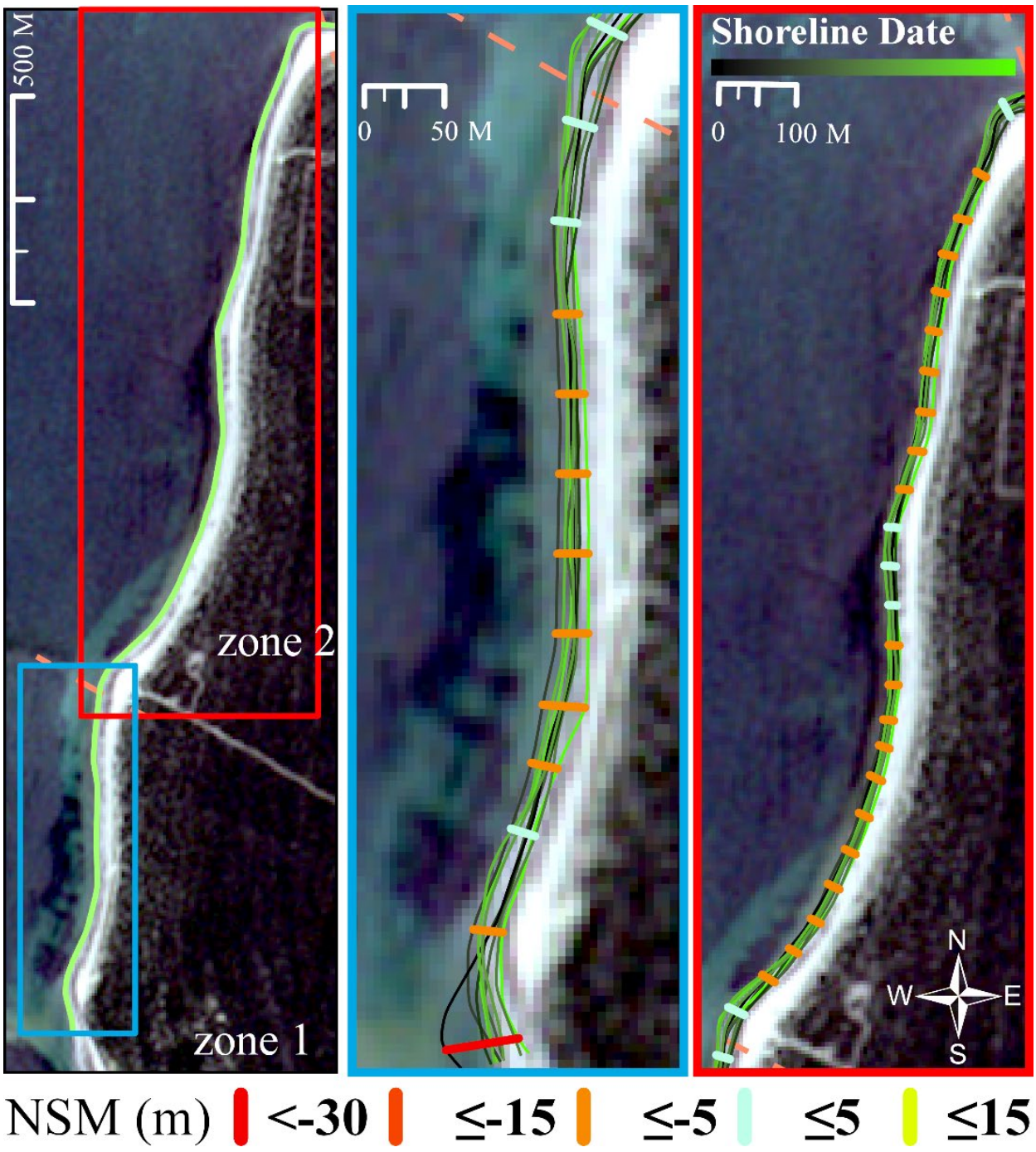

Figure 15 shows the resulting shoreline change to the west of the Cape Jaffa Marina. The IWL proxies as extracted from PlanetScope images from April 2018 to May 2019. The transects of the NSM for the IWL represents the amount of change experienced over one year, with shades of green representing depositional transects while yellow to red represent erosional transects. Shoreline proxies are presented from Black to Green, with oldest proxy within time series coloured black and most recent approaching light green.

4.2.3 Seasonal Variability (21/04/2018 to 22/08/2018)

The results from the shoreline change analysis on the Instantaneous Water Line (IWL) and Edge of Vegetation (EV) for the winter storm season are presented in Table 12. The rate of change statistics for both the eastern and western time series is significantly higher than previous time series assessments due to the observed rapid shoreline adjustment. The drastic morphological changes occurring across the relatively short time period is reflected in the high erosion rates of the LRR across the study area and is illustrated in Figure 16. The net effects of the winter storm season are shown in Figures 17, 18 and 19 by the classification of the Net Shore Movement (NSM). The comparatively higher LCI values (10.89 for the western transects and 11.18 for the east) to the other time series reflect the short observation period and rapid shoreline adjustment occurring during the winter season, further suggesting that the high rates of uncertainty (LCI) depict a dataset where a linear regression model would poorly describe the observed change. The high temporal resolution of this time series has demonstrated the typical shoreline response to storm events, erosional, except in the case of the transects closer to the marina training walls where sediment migration has been impeded (zone 4 Figure 18).

The western side of the marina was mostly characterised by negative distance transects (Figures 18 and 19), except those in close proximity to the Cape Jaffa Marina, with 69 of 80 classified erosional by the NSM and EPR. Across zones 1-5, the rate of change of the IWL was an average -10.73 m/yr (LRR) and -.78 m/yr for the EV. The mean SCE, the measure of shoreline position variability, for the IWL was 14.67 m and 8.72 m for the EV. Of the transects evaluated on the western side of the marina, 19 experienced a statistically significant erosion trend and 2 an accretion trend (zone 4), with none of the EV transects experiencing statistically significant patterns.

Overall the eastern edge of the marina, zones 6-8, demonstrated erosional trends (Figure 17). All 68 transects evaluated were classified as erosional by the EPR and NSM. The average rate of change of the IWL was -17.38 m/yr (LRR) and -9.17 m/yr for the EV. The LCI values were similarly high, with an average of 11.18 for the IWL and 4.55 for the EV. The averages of the EPR were significantly higher than the LRR, suggesting that high temporal data had a varied rate of change between observations (-35.46 m/yr for the IWL and -11.45 for the EV). Although all transects to the

east of the marina were evaluated by the NSM to be erosional, the consideration of uncertainty of the observation to the regression rate (LCI), suggested that only 10 of 68 transects of the IWL and 21 of the EV experienced a significant trend of erosion.

Table 12 Range of statistics from the IWL analysis of the PlanetScope time series of the winter-storm season to the east of Cape Jaffa Marina. Statistics shown are Linear Regression Rate (LRR), End Point Rate (EPR), Shoreline Change Envelope (SCE), and Net Shore Movement (NSM). Total transects classified as Erosion (ER), Accretion (AC).

	LRR (m/yr)		EPR (m/yr)		SCE (m)	NSM (m)	
	Er (79)	Ac (12)	Er (89)	Ac (2)		Er (89)	Ac (2)
EV	-24 to -.25	.94	-30 to -3	1.75	.55 to 12	-10 to -.1	.55
IWL	-52 to -.7	.3 to 3.8	-70 to -13.9		6.8 to 24	-24 to -4.7	.2 to 1.79

Table 13 Range of statistics from the IWL analysis of the PlanetScope time series of the winter-storm season to the west of Cape Jaffa Marina. Statistics shown are Linear Regression Rate (LRR), End Point Rate (EPR), Shoreline Change Envelope (SCE), and Net Shore Movement (NSM). Total transects classified as Erosion (ER), Accretion (AC).

	LRR (m/yr)		EPR (m/yr)		SCE (m)	NSM (m)	
	Er (58)	Ac (22)	Er (69)	Ac (11)		Er (69)	Ac (11)
EV	-51.6 to -.2	.3 to 32	-63 to -.1	.8 to 28	1.9 to 31	-21 to -.05	.3 to 9.4
IWL	-105 to -.17	.94 to 124	-101 to -.15	.8 to 103	5.2 to 41	-34 to -.05	.3 to 34.6

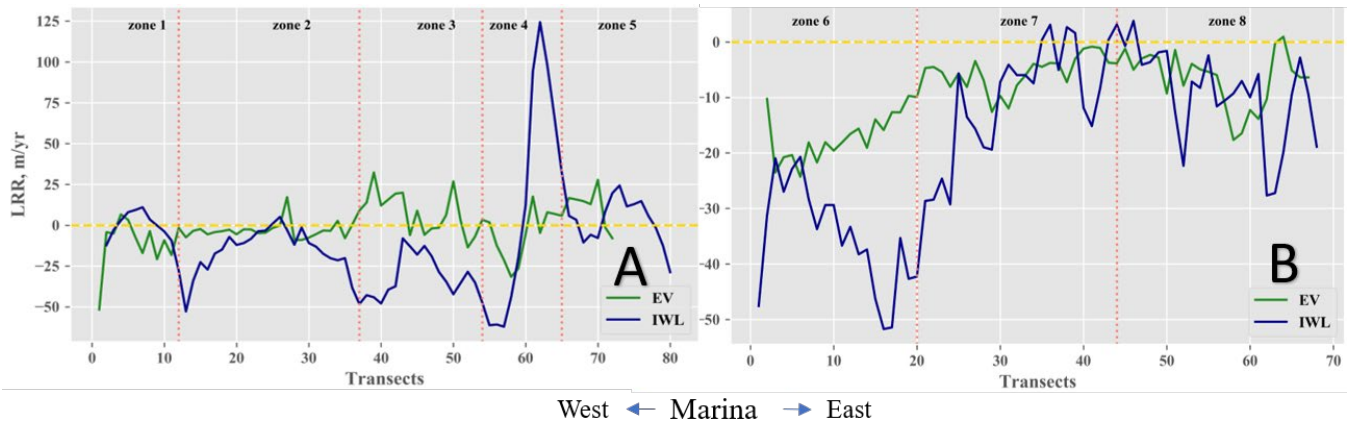

Figure 16 Rate of change statistics from transects of shoreline change of the EV and IWL from the PlanetScope time series examining the shoreline change from April 2018 to August 2018. Plot A representing zones 1-5 on the to the west of the marina and Plot B showing the LRR to the east of the marina (zones 6-8).

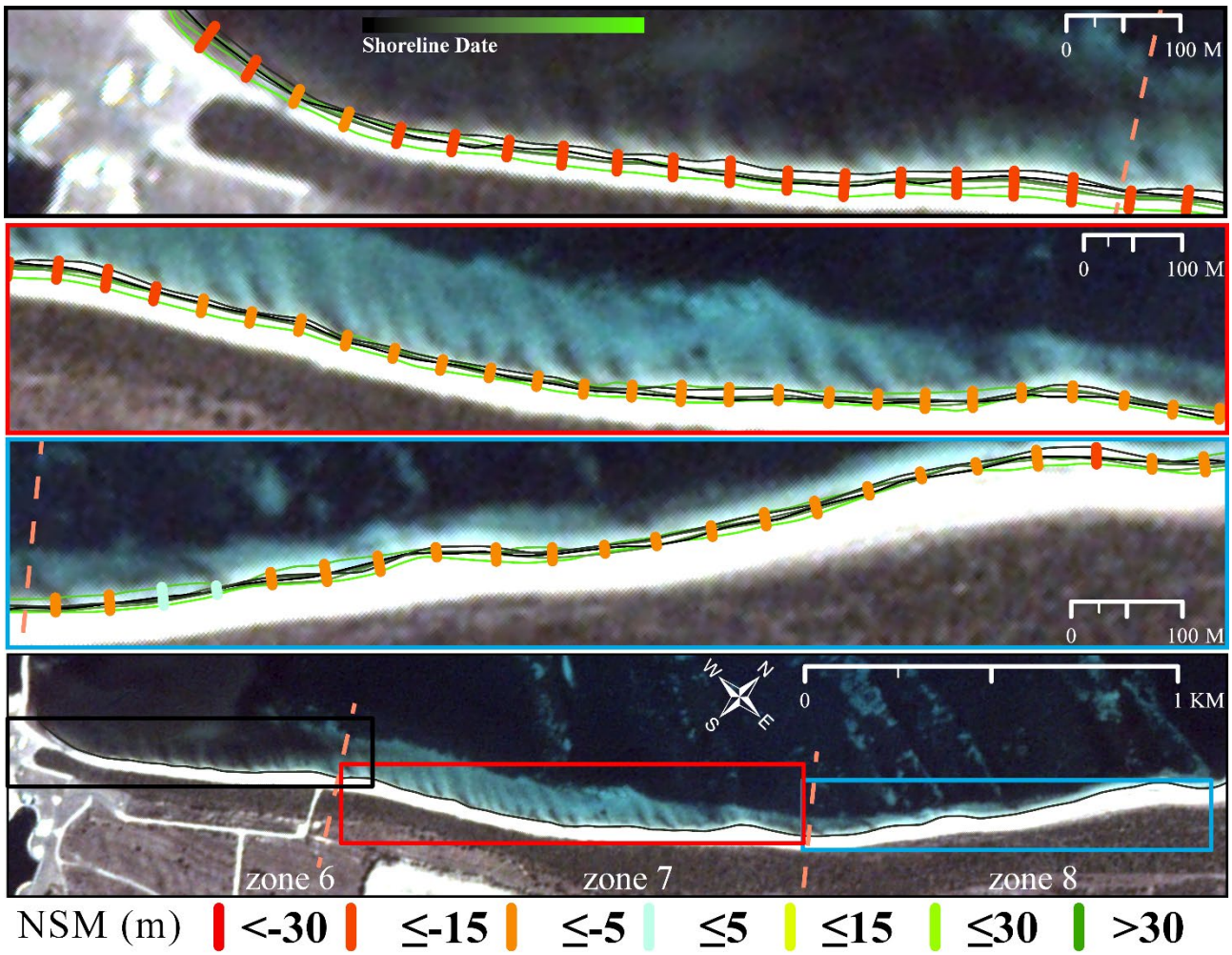

Figure 17 The 3 kilometres of beach to the east of the Cape Jaffa Marina. The transects of the NSM for the IWL represents the amount of change experienced over the months between April and August of 2018, with shades of green representing depositional transects while yellow to red represent erosional transects. Shoreline proxies are presented from Black to Green, with oldest proxy within time series coloured black and most recent approaching light green.

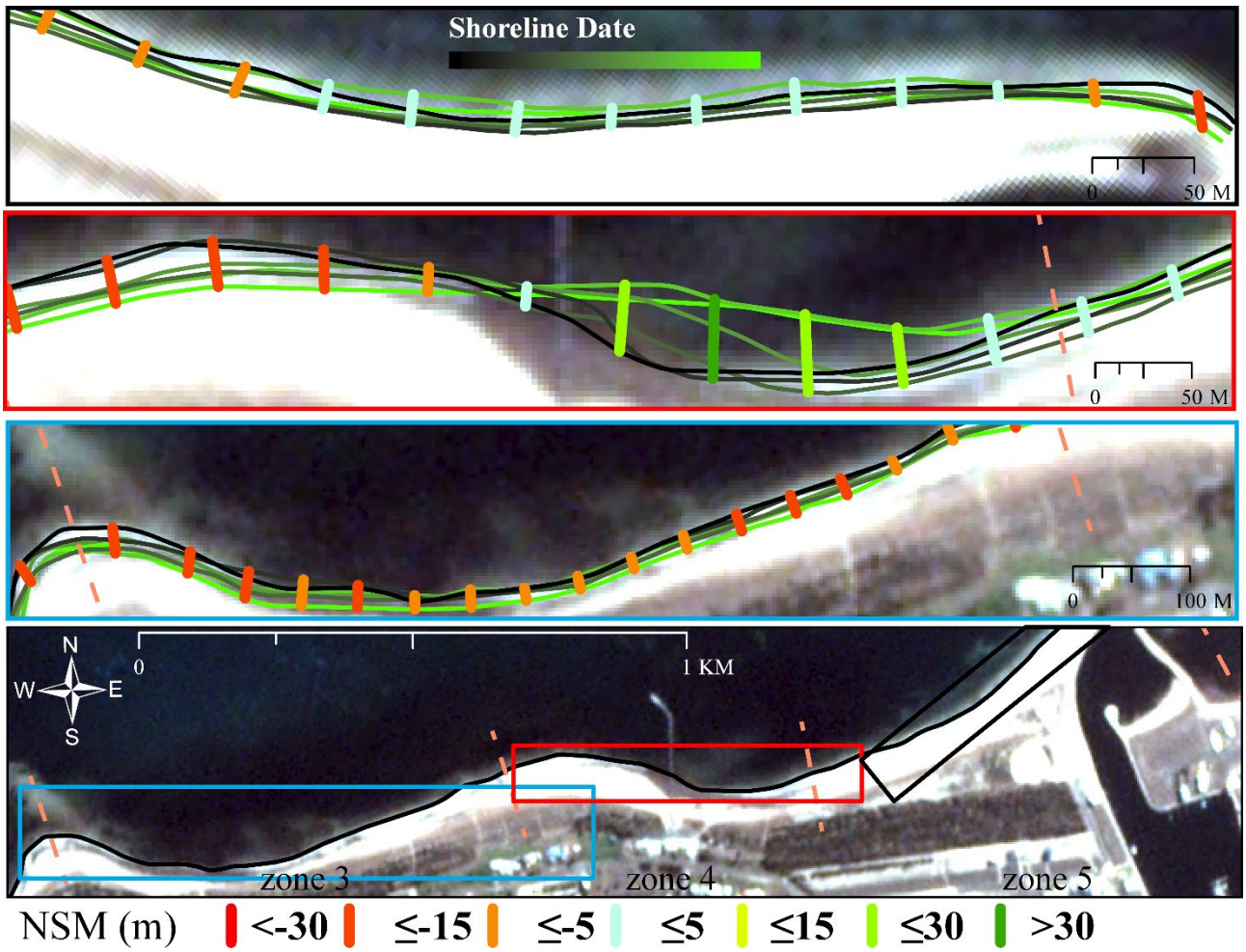

Figure 18 The 3 kilometres of beach to the west of the Cape Jaffa Marina. The transects of the NSM for the IWL represents the amount of change experienced over the months between April and August of 2018, with shades of green representing depositional transects while yellow to red represent erosional transects. Shoreline proxies are presented from Black to Green, with oldest proxy within time series coloured black and most recent approaching light green.

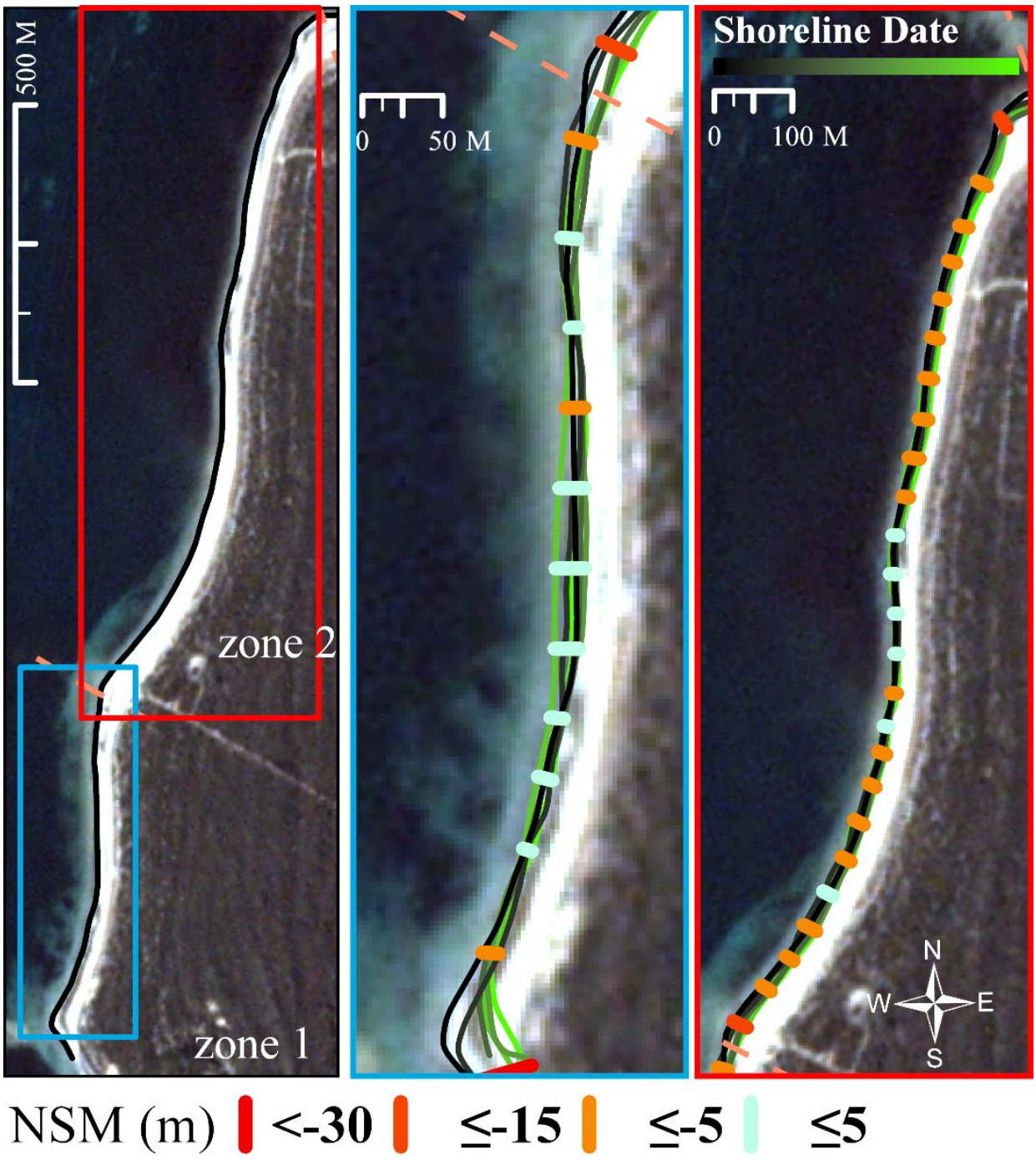

Figure 19 The western facing beaches of zones 1 and 2 with the transects of the NSM for the IWL. Illustrates the amount of change experienced over the months between April and August of 2018, with shades of green representing depositional transects while yellow to red represent erosional transects. Shoreline proxies are presented from Black to Green, with oldest proxy within time series coloured black and most recent approaching light green.

4.3 Seasonal Variability UAV Derived (25/04/2019 to 30/08/2019)

The digitised IWLs from the UAV surveys were compared in a shoreline change analysis of 167 transects oriented transverse to the coast at 5 m intervals. The results (Figure 20) show that the 130 metres on the western part of the analysed shoreline has retreated an average -4.67 m (NSM), while the rest of the transects pro-graded with an average NSM of 14.33 m. The visible trend of accretion can be seen in Figure 16, where sediment has likely been transported eastward over the course of the winter storm season and accumulated towards the groynes of Cape Jaffa marina. Of the 167 transects, 26 were classified as erosional by the NSM and EPR and 141 accretional. An examination of the trends of the LRR suggest that few transects have experienced statistically significant rates of change, 20 accretional and 0 erosional. This suggests that there has been a variable rate of change rather than a linear trend and that the shoreline's position has been dynamic over the course of the study. The rate of change calculated by the analysis of the LRR showed relatively high rates of change for both the erosional and accretional transects, the erosional transects had an average rate of change of -12.59 m/yr while the accretion transects experienced a higher mean rate of change of 42.43 m/yr.

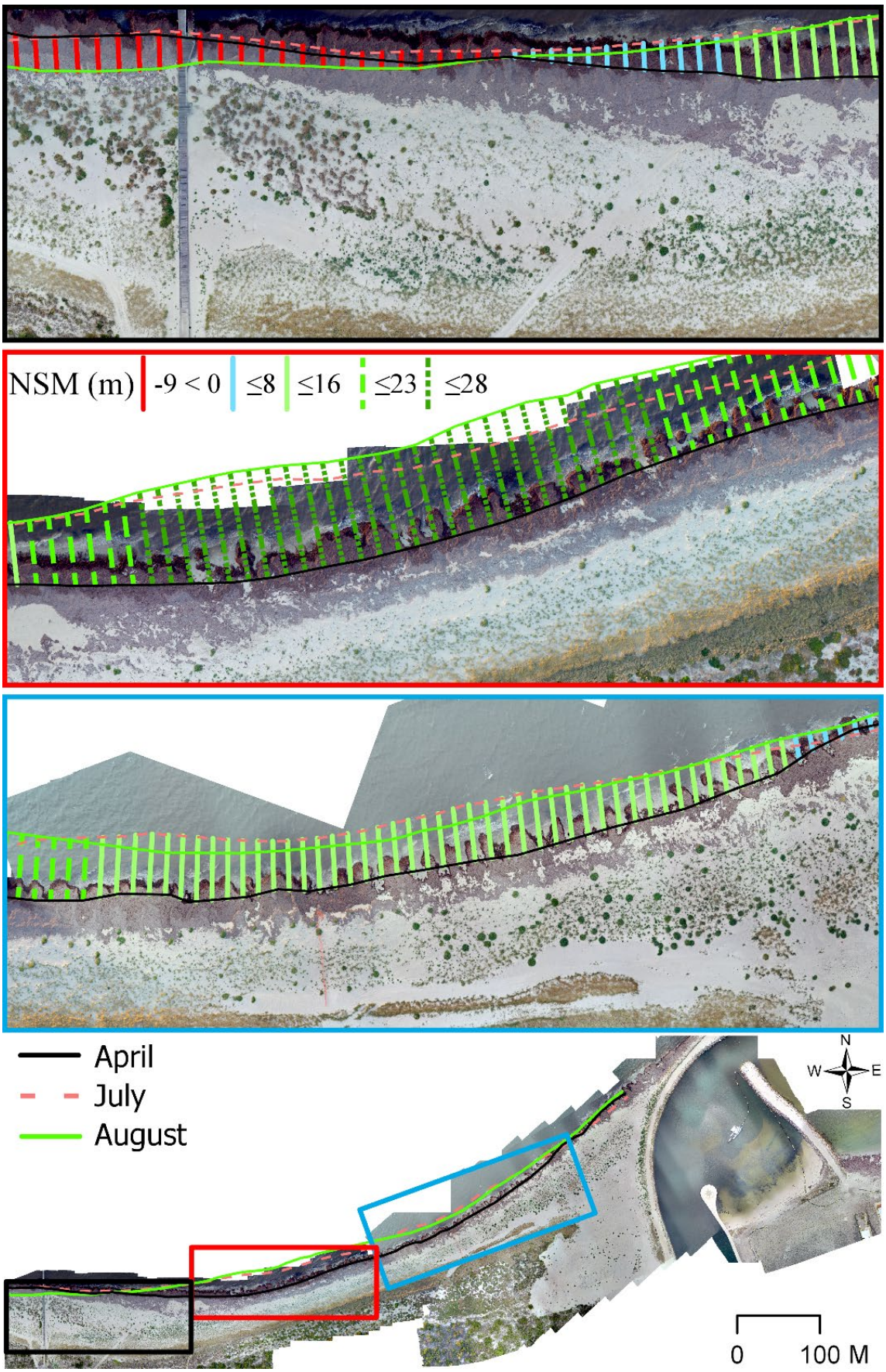

Figure 20 IWL shoreline proxies sourced from UAV surveys from April, July and August of 2019. Cross-shore transects representing the NSM signifying areas of erosion and accretion overlain over an orthomosaic from the April survey.

4.4 Shoreline Validation

Figure 21 shows the results of the comparison between the automated shoreline extraction from the CubeSat satellite images and the high-resolution orthomosaics created from UAV surveys. The results show that the shoreline proxies sourced from the PlanetScope satellite images are within 1-2 pixels of the digitised IWL on the orthomosaics. The results further illustrate that the automatically extracted EV line sourced from the PlanetScope images is falling within the mixed pixels of sand and shallow rooted primary colonising grasses, mainly Thinopyrum Junceiforme (Sea Wheat-Grass).

Figure 22 shows the results of the shoreline extraction from concurrent images of RapidEye and PlanetScope satellites, collected on January 24, 2019. Considering the differing spatial resolutions (3m vs 5m) of the satellite systems, the resulting extracted shoreline vectors are within a single pixel.\

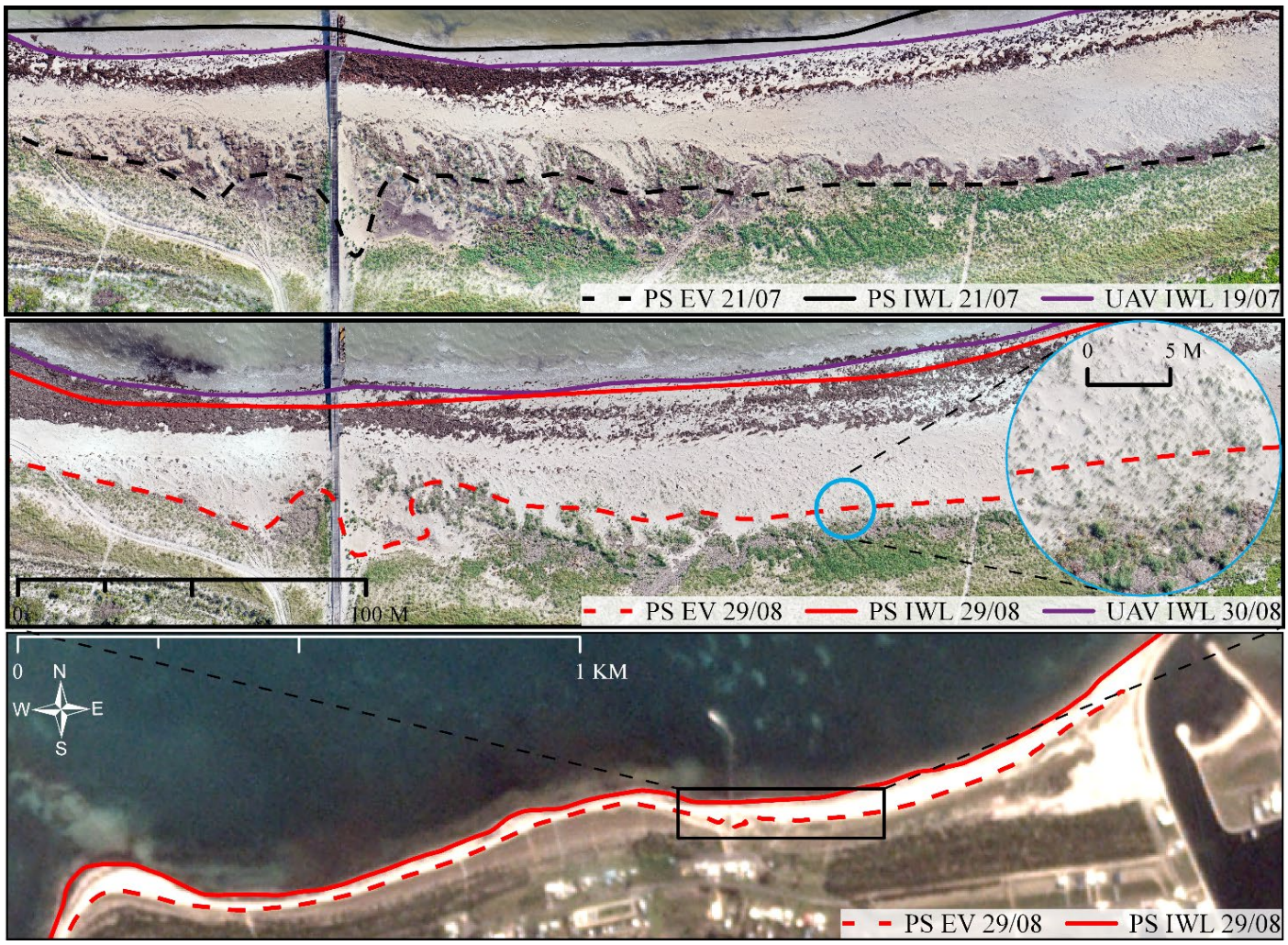

Figure 21 Top 2 panes are shoreline proxies digitised from UAV orthomosaics collected on 19/07/2019 and 30/08/2019 with shoreline proxies extracted from PlanetScope imagery from 21/07/2019 and 29/08/2019. Comparison of difference shows less than 2-pixel size difference between UAV and satellite extracted proxies.

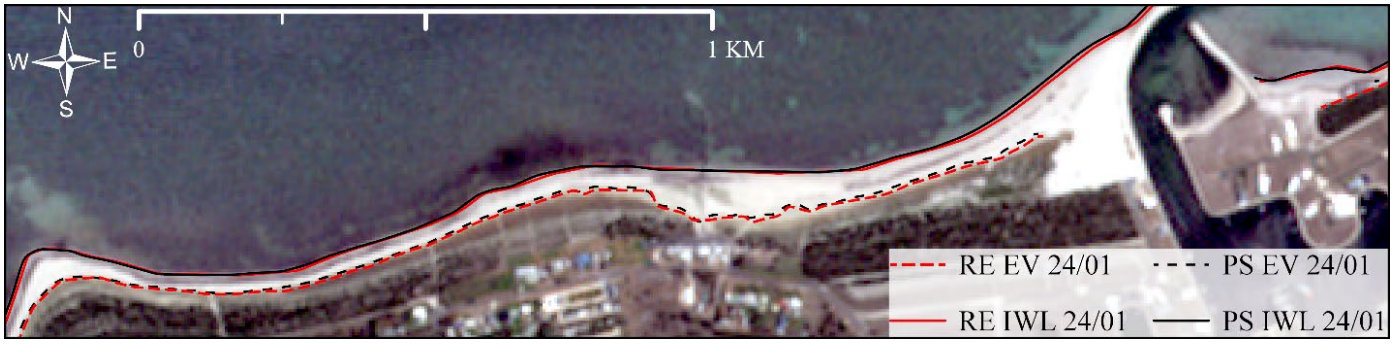

Figure 22 Shoreline proxies automatically extracted from RapidEye (RE) and PlanetScope (PS) imagery that were both collected on 24 January 2019. Shorelines are within 1-2 pixels across study area.

5. DISCUSSION

Although Lacepede Bay at the south end of the Coorong region is characterised by a relatively low wave-energy environment, the barrier effects of the constructed groynes on the longshore sediment transport has significantly impacted the region's shoreline. The effects of similarly constructed groynes on shoreline morphology have been extensively documented by the literature (Carter, 1988; Komar. 1998) with some coastal management schemes resolving to implement passive real-time monitoring systems with stationary cameras and management programs with responsive sand-pumping systems (Brayshaw & Lemckert, 2012) to minimise the effects of blocking the longshore current. This study presents an assessment of shoreline change over a number of temporal scales for the beaches surrounding Cape Jaffa and the constructed marina. Imagery collected over the past 44 years reveals considerable shifts in shoreline position and the array of temporal resolutions informs of the time-scale dependent rates of change. The overall results of the shoreline change analysis throughout this study are presented in Appendix 3, which displays the Net Shore Movement (NSM) of the Instantaneous Water Line (IWL). The results of this study show that the location and rates of change of the Edge of Vegetation (EV) shoreline proxy mirrors the shoreline trends of the IWL. Across the varying temporal scales, there is a distinct pattern per region within segments of the study area (groups 1 to 3 of Appendix 3), showing that the shoreline dynamics are responding to its relative location and orientation. The (A) panes within Appendix 3 illustrate the shoreline trends of the region pre-construction of the marina as long-term accretional and erosional patterns with a relatively small magnitude of shoreline change as shown by the NSM over a 30-year time period. The images on panes B to D in Appendix 3 illustrate how the shoreline has evolved since the construction of the marina with the varying time scales and frequency of observations. These are characterised by contrasting but significant shifts in shoreline position occurring in groups 2 and 3 as the barrier effects on the littoral drift takes place. The similar results of the shoreline proxies derived from the 2019 winter-storm season by UAV surveys further illustrate the migration of sediment alongshore as sand waves and its subsequent trapping behind the marina. The validation of the automatically extracted

shoreline proxies by in-situ UAV observations further supports the monitoring of shoreline positions and trends with CubeSat sourced observations.

5.1 Pre-Marina Shoreline

The results of the analysis of shoreline change trends from 1975-2005 illustrates a coastline showing dominant accretional trends in zones 1-4 with transects in zone 5 experiencing a slight erosional trend (Figure 4). The analysis of the pre-marina time series that extends into zones 6-8 (Figure 5) was evaluated solely with the Net Shore Movement (NSM) statistic, as shown in Appendix 3 (2A and 3A), to show the overall shoreline change for the area as imagery for the intervening years (1987, 1995, 2000) was not available for this study. The negative NSM values indicate that the erosional trend, as shown in Figures 4 and 5, continued into zones 6 and 7 (Appendix 3, panel 3A). The predominantly pro-grading coastline has seen significant accretions of sand in zones 1-5, represented by the greater magnitude of the statistic for variability (SCE) and NSM of the Instantaneous Water Line (IWL) compared to the Edge of Vegetation (EV). Sandy beaches are inherently dynamic systems and are expected to have a greater variability in the erosion/accretion rates for the cross-shore transects of the IWL (Del Rio et al., 2013) as they represent variations in unconsolidated sand, as opposed to the EV on the seawards side of the foredune as it tends to be less susceptible to short-term fluctuations in water level during calm conditions. Nonetheless, a comparison of the mean LRR for accretion/erosion classified transects (Table 14) and the similar rates across the study (Figure 4) shows that the rates of change of the IWL and EV follow similar trends. These trends provide an indicative analysis of the rate of changes that the pre-marina shoreline experienced and indicates that the long-term trends of the shorelines are a result of the local forcing conditions of the hydrodynamics and its interaction with a sandy coastline, similar to the findings of Ribas et al. (2013).

One potential explanation of the accretional nature of shorelines pre-construction of the marina is from Hilton et al. (2006) who suggests that Sea-Wheat Grass, the invasive perennial rhizomatous grass visible in the circular inset of Figure 21, was not present in the region in 1975 when the first image in this time series was taken. Hilton et al. (2006) states that the invasion

timeline of Sea-Wheat grass in the area is not certain, but that it was not present in the established foredunes of the Younghusband Peninsula, the coastal barrier located just to the north in the Coorong region, when Short and Hesp (1980) undertook a study of the area in the late 1970's. Sea-Wheat Grass is thought to have first colonised the South Australian coasts in the mid 1980's and has resulted in substantial shifts in the morphology of foredunes and the corresponding accretional disposition of shorelines that it dominates (Hilton et al., 2006). The morphological impact of Sea-Wheat Grass is a product of its resiliency to tidal inundation and high salinity levels in comparison to native Australian species (Bourman, 2016; Heyligers, 1985; Hilton et al., 2006).

The erosional trends of the transects in zone 5 and the negative distance of the NSM in zones 6-8 confirms the prediction made in Short and Hesp (1984) of areas that would experience shoreline retreat, which was based on the assumption that the subaqueous sand waves would continue to move into Lacepede Bay. Sand waves migrate with the direction of the littoral drift and as shown in Figure 23 and can have a high spatial variability across varying temporal scales. Ribas et al., (2013) reiterates that the wave-like patterns of the sand waves that are visible in the subaerial beach often extend into the near-shore and have a similar morphology that is visible in bathymetric contours. These features cyclically accrete and erode sediment and represent considerable magnitudes of sand (Ashton & Murray, 2006; Ribas et al., 2013) and correspond to the areas of highest change rates across the different temporal resolutions presented in this study. The spatial variability of sand wave features on the western facing beaches are presented in Figure 24 to illustrate the wide spatial envelop that they occupy and insinuate substantial migrations of sand in the longshore processes of the area.

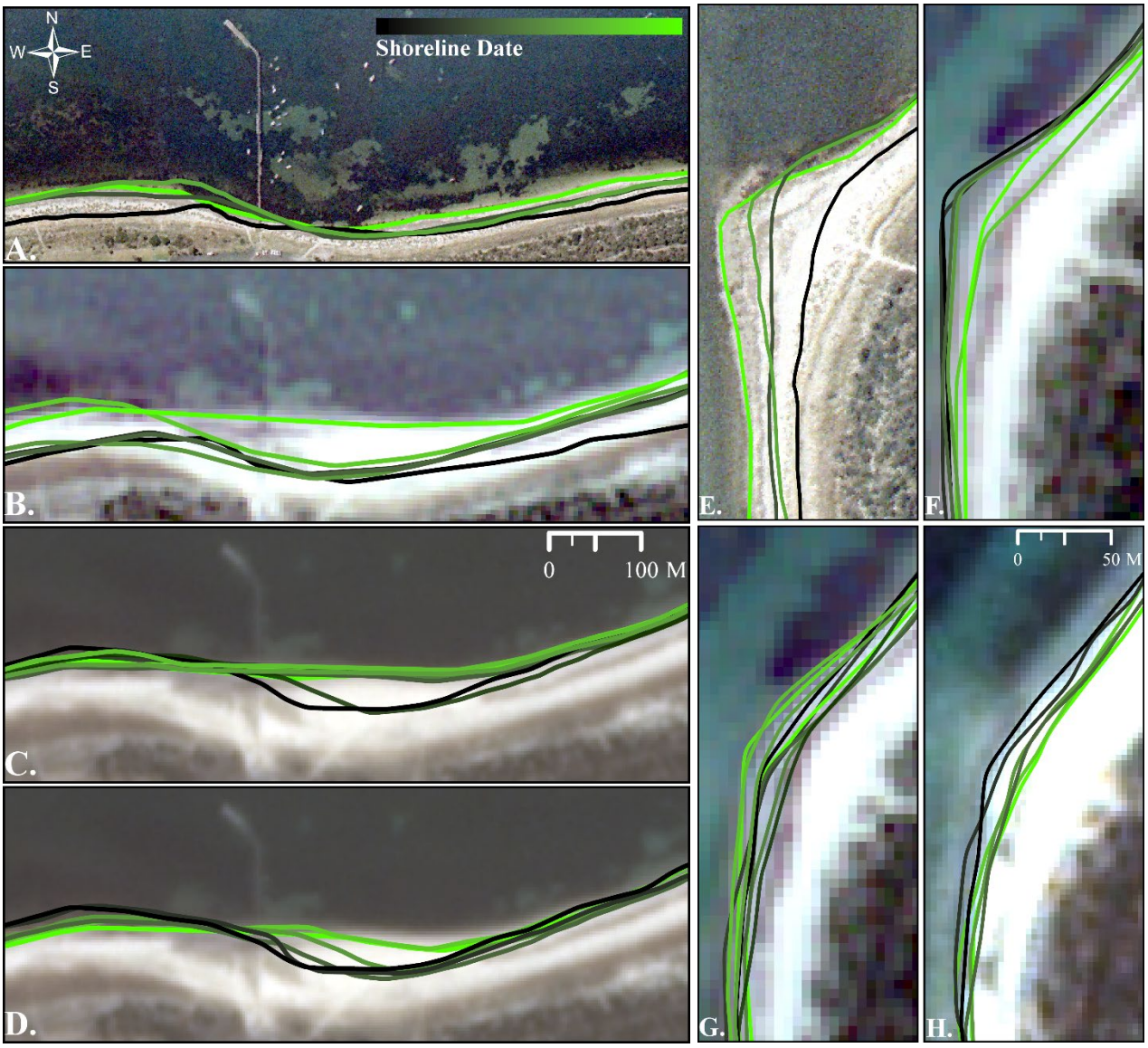

Figure 23 IWLShoreline proxies in front of the Cape Jaffa settlement and on the western facing beach over a sand wave feature with shoreline proxies from individual time series. The shorelines are coloured from black to green based on their relative date, with oldest shorelines within the time series darker and more recent proxies approaching light green. Images (A and E) are from the aerial photos from 2005 with pre-marina shoreline proxies. Below (B and F) is a RapidEye image with proxies from the 2009-2019 time series, PlanetScope annual time series (C and G) and the PlanetScope storm season time series (D and H). Satellite images overlain sensor specific images from 24 January 2019.

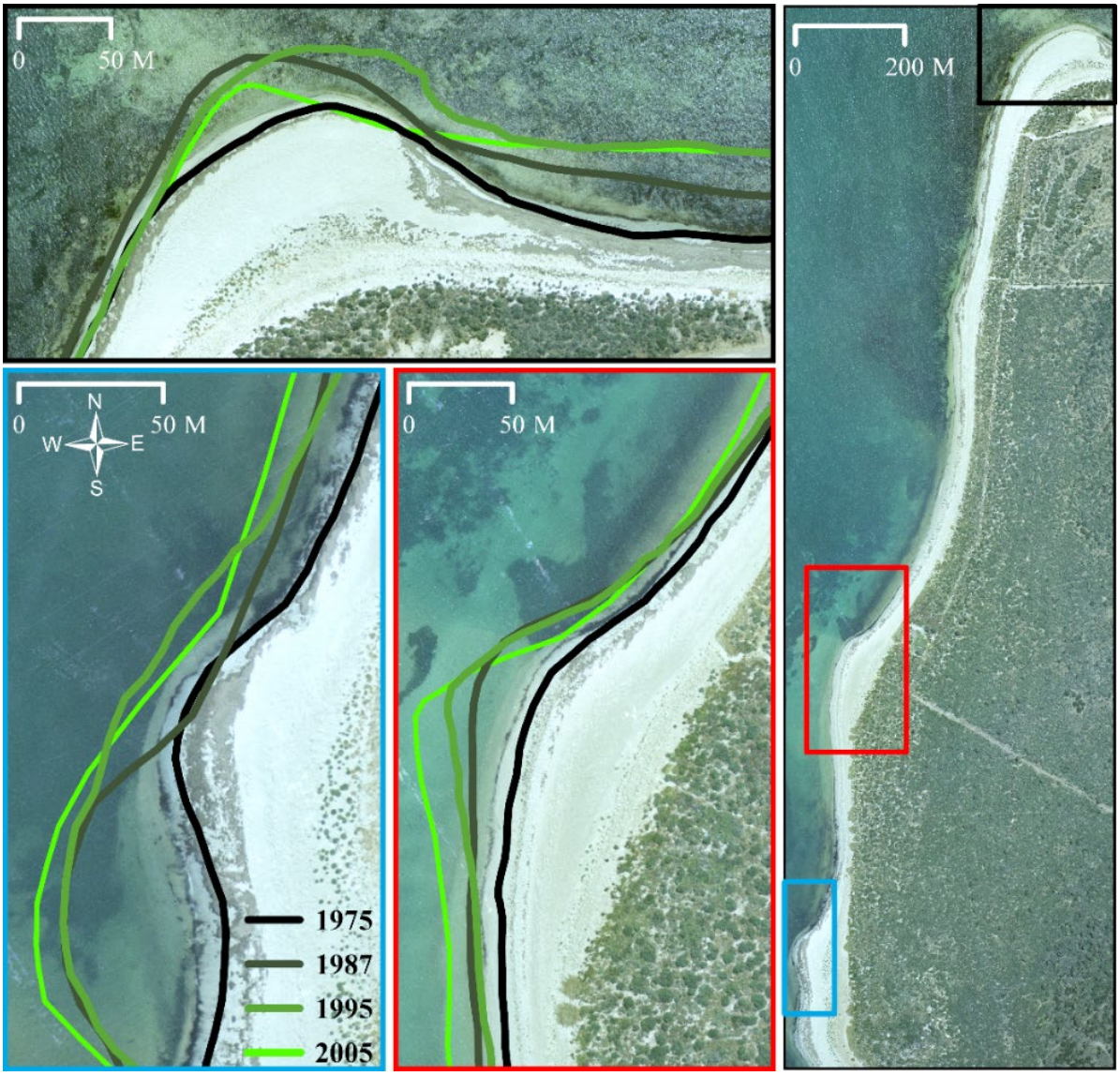

Figure 24 Sand wave features on the western facing beaches, shoreline proxies sourced from airplane derived IWL shorelines. Image is from 1975.

Table 14 Regression rates from the presented time series. Separated by erosion/accretional transects and West(W)/East(E) to illustrate the average rates experienced. Aerial imagery from 1975-2005. RapidEye (RE) imagery from 2009-2019. PlanetScope (PS) Annual 21/04/2018 to 16/05/2019 and PS Storm 21/04/2018 to 22/08/2018.

		LRR m(yr)	
Source	**Proxy**	**Mean Erosion**	**Mean Accretion**
Aerial	EV	-0.4	0.8
	IWL	-0.2	0.7
RE	EV	W (-1.3), E (-2.8)	W (2), E (.6)
	IWL	W (-1), E (-3.6)	W (3.7), E (.3)
PS Annual	EV	W (-3.6), E (-2.1)	W (7.9, E (1.9)
	IWL	W (-5.9), E (-7.3)	W (8.3), E (20)
PS Storm	EV	W(-51.63), E(-24.3)	W(32.31), E(0.94)
	IWL	W (-24.7), E (-19.6))	W (26), E (2)

5.2 Post-Marina Shoreline

The decade since the marina was constructed has shown a profound temporal and spatial shoreline variability across the 8 kms analysed. The shoreline vectors sourced from the satellite imagery have illustrated the varying effects of the construction of the Cape Jaffa Marina onto the surrounding shorelines, providing an analysis that informs how a beach has evolved over a variety of time frames; seasonally, annually and on a decadal scale. According to Short and Hesp (1982) and Splinter et al. (2016) the characteristic low-wave energy environment and reflective beach types that surround Cape Jaffa typically experience rapid alterations to their shorelines, adjusting their morphology over relatively short timescales from days to weeks. The rapid changes occur during episodic erosional events from storms with high wave-energy and are followed by a corresponding post-storm beach recovery (Wright and Short, 1984, Splinter et al., 2014) if sediment is available. Furthermore, the sediment exchange across reflective beaches has been shown to be highly responsive to changes in wave energy as the sediment is mainly stored in the subaerial beach, accumulating under normal conditions and eroded in high-wave energy conditions (Aagaard et al., 2012). This can be observed across the study area with the high spatial variability in the shoreline proxies of the PlanetScope time series with observations sourced from the winter months and the correspondingly high rate of change (Table 14) statistics for the seasonal and intra-annual time series compared to the lesser rates of change from the inter-annual time series.

The inter-annual shoreline analysis sourced from the RapidEye imagery illustrates a medium-term change analysis with two distinct patterns of shoreline change represented by the western and eastern data sets. The eastern set of data has shown a majority of its cross-shore transects to have experienced a statistically significant erosional trend, with a linear regression fit precisely describing the shoreline retreat. Over time, the barrier effect on the littoral drift from the constructed groynes of the Cape Jaffa Marina has persistently starved the shoreline downdrift, to its relative east, of the sediment that replenishes it. Conversely, the updrift zones (3-5) to the west of the marina have seen distinct accretional trends with substantial progradation and significant increases in the rate of change occurring closer to the constructed groynes of the marina as the sediment that would normally be transported westwards by the predominant longshore current is impeded. The imagery outside of the winter storm season with negligible differences in tide and

significant wave height provides a data set that illustrates the positional change of the shorelines in the study area and highlights the subsequent accelerated rates of change contrasted to the pre-marina shoreline analysis.

The time series analysis of the PlanetScope satellite systems provides a high frequency observational data set that shows the cross-shore variability of the IWL and its response across a year and storm season. Significant shoreline changes have been documented in the analysis of PlanetScope images that focused on the change occurring across a year, with a highly variable rate of change and a non-linear trend as shown in the shoreline vectors of Figure 23 (panels C,D, G and H) and uncertainty statistics presented in the results 4.2.2 and 4.2.3 statistics. Measurements of significant wave height from the Cape du Couedic waverider buoy show that there were at least 7 days within the winter-storm season of 2018 where the significant wave height exceeded 7 m, signifying multiple storm events with pro-longed high-wave energy. The resultant effects are shown in the shoreline retreat in Figure 23 (panels D and H) and in the significantly higher rates of change in Table 14. As expected, the results predominantly illustrate significant rates of erosion across the study area, with a marked spike in the rate of accretion to the west of the constructed groynes at the Cape Jaffa marina as migrating sediment is impeded (Figure 16A). Other areas where the LRR transects reflect a pattern of accretion correspond to the highly variable sand wave features in zones 1, 2, 7 and 8 (Figure 1).

This study applied UAV surveys to measure shoreline change across a storm season at a high spatial resolution and to validate the output from remote sensing techniques by near simultaneous data collection. The application of Structure from Motion (SfM) photogrammetry with high-resolution imagery and geo-referenced ground control points (GCPs) delivers outputs with <2 cm pixel sizes that have been utilised here for a change over time analysis and specifically to measure the significant change to the shoreline. The results further illustrate the effects of a winter storm season with a net retreat of the shoreline on the western end of the survey and that substantial sediment continues to accumulate on the beaches near the constructed groynes (Figure 20). The increasingly accessible and relatively inexpensive UAV technology has led to its extensive use in research environments to assess landscape changes over time at a high spatial resolution (Colomina & Molina, 2014; Drummond et al., 2015). UAV surveys have been

implemented as part of long-term coastal monitoring programs (Clark, 2017; Gonçalves & Henriques, 2015; Johannes et al., 2012) and to analyse shoreline change rapidly after it has occurred (Casella et al., 2016; Ierodiaconou et al., 2016; Turner et al., 2016). Recent research has utilised UAVs to validate classifications within estuarine environments from satellite imagery (Gray et al., 2018) and to source the shoreline proxies for a change over time analysis (Albuquerque et al., 2018; Čermáková et al., 2016; Yoon-Kyung et al., 2019) but the work presented here is the first to employ UAV surveys to both assess shoreline change at a high spatial resolution and to validate an automated remote sensing workflow of an inherently spatiotemporally variable landscape feature such as a shoreline proxy. The results of the validation of the shoreline proxies shows that the satellite extracted shoreline proxies are with 1-2 pixels of the high-resolution derived water line and edge of vegetation, suggesting a relatively small margin of error and providing a definite estimation of error for the vector shoreline analysis (3.5).

5.3 Assessment Of Satellite Imagery

The utilisation of PlanetScope ‘dove’ satellite constellations for earth observation of landscape change has distinct advantages and drawbacks over more established systems. The advertised daily re-visit rate of multi-spectral satellite imagery from Planet (2018) represents a promising improvement over conventional space-based systems (Houborg & McCabe, 2016) for monitoring spatio-temporally variable phenomena such as shorelines. Planet has enabled the increase in spatial and temporal resolutions with the deployment of a multi-satellite constellation approach that utilises small and relatively affordable CubeSat satellites. An additional consideration for space-based earth observation programs arises when the cost per image analysis is done, Sozzi et al. (2018) shows that the relatively low cost of PlanetScope imagery allows for it be implemented at large scales at a significantly lower cost compared to other satellite systems. Inherent to the multi-satellite constellation approach taken by Planet is the continuous launching of new satellites with hardware upgrades resulting in varying capabilities of radiometric calibration across its fleet (Cooley et al., 2017). The continuously expanding fleet and improving technology is allowing more frequent and higher spatial resolution observations that could be

incorporated into an automated monitoring system that provides frequent observations at a high spatial scale at a large scale if current limitations are addressed (Cooley et al., 2017; Houborg & McCabe 2016; Houborg & McCabe, 2018a; Houborg & McCabe, 2018b).

The image pre-processing done as a part of this work highlights the considerations that must be addressed before utilising the imagery for an extensive observational data set in an automated process. As per the methods of this study, both the geometric and radiometric calibrations of the images currently have to be verified and adjusted before analysis to avoid error. Inconsistencies between individual spectral bands' registration represents a significant fidelity issue within Planet's geo-referencing process and could introduce substantial errors in any spatial analysis observing phenomena at a high-spatial resolution utilising the NIR band. While co-registering an image is considered an essential step for spatiotemporal studies (Behling et al., 2014; Scheffler et al., 2017), most co-registration processes assume bands within an image are uniformly rectified and will potentially omit a mis-registered multi-spectral band. In regards to atmospheric correction, the recently released surface reflectance product from Planet is becoming standard for the PlanetScope satellite images and improvements within its availability and consistency represent a reduced cost in pre-processing of imagery and a step closer to an automated process of shoreline extraction. On-going improvements with sensor calibration across the constellation of PlanetScope satellites will facilitate more precise results from remote sensing indices, such as the NDVI, and will aid in their applications of monitoring spatiotemporal change of the environment. Although not used as part of this study, the continued advancements within the usable data mask (UDM) offered with PlanetScope imagery will potentially allow an image to be evaluated for its suitability for feature extraction automatically and objectively.

5.4 Assessment of Scale

The results of the different time series presented in this study and the corresponding variation in the rate of change statistics (Table 14) shows that the interpretation of shoreline trends is highly dependent on the temporal scale of the observations. An accurate and informative interpretation of a long-term pattern of shoreline change requires the minimisation of errors that could be introduced with seasonal variations (Leatherman, 2003; Pajak & Leatherman, 2002) and

that the resulting accuracy of the interpretive trend increases as the historical shoreline record is expanded. The results of a longer-term shoreline change analysis provide valuable insights into the past's morphological trends and informs an investigation, such as the one presented here, as to the scale of the of shifts in the sediment budget as a result of an alteration to the environment.

The relatively shorter-term forecasting of shoreline change (intra/inter annual) is broadly based on cross-shore processes and its response to storm events and wave energy and requires higher-temporal observations, especially across rapid seasonal change. These shorter-term forecasting models are based on the association of wave forcing and cross-shore shoreline response (Davidson & Turner, 2009; Davidson et al., 2013; Splinter et al., 2011; Splinter et al., 2014; Splinter et al., 2017). The high-spatial and temporal observations sourced from CubeSat systems can provide insight into shoreline change rapidly after it has occurred, providing the satellites capture cloud-free images pre- and post-storm. These rapid observations could be utilised in shoreline prediction models that rely on sufficient calibration data, such as shoreline positions pre and post-storm event, that incorporate wave height and wave period to produce predictions of cross-shore variability (Splinter et al., 2013; Splinter et al., 2017). Equilibrium shore models (Davidson & Turner, 2009; Davidson et al., 2010, 2013; Splinter et al., 2014) as well as data driven models (Anderson et al., 2010; Karunarathna & Reeve, 2013) have been shown to be able to model shoreline response at a temporal scale of weeks to decades when provided with a temporally robust observation data set. These models are particularly useful tools for coastal managers and engineers as they provide indications of future shoreline position and help identify potentially vulnerable areas. The importance of forecasting expected shoreline change is accentuated as the effects of climate change imply an increase in both storm frequency and intensity, both drivers of shoreline erosion, that will continue to threaten the increasing coastal populations.

The localised and high spatial resolution data sets created with UAV surveys provides detailed insights into shoreline change, identifying sub-metre changes that can be used as an adaptive and responsive monitoring method for numerous applications. The deployment of UAV surveys can be used to determine the magnitude of change at a high-resolution, as done by researchers monitoring shoreline response to storm events (Casella et al., 2016; Ierodiaconou et

al., 2016; Turner et al., 2016) or integrated into longer-term coastal observational data sets that track high value sandy coasts and their evolution over time (Clark, 2017; Gonçalves & Henriques, 2015; Johannes et al., 2012; Short and Trembanis 2004; Turner et al., 2016).

6. CONCLUSIONS

A multi-temporal assessment of shoreline change in the South East of South Australia around a constructed canal estate was presented supporting the following conclusions.

The different temporal scales demonstrate the long, medium and short-term patterns of shoreline change in the region with the disruptive effect of the Cape Jaffa Marina development. The pre-marina shoreline showed a pre-dominantly accretional nature over the long-term, with the highly dynamic shoreline protrusions (sand waves) associated with the highest rates of shoreline change. In the medium term, results from the post-marina shoreline analysis shows that there have been distinct patterns of shoreline change occurring to the west and east of the constructed marina.

The results of this study confirm that compared to the pre-marina shoreline, rates of accretion and erosion have accelerated for kilometres on either side of the marina, with sediment being deposited on the western side of the marina which blocks the littoral drift and erosion down drift, to the east of the marina.

The examination of the rates of change between the two intra-annual time series, from PlanetScope imagery, showed that rates of change across the study area are significantly higher during the late autumn and winter months, corresponding to the peaks in the swell and wave energy in the region. These results confirm the observations from the literature that characterise sediment exchange rates for low wave energy beaches and provide a methods for reliable responsive monitoring.

The high spatial resolution orthomosaics created with UAV surveys and Structure from Motion photogrammetry were used to illustrate and measure the localised shoreline response to the seasonal increase of storm events via a spatiotemporal analysis. The results of this analysis show the likely migration of sand alongshore resulting in a further accretion of the shoreline to the immediate west of the Cape Jaffa Marina groynes.

The orthomosaics generated from the UAV surveys were used to validate the automatically extracted shoreline proxies from the PlanetScope imagery with the resulting comparison showing an average 1-2 pixel (3-6 metre) difference, a promising result considering spatial and temporal resolutions and its associated monetary cost. These results support the methods of automated shoreline extraction that is objectively based on image specific statistics. The developed framework presented here enables the automation of shoreline extraction and subsequent analysis of change over time in a dense time-series.

Canal estates and urban developments near the coast face a precarious future as predictions of sea-level rise, increased frequency and intensity of storms will subsequently drive higher rates of sediment transport alongshore and the coastal erosion that threaten them. The methods of remote sensing utilised here provide a means of analysing the historical past and monitoring the contemporary coastal trends of coastlines to better inform the response of coastal management.

6.1 Future Research

The continuously upgraded and expanding flock of Planet's dove satellites represents a promising potential for large-scale Earth observation. Planet's CubeSat technology, which is due to its compact nature and low cost, allows for mass deployments in multi-satellite constellations and relatively inexpensive data access at an exceptional temporal scale. Forth-coming improvements will hopefully address consistency with its atmospheric corrections, cross-sensor calibration and geo-referencing accuracy. Accounting for its inexpensive sensors that aren't able to achieve the same robust sensor calibration as larger Earth observations platforms and programs, with appropriate image pre-processing reduces significant sources of error in a multi-temporal analysis observing phenomena at a high spatial resolution. The reliable observations could be paired with contemporary wave datasets to calibrate shoreline prediction models that have been to demonstrated to accurately estimate shoreline response to storm events. A satellite prediction

service or more reliable daily imagery schedule would further facilitate ground-truthed validations like the simultaneous UAV surveys flown as part of this study.

Future work should explore the integration of the high temporal shoreline data sourced from PlanetScope imagery with the implementation of in-situ sensors that monitor near-shore currents and wave energy to calibrate shoreline prediction models. Improved Earth observation technology will facilitate new areas of research as space-based sensors provide insight into landscape level changes at a high spatial, temporal and spectral resolution. Additional areas of research should attempt to monitor and quantify the suspended sand travelling alongshore, visible in many satellite images and potentially isolatable with remote sensing methods.

BIBLIOGRAPHY

Ahmed, A, Drake, F, Nawaz, R & Woulds, C 2018, 'Where is the coast? Monitoring coastal land dynamics in Bangladesh: An integrated management approach using GIS and remote sensing techniques', *Ocean & Coastal Management*, vol. 151, pp. 10-24.

Albuquerque, MDG, Leal Alves, DC, Espinoza, JMDA, Oliveira, UR & Simões, RS 2018, 'Determining Shoreline Response to Meteo-oceanographic Events Using Remote Sensing and Unmanned Aerial Vehicle (UAV): Case Study in Southern Brazil', *Journal of Coastal Research*, vol. 85, no. sp1, pp. 766-70.

Anderson, T, Frazer, L & Fletcher, C 2015, 'Long-Term Shoreline Change at Kailua, Hawaii, Using Regularized Single Transect', *Journal of Coastal Research*, vol. 31, no. 2, pp. 464-76.

Anderson, TR, Frazer, LN & Fletcher, CH 2010, 'Transient and persistent shoreline change from a storm', *Geophysical Research Letters*, vol. 37, no. 8, pp. n/a-n/a.

Aplin, P, Atkinson, PM & Curran, PJ 1997, 'Fine spatial resolution satellite sensors for the next decade', *International Journal of Remote Sensing*, vol. 18, no. 18, pp. 3873-81.

Baptista, P, Cunha, T, Bernardes, C, Gama, C, Ferreira, Ó & Dias, A 2011, 'A Precise and Efficient Methodology to Analyse the Shoreline Displacement Rate', *Journal of Coastal Research*, vol. 27, no. 2, pp. 223-32.

Behling, R, Roessner, S, Segl, K, Kleinschmit, B & Kaufmann, H 2014, 'Robust Automated Image Co-Registration of Optical Multi-Sensor Time Series Data: Database Generation for Multi-Temporal Landslide Detection', *Remote Sensing*, vol. 6, no. 3, pp. 2572-600.

Bheeroo, RA, Chandrasekar, N, Kaliraj, S & Magesh, NSJEES 2016, 'Shoreline change rate and erosion risk assessment along the Trou Aux Biches–Mont Choisy beach on the northwest coast of Mauritius using GIS-DSAS technique', vol. 75, no. 5, p. 444.

Boak, EH & Turner, IL 2005, 'Shoreline definition and detection: a review', *Journal of Coastal Research*, vol. 21, no. 4, p. 688.

Bonifacio, R & Pisanu, P 2012, *Seagrass community of South Australia*, Department of Environment and Natural Resources, South Australia.

Bourman, RP 2016, *Coastal landscapes of South Australia*, Adelaide: The University of Adelaide Press.

Brayshaw, S & Lemckert, C 2012, 'Pitfalls of Shoreline Stabilisation – Tweed River Mouth, Gold Coast, Australia', in JAG Cooper & OH Pilkey (eds), *Pitfalls of Shoreline Stabilization: Selected Case Studies*, Springer Netherlands, Dordrecht, pp. 1-13.

Carlson, TN & Ripley, DA 1997, 'On the relation between NDVI, fractional vegetation cover, and leaf area index', *Remote Sensing of Environment*, vol. 62, no. 3, pp. 241-52.

Carrasco, AR, Ferreira, Ó, Matias, A & Freire, P 2012, 'Natural and human-induced coastal dynamics at a back-barrier beach', *Geomorphology*, vol. 159-160, pp. 30-6.

Carter, B 1988, *Coastal environments: an introduction to the physical, ecological, and cultural systems of coastlines*, London New York : Academic Press, London, New York.

Casella, E, Rovere, A, Pedroncini, A, Stark, CP, Casella, M, Ferrari, M & Firpo, M 2016, 'Drones as tools for monitoring beach topography changes in the Ligurian Sea (NW Mediterranean)', *Geo-Marine Letters*, vol. 36, no. 2, pp. 151-63.

Castelle, B, Guillot, B, Marieu, V, Chaumillon, E, Hanquiez, V, Bujan, S & Poppeschi, C 2018, 'Spatial and temporal patterns of shoreline change of a 280-km high-energy disrupted sandy coast from 1950 to 2014: SW France', *Estuarine, Coastal and Shelf Science*, vol. 200, pp. 212-23.

Čermáková, I, Komárková, J & Sedlák, P 2016, 'Using UAV to detect shoreline changes: case study–Pohranov Pond, Czech Republic', *The International Archives of Photogrammetry, Remote Sensing and Spatial Information Sciences*, vol. 41, p. 803.

Chaaban, F, Darwishe, H, Battiau-Queney, Y, Louche, B, Masson, E, Khattabi, J & Carlier, E 2012, 'Using ArcGIS registered Modelbuilder and Aerial Photographs to Measure Coastline Retreat and Advance: North of France', *Journal of Coastal Research*, vol. 28, no. 6, pp. 1567-79.

Chavez, PS 1988, 'An improved dark-object subtraction technique for atmospheric scattering correction of multispectral data', *Remote Sensing of Environment*, vol. 24, no. 3, pp. 459-79.

Chavez, PS 1996, 'Image-based atmospheric corrections-revisited and improved', *Photogrammetric Engineering and Remote Sensing*, vol. 62, no. 9, pp. 1025-35.

Chen, B, Yang, Y, Wen, H, Ruan, H, Zhou, Z, Luo, K & Zhong, F 2018, 'High-resolution monitoring of beach topography and its change using unmanned aerial vehicle imagery', *Ocean & Coastal Management*, vol. 160, pp. 103-16.

Chen, W-W & Chang, H-K 2009, 'Estimation of shoreline position and change from satellite images considering tidal variation', *Estuarine, Coastal and Shelf Science*, vol. 84, no. 1, pp. 54-60.

Clark, A 2017, 'Small unmanned aerial systems comparative analysis for the application to coastal erosion monitoring', *GeoResJ*, vol. 13, pp. 175-85.

Colomina, I & Molina, P 2014, 'Unmanned aerial systems for photogrammetry and remote sensing: A review', *ISPRS Journal of Photogrammetry and Remote Sensing*, vol. 92, pp. 79-97.

Cooley, S, Smith, L, Stepan, L & Mascaro, J 2017, 'Tracking Dynamic Northern Surface Water Changes with High-Frequency Planet CubeSat Imagery', *Remote Sensing*, vol. 9, no. 12, p. 1306.

Crowell, M, Leatherman, S & Buckley, MK 1991, 'Historical shoreline change: error analysis and mapping accuracy', *Journal of Coastal Research*, vol. 7, pp. 839-52.

Darwish, K, Smith, S, Torab, M, Monsef, H & Hussein, O 2017, 'Geomorphological Changes along the Nile Delta Coastline between 1945 and 2015 Detected Using Satellite Remote Sensing and GIS', *Journal of Coastal Research*, vol. 33, no. 4, pp. 786-94.

Davidson, MA, Lewis, RP & Turner, IL 2010, 'Forecasting seasonal to multi-year shoreline change', *Coastal Engineering*, vol. 57, no. 6, pp. 620-9.

Davidson, MA, Splinter, KD & Turner, IL 2013, 'A simple equilibrium model for predicting shoreline change', *Coastal Engineering*, vol. 73, pp. 191-202.

Davidson, MA & Turner, IL 2009, 'A behavioral template beach profile model for predicting seasonal to interannual shoreline evolution', *Journal of Geophysical Research: Earth Surface*, vol. 114, no. 1, pp. n/a-n/a.

Davidson-Arnott, R 2010, *Introduction to coastal processes and geomorphology*, 2nd ed. edn, Cambridge: Cambridge University Press, Cambridge.

Defeo, O, McLachlan, A, Schoeman, DS, Schlacher, TA, Dugan, J, Jones, A, Lastra, M & Scapini, F 2009, 'Threats to sandy beach ecosystems: A review', *Estuarine, Coastal and Shelf Science*, vol. 81, no. 1, pp. 1-12.

Del Río, L, Gracia, FJ & Benavente, J 2013, 'Shoreline change patterns in sandy coasts. A case study in SW Spain', *Geomorphology*, vol. 196, no. C, pp. 252-66.

Dhanjal-Adams, KL, Hanson, JO, Murray, NJ, Phinn, SR, Wingate, VR, Mustin, K, Lee, JR, Allan, JR, Cappadonna, JL, Studds, CE, Clemens, R, Roelfsema, CM & Fuller, RA 2016, 'The distribution and protection of intertidal habitats in Australia', *Emu - Austral Ornithology*, vol. 116, no. 2, pp. 208-14.

Dolan, R, Hayden, BP, May, P & May, S 1980, 'The reliability of shoreline change measurements from aerial photographs', *Shore and beach*, vol. 48, no. 4, pp. 22-9.

Drummond, CD, Harley, MD, Turner, IL, A Matheen, AN & Glamore, WC 2015, 'UAV applications to coastal engineering', in *Australasian Coasts & Ports Conference 2015: 22nd Australasian Coastal and Ocean Engineering Conference and the 15th Australasian Port and Harbour Conference*, p. 267.

Duffy, J, Shutler, J, Witt, M, Debell, L & Anderson, K 2018, 'Tracking Fine-Scale Structural Changes in Coastal Dune Morphology Using Kite Aerial Photography and Uncertainty-Assessed Structure-from-Motion Photogrammetry', *Remote Sensing*, vol. 10(9).

Duru, UJEM & Assessment 2017, 'Shoreline change assessment using multi-temporal satellite images: a case study of Lake Sapanca, NW Turkey', vol. 189, no. 8, p. 385.

Fisher, A, Flood, N & Danaher, T 2016, 'Comparing Landsat water index methods for automated water classification in eastern Australia', *Remote Sensing of Environment*, vol. 175, pp. 167-82.

Fletcher, C, Rooney, J, Barbee, M, Lim, S-C & Richmond, B 2003, 'Mapping shoreline change using digital orthophotogrammetry on Maui, Hawaii', *Journal of Coastal Research*, pp. 106-24.

Ford, M 2013, 'Shoreline changes interpreted from multi-temporal aerial photographs and high-resolution satellite images: Wotje Atoll, Marshall Islands', *Remote Sensing of Environment*, vol. 135, pp. 130-40.

Global Risk Report, 2019, *The global risks report 2019*, World Economic Forum.

Frazier, PS & Page, KJ 2000, 'Water body detection and delineation with Landsat TM data', *Photogrammetric Engineering and Remote Sensing*, vol. 66, no. 12, pp. 1461-8.

Geospatial, H 2018, *Rapid Atmospheric Correction*, viewed 12/09 2019, <https://hexagongeospatial.fluidtopics.net/reader/XWswM6TZr3V__hu3iKjbGA/eWxe5pKM97cbVthy4wiX5w>.

Gonçalves, JA & Henriques, R 2015, 'UAV photogrammetry for topographic monitoring of coastal areas', *ISPRS Journal of Photogrammetry and Remote Sensing*, vol. 104, pp. 101-11.

González-Villanueva, R, Costas, S, Pérez-Arlucea, M, Jerez, S & Trigo, RM 2012, 'Impact of atmospheric circulation patterns on coastal dune dynamics, NW Spain', *Geomorphology*, vol. 185, no. C.

Goward, SN, Markham, B, Dye, DG, Dulaney, W & Yang, J 1991, 'Normalized difference vegetation index measurements from the advanced very high-resolution radiometer', *Remote Sensing of Environment*, vol. 35, no. 2-3, pp. 257-77.

Gray, PC, Ridge, J, Poulin, S, Seymour, A, Schwantes, A, Swenson, J & Johnston, D 2018, 'Integrating Drone Imagery into High Resolution Satellite Remote Sensing Assessments of Estuarine Environments', *Remote Sens.*, vol. 10, no. 8.

Guisado-Pintado, E, Jackson, DWT & Rogers, D 2019, '3D mapping efficacy of a drone and terrestrial laser scanner over a temperate beach-dune zone. (Report)', *Geomorphology*, vol. 328, p. 157.

Hagenaars, G, de Vries, S, Luijendijk, AP, de Boer, WP & Reniers, AJHM 2018, 'On the accuracy of automated shoreline detection derived from satellite imagery: A case study of the sand motor mega-scale nourishment', *Coastal Engineering*, vol. 133, pp. 113-25.

Hapke, CJ, Kratzmann, MG & Himmelstoss, EA 2013, 'Geomorphic and human influence on large-scale coastal change', *Geomorphology*, vol. 199, pp. 160-70.

Harvey, N & Stocker, L 2015, 'Coastal residential waterways, science and policy-making: The Australian experience', *Estuarine, Coastal and Shelf Science*, vol. 155, pp. A1-A13.

Heine, I, Stüve, P, Kleinschmit, B & Itzerott, S 2015, 'Reconstruction of lake level changes of groundwater-fed lakes in Northeastern Germany using RapidEye time series', *Water*, vol. 7, no. 8, pp. 4175-99.

Heyligers, P 1985, 'Impact of introduced plants on foredune formation in south-eastern Australia'.

Hilton, M, Harvey, N, Hart, A, James, K & Arbuckle, C 2006, 'The Impact of Exotic Dune Grass Species on Foredune Development in Australia and New Zealand: a case study of Ammophila arenaria and Thinopyrum junceiforme', *Australian Geographer*, vol. 37, no. 3, pp. 313-34.

Himmelstoss, EA, Henderson, RE, Kratzmann, MG & Farris, AS 2018, *Digital Shoreline Analysis System (DSAS) version 5.0 user guide*, 2018-1179, Reston, VA.

Houborg, R & McCabe, M 2016, 'High-Resolution NDVI from Planet's Constellation of Earth Observing Nano-Satellites: A New Data Source for Precision Agriculture', *Remote Sens.*, vol. 8, no. 9.

Houborg, R & McCabe, MF 2018a, 'A Cubesat enabled Spatio-Temporal Enhancement Method (CESTEM) utilizing Planet, Landsat and MODIS data', *Remote Sensing of Environment*, vol. 209, pp. 211-26.

Houborg, R & McCabe, MF 2018b, 'Daily retrieval of NDVI and LAI at 3 m resolution via the fusion of CubeSat, Landsat, and MODIS data', *Remote Sensing*, vol. 10, no. 6.

Houser, C, Hapke, C & Hamilton, S 2008, 'Controls on coastal dune morphology, shoreline erosion and barrier island response to extreme storms', *Geomorphology*, vol. 100, no. 3, pp. 223-40.

Huhdanpaa, H, Hwang, D, Gasparian, G, Booker, M, Cen, Y, Lerner, A, Boyko, O, Go, J, Kim, P, Rajamohan, A, Law, M & Shiroishi, M 2014, 'Image Coregistration: Quantitative Processing Framework for the Assessment of Brain Lesions', *The Journal of the Society for Computer Applications in Radiology*, vol. 27, no. 3, pp. 369-79.

Ierodiaconou, D, Schimel, AC & Kennedy, 'A new perspective of storm bite on sandy beaches using unmanned aerial vehicles', Supplementary Issues 2016, , vol. 60, no. 3, pp. 123-37.

James, MR, Robson, S, Amp, Apos, Oleire-Oltmanns, S & Niethammer, U 2017, 'Optimising UAV topographic surveys processed with structure-from-motion: Ground control quality, quantity and bundle adjustment', *Geomorphology*, vol. 280, pp. 51-66.

Ji, L, Zhang, L & Wylie, B 2009, 'Analysis of dynamic thresholds for the normalized difference water index', *Photogrammetric Engineering & Remote Sensing*, vol. 75, no. 11, pp. 1307-17.

Johannes, BR, Irene, M, Sebastian, DO-O & Klaus Daniel, P 2012, 'Unmanned Aerial Vehicle (UAV) for Monitoring Soil Erosion in Morocco', *Remote Sensing*, vol. 4, no. 11, pp. 3390-416.

Joyce, KE, Duce, S, Leahy, SM, Leon, J & Maier, SW 2018, 'Principles and practice of acquiring drone-based image data in marine environments %J Marine and Freshwater Research', pp. -.

Kabuth, AK, Kroon, A & Pedersen, JBT 2014, 'Multidecadal Shoreline Changes in Denmark', *Journal of Coastal Research*, vol. 30, no. 4, pp. 714-28.

Karunarathna, H & Reeve, D 2013, 'A model for beach plan shape change using an inverse approach', in *Coastal Dynamics*, vol. 2013, pp. 937-46.

Kelly, JT & Gontz, AM 2018, 'Using GPS-surveyed intertidal zones to determine the validity of shorelines automatically mapped by Landsat water indices', *International Journal of Applied Earth Observations and Geoinformation*, vol. 65, pp. 92-104.

Komar, PD 1998, *Beach Processes and Sedimentation*, Prentice Hall, New Jersey, USA.

Kropáček, J, Braun, A, Kang, S, Feng, C, Ye, Q & Hochschild, V 2012, 'Analysis of lake level changes in Nam Co in central Tibet utilizing synergistic satellite altimetry and optical imagery', *International Journal of Applied Earth Observations and Geoinformation*, vol. 17, no. 1, pp. 3-11.

Lavery, P, McMahon, K, Weyers, J, Boyce, M & Oldham, C 2013, 'Release of dissolved organic carbon from seagrass wrack and its implications for trophic connectivity', *Marine Ecology Progress Series*, vol. 494, pp. 121-33.

Leatherman, SP 2003, 'Shoreline Change Mapping and Management Along the U.S. East Coast', *Journal of Coastal Research*, pp. 5-13.

Lee, J-M, Park, J-Y & Choi, J-Y 2013, 'Evaluation of Sub-aerial Topographic Surveying Techniques Using Total Station and RTK-GPS for Applications in Macrotidal Sand Beach Environment', *Journal of Coastal Research*, vol. 1, no. 65, pp. 535-40.

Lee, Y-K, Eom, J, Do, J-D, Kim, B-J & Ryu, J-H 2019, 'Shoreline Movement Monitoring and Geomorphologic Changes of Beaches Using Lidar and UAVs Images on the Coast of the East Sea, Korea', *Journal of Coastal Research*, vol. 90, no. sp1, pp. 409-14, 6.

Li, R, Ma, R & Di, K 2002, 'Digital Tide-Coordinated Shoreline', *Marine Geodesy*, vol. 25, no. 1-2, pp. 27-36.

Li, W, Du, Z, Ling, F, Zhou, D, Wang, H, Gui, Y, Sun, B & Zhang, X 2013, 'A Comparison of Land Surface Water Mapping Using the Normalized Difference Water Index from TM, ETM+ and ALI', *Remote Sensing*, vol. 5, no. 11, pp. 5530-49.

Li, W & Gong, P 2016, 'Continuous monitoring of coastline dynamics in western Florida with a 30-year time series of Landsat imagery', *Remote Sensing of Environment*, vol. 179, pp. 196-209.

Liu, H & Jezek, K 2004, 'Automated extraction of coastline from satellite imagery by integrating Canny edge detection and locally adaptive thresholding methods', *International Journal of Remote Sensing*, vol. 25, no. 5, pp. 937-58.

Liu, Y, Song, P, Peng, J & Ye, C 2012, 'A physical explanation of the variation in threshold for delineating terrestrial water surfaces from multi-temporal images: effects of radiometric correction', *International Journal of Remote Sensing*, vol. 33, no. 18, pp. 5862-75.

Lu, S, Wu, B, Yan, N & Wang, H 2011, 'Water body mapping method with HJ-1A/B satellite imagery', *International Journal of Applied Earth Observation and Geoinformation*, vol. 13, no. 3, pp. 428-34.

Mancino, G, Nole, A, Ripullone, F & Ferrara, A 2014, 'Landsat TM imagery and NDVI differencing to detect vegetation change: assessing natural forest expansion in Basilicata, southern Italy', *iForest: Biogeosciences & Forestry*, vol. 7, no. 2, pp. 75-84.

Massetti, A, Sequeira, MM, Pupo, A, Figueiredo, A, Guiomar, N & Gil, A 2016, 'Assessing the effectiveness of RapidEye multispectral imagery for vegetation mapping in Madeira Island (Portugal)', *European Journal of Remote Sensing*, vol. 49, no. 1, pp. 643-72.

Massey, LL, Johnston, JB, Paulson, O & Pessoney, GF 1976, 'Bibliography of Coastal Residential Canals with Selected Annotations'.

McFeeters, SK 1996, 'The use of the Normalized Difference Water Index (NDWI) in the delineation of open water features', *International Journal of Remote Sensing*, vol. 17, no. 7, pp. 1425-32.

Moore, L, Ruggiero, P & List, J 2006, 'Comparing mean high water and high-water line shorelines: Should proxy-datum offsets be incorporated into shoreline change analysis? (vol 22, pg 894, 2006)', *J. Coast. Res.*, vol. 22, no. 6, pp. 1452-.

Mukhopadhyay, A, Mukherjee, S, Mukherjee, S, Ghosh, S, Hazra, S & Mitra, D 2012, *Automatic shoreline detection and future prediction: A case study on Puri Coast, Bay of Bengal, India*, vol. 45.

Murray, JN, Phinn, RS, Clemens, SR, Roelfsema, MC & Fuller, AR 2012, 'Continental Scale Mapping of Tidal Flats across East Asia Using the Landsat Archive', *Remote Sensing*, vol. 4, no. 11.

Muster, S, Heim, B, Abnizova, A & Boike, J 2013, 'Water Body Distributions Across Scales: A Remote Sensing Based Comparison of Three Arctic Tundra Wetlands', *Remote Sensing*, vol. 5, no. 4, pp. 1498-523.

Nicholls, RJ, Townend, IH, Bradbury, AP, Ramsbottom, D & Day, SA 2013, 'Planning for long-term coastal change: Experiences from England and Wales', *Ocean Engineering*, vol. 71, pp. 3-16.

Nuttall, PM 1991, *Environmental effects of residential tidal canal estates, waterways and marinas in Victoria*, Deakin University.

Otsu, N 1979, 'A Threshold Selection Method from Gray-Level Histograms', *IEEE Transactions on Systems, Man, and Cybernetics*, vol. 9, no. 1, pp. 62-6.

Ozturk, D & Sesli, F 2015, *Shoreline change analysis of the Kizilirmak Lagoon Series*.

Pajak, MJ & Leatherman, S 2002, 'The high-water line as shoreline indicator', *Journal of Coastal Research*, pp. 329-37.

Planet 2018, *Planet Imagery Product Specification: Planetscope & Rapideye*, Planet.com, August 2018.

Quentin, L-F, Vincent, M, Bruno, C, Richard, M, Stéphane, B & David, R 2019, 'Low-Cost UAV for High-Resolution and Large-Scale Coastal Dune Change Monitoring Using Photogrammetry', *Journal of Marine Science and Engineering*, vol. 7, no. 3, p. 63.

Roach, JK, Griffith, B & Verbyla, D 2012, 'Comparison of three methods for long-term monitoring of boreal lake area using Landsat TM and ETM+ imagery', *Canadian Journal of Remote Sensing*, vol. 38, no. 4, pp. 427-40.

Roessler, S, Wolf, P, Schneider, T & Melzer, A 2013, 'Multispectral Remote Sensing of Invasive Aquatic Plants Using RapidEye', in JM Krisp, L Meng, R Pail & U Stilla (eds), *Earth Observation of Global Changes (EOGC)*, Springer Berlin Heidelberg, Berlin, Heidelberg, pp. 109-23.

Rouse Jr, JW, Haas, RH, Schell, J & Deering, D 1973, 'Monitoring the vernal advancement and retrogradation (green wave effect) of natural vegetation'.

Ruggerio, P, Kratzmann, MG, Himmelstoss, EA, Reid, D, Allan, J & Kaminsky, G 2013, *National assessment of shoreline change: historical shoreline change along the Pacific Northwest coast*, 2012-1007, Reston, VA.

Ruiz-Beltran, AP, Astorga-Moar, A, Salles, P, Appendini, CMJE & Coasts 2019, 'Short-Term Shoreline Trend Detection Patterns Using SPOT-5 Image Fusion in the Northwest of Yucatan, Mexico'.

Sagar, S, Roberts, D, Bala, B & Lymburner, L 2017, 'Extracting the intertidal extent and topography of the Australian coastline from a 28year time series of Landsat observations', *Remote Sensing of Environment*, vol. 195, pp. 153-69.

Scarelli, FM, Cantelli, L, Barboza, EG, Rosa, MLCC & Gabbianelli, G 2016, 'Natural and anthropogenic coastal system comparison using DSM from a low-cost UAV survey (Capão Novo, RS/Brazil)', *Journal of Coastal Research*, vol. 1, no. 75, pp. 1232-6.

Scheffler, D, Hollstein, A, Diedrich, H, Segl, K & Hostert, P 2017, 'AROSICS: An Automated and Robust Open-Source Image Co-Registration Software for Multi-Sensor Satellite Data', *Remote Sensing*, vol. 9, no. 7, p. 676.

Serafim, MB & Bonetti, J 2017, 'Vulnerabilidade das Praias do estado de santa catarina a eventos de erosão e inundação costeira: Proposta metodológica baseada em um índice multicritério', *Vulnerability of santa catarina beaches to coastal erosion and flooding: A methodological approach based on a multicriterial index*, vol. 8, no. 2, pp. 36-54.

Short, A & Hesp, P 1980, *Coastal Engineering and Mophodynamic Assessment of the Coast within the South East Coast Protection District South Australia*.

Short, AD, Hesp, P.A. 1984, *Beach and dune morphodynamics of the South East coast of South Australia*, Sydney: Dept. of Geography, University of Sydney, Sydney.

Short, AD 2019, *Australian Coastal Systems*, Cham, Switzerland.

Silva, R, Martnez, ML, Hesp, PA, Catalan, P, Osorio, AF, Martell, R, Fossati, M, Miot da Silva, G, Mario-Tapia, I, Pereira, P, Cienguegos, R, Klein, A & Govaere, G 2014, 'Present and Future Challenges of Coastal Erosion in Latin America', *Journal of Coastal Research*, vol. 71, no. sp1, pp. 1-16.

Song, C, Woodcock, CE, Seto, KC, Lenney, MP & Macomber, SA 2001, 'Classification and Change Detection Using Landsat TM Data: When and How to Correct Atmospheric Effects?', *Remote Sensing of Environment*, vol. 75, no. 2, pp. 230-44.

Splinter, K, Davidson, MA & Turner, I 2013, 'Monitoring data requirements for shoreline prediction: How much, how long, and how often?', *J. Coast. Res.*, vol. 65, no. sp2, pp. 2179-84.

Splinter, KD, Holman, RA & Plant, NG 2011, 'A behavior-oriented dynamic model for sandbar migration and 2DH evolution', *Journal of Geophysical Research: Oceans*, vol. 116, no. C1, pp. n/a-n/a.

Splinter, KD, Turner, IL, Davidson, MA, Barnard, P, Castelle, B & Oltman-Shay, J 2014, 'A generalized equilibrium model for predicting daily to interannual shoreline response', *Journal of Geophysical Research: Earth Surface*, vol. 119, no. 9, pp. 1936-58.

Splinter, KD, Turner, IL, Reinhardt, M & Ruessink, G 2017, 'Rapid adjustment of shoreline behavior to changing seasonality of storms: observations and modelling at an open-coast beach', *Earth Surface Processes and Landforms*, vol. 42, no. 8, pp. 1186-94.

Stocker, L, Harvey, N & Metcalf, SJ 2016, 'Management of coastal canal estates in Australia: Challenges and opportunities', *Ocean & Coastal Management*, vol. 130, pp. 148-61.

Stratoulias, D, Tolpekin, V, De By, R, Zurita-milla, R, Retsios, V, Bijker, W, Hasan, M & Vermote, E 2017, 'A Workflow for Automated Satellite Image Processing: from Raw VHSR Data to Object-Based Spectral Information for Smallholder Agriculture', *Remote Sensing*, vol. 9, no. 10, pp. urn:issn:2072-4292.

Sytnik, O, Del Río, L, Greggio, N & Bonetti, J 2018, 'Historical shoreline trend analysis and drivers of coastal change along the Ravenna coast, NE Adriatic', *Environmental Earth Sciences*, vol. 77, no. 23, pp. 1-20.

Thieler, ER, Himmelstoss, EA, Zichichi, JL & Ergul, A 2009, *The Digital Shoreline Analysis System (DSAS) Version 4.0 - An ArcGIS extension for calculating shoreline change*, 2008-1278, Reston.

Tsokos, A, Kotsi, E, Petrakis, S & Vassilakis, E 2018, 'Combining series of multi-source high spatial resolution remote sensing datasets for the detection of shoreline displacement rates and the effectiveness of coastal zone protection measures', *Planning and Management*, vol. 22, no. 2, pp. 431-41.

Turner, I, Harley, M & Drummond, C 2016, 'UAVs for coastal surveying', *Coastal Engineering*, vol. 114, pp. 19-24.

Turner, IL, Aarninkhof, SG & Holman, RA 2006, 'Coastal imaging applications and research in Australia', *Journal of Coastal Research*, pp. 37-48.

Valderrama-Landeros, L, Flores-de-Santiago, F, Kovacs, JM & Flores-Verdugo, F 2017, 'An assessment of commonly employed satellite-based remote sensors for mapping mangrove species in Mexico using an NDVI-based classification scheme', *Environmental Monitoring and Assessment*, vol. 190, no. 1, p. 23.

van Leeuwen, WJD, Orr, BJ, Marsh, SE & Herrmann, SM 2006, 'Multi-sensor NDVI data continuity: Uncertainties and implications for vegetation monitoring applications', *Remote Sensing of Environment*, vol. 100, no. 1, pp. 67-81.

Vos, K, Harley, MD, Splinter, KD, Simmons, JA & Turner, IL 2019, 'Sub-annual to multi-decadal shoreline variability from publicly available satellite imagery', *Coastal Engineering*, vol. 150, pp. 160-74.

Westman, WE 1975, 'Ecology of canal estates', *Search*, vol. 6, no. 11-1, pp. 491-7.

Wicaksono, P & Hafizt, M 2018, 'Dark target effectiveness for dark-object subtraction atmospheric correction method on mangrove above-ground carbon stock mapping', *IET Image Processing*, vol. 12, no. 4, pp. 582-7.

Wicaksono, P & Lazuardi, W 2018, 'Assessment of PlanetScope images for benthic habitat and seagrass species mapping in a complex optically shallow water environment', *International Journal of Remote Sensing*, vol. 39, no. 17, pp. 5739-65.

Work, E & Gilmer, DS 1976, 'Utilization of satellite data for inventorying prairie ponds and lakes', *Photogrammetric Engineering and Remote Sensing*, vol. 42, no. 5, pp. 685-94.

Wright, LD & Short, AD 1984, 'Morphodynamic variability of surf zones and beaches: A synthesis', *Marine Geology*, vol. 56, no. 1, pp. 93-118.

Wright, LD & Thom, BG 1977, 'Coastal depositional landforms: a morphodynamic approach', vol. 1, no. 3, pp. 412-59.

Wulder, MA, White, JC, Niemann, KO & Nelson, T 2004, 'Comparison of airborne and satellite high spatial resolution data for the identification of individual trees with local maxima filtering', *International Journal of Remote Sensing*, vol. 25, no. 11, pp. 2225-32.

Xiao, X, Braswell, B, Zhang, Q, Boles, S, Frolking, S & Moore, B 2003, 'Sensitivity of vegetation indices to atmospheric aerosols: continental-scale observations in Northern Asia', *Remote Sensing of Environment*, vol. 84, no. 3, pp. 385-92.

Yang, B, Hawthorne, TL, Torres, H & Feinman, M 2019, 'Using Object-Oriented Classification for Coastal Management in the East Central Coast of Florida: A Quantitative Comparison between UAV, Satellite, and Aerial Data', *Drones*, vol. 3, no. 3, p. 60.

Zhai, K, Wu, X, Qin, Y & Du, P 2015, 'Comparison of surface water extraction performances of different classic water indices using OLI and TM imageries in different situations', *Geo-spatial Information Science*, vol. 18, no. 1, pp. 32-42.

Zhou, Y & Michalak, AM 2009, 'Characterizing attribute distributions in water sediments by geostatistical downscaling', *Environmental science & technology*, vol. 43, no. 24, pp. 9267-73.

APPENDICES

Appendix 1:

Shoreline Concept Definition in the Literature:

The shoreline is one part of the larger coastal zone that is broadly and imprecisely defined. Davidson-Arnott (2010, p. 11) explains that the definition is broadly termed to allow its overview to address the large geographic region that is influenced by its processes. Following the work of previous coastal change research (Dolan et al., 1980), shorelines can be interpreted as a dynamic boundary between water and land surfaces which can be used as an indicator for analysing the morphological trends of a study area. Boak and Turner (2005) further suggest that due to the inherently dynamic nature of coasts any definition must consider its spatial variability across a temporal scale according to the context and conditions of the study area. Some researchers have found that the most consistent shoreline indicator for their study area was the edge of vegetation or the limit between the upper beach and the vegetated foredune (Anderson et al., 2015; Baptista et al., 2011; Castelle et al., 2018; Chaaban et al., 2012; Ford, 2013; Kabuth et al., 2014). Other studies have utilised the High Water Line or Instantaneous Water Line (IWL) for sandy beaches as their defined shoreline due to the presence of indicators such as the wet/dry line that is identifiable in field work, aerial photographs and satellite imagery (Bheeroo, 2016; Hapke, 2013; Houser et al., 2008; Kelly et al., 2018; Leatherman, 2003; Moore et al., 2006; Pajak & Leatherman, 2002; Ruggerio, 2013; Sytnik et al., 2018). The IWL is considered the most widely used shoreline indicator and is generally defined as the last high tide mark visible within imagery (Del Rio, 2013). Additionally, the IWL has been shown by researchers to be a good indicator of shoreline in micro-tidal and low slope beaches (Crowell et al., 1991; Ruiz-Beltran et al., 2019; Serafim & Bonetti, 2017; Sytnik et al., 2018).

Image Pre-Processing

Before analysis could be done on individual images, images were pre-processed using atmospheric, radiometric and geometric correction techniques. The pre-processing of imagery is an integral part of remote sensing studies because it minimises the varying temporal effects of atmosphere (Houborg & McCabe, 2018a; Massetti et al., 2016; Stratoulias et al., 2017; Wicaksono & Lazuardi, 2018; Wicaksono & Hafizt, 2018) and the differences between geometric rectification of satellite imagery (Behling et al., 2014; Chen et al., 2018; Heine et al., 2015; Huhdanpaa et al., 2014; Kropáček et al., 2012; Roessler et al., 2013; Ruiz-Beltran et al., 2019; Scheffler et al., 2017; Stratoulias et al., 2017). The atmospheric effects within imagery are a result of the scattering of electromagnetic radiation as it passes through the Earth's atmosphere, resulting in disproportionate effects within the shorter and visible wave lengths of RGB (Red, Green and Blue) and NIR (Liu et al., 2012; Wicksono & Hafizt, 2018). Similarly, the geometric correction of

orthorectified satellite imagery requires addressing the displacements that exist between images as a result of inter or intra-sensoral mis-registration (Scheffler et al., 2017). The co-registering of a time series of images adjusts all images with a master image, either in an automated process as shown in the work of Scheffler et al., (2017) or by an operator per individual image (Ruiz-Beltran et al., 2019). This step ensures that change detection analysis does not register error between data sets as physical change of the study site (Behling et al., 2014).

Image Analysis

After the effects of atmosphere have been minimised and the spatial reference between images has been standardised, image analysis provides methods for identifying landscape features based on their spectral signatures. Various studies have utilised the characteristic properties of the NIR band to extract water boundaries from satellite imagery (Liu et al., 2012) and to monitor vegetation change. One popular indices for terrestrial waterline extraction is the Normalised Difference Water Index (NDWI) as shown by its extensive use across the literature (Cooley et al., 2017; Darwish et al., 2017; Duru, 2017; Fisher et al., 2016; Ji et al., 2009; Ozturk & Sesli, 2015; Sagar et al., 2017). The NDWI index was developed by McFeeters (1996), who exemplified the relationship between the green and NIR bands (equation 1), which provides a standardised value between -1 and 1 where open water pixel values approach 1 (Cooley et al., 2017). Other researchers (Heine et al., 2015; Kropáček et al., 2012; Muster et al., 2013; Tsokos et al., 2018; Work & Gilmer, 1976) have found that the properties of the NIR band alone could effectively distinguish the land water boundary. The NIR band is almost completely absorbed by water bodies (Muster et al., 2013) and provides a simple method that has been shown to produce similar results of extracting the water line boundary compared with multi-spectral classifications (Frazier & Page, 2000; Muster et al., 2013; Roach et al., 2012).

Multi-spectral satellite imagery has been utilised for monitoring vegetation change and extracting the extent of water bodies with the use of the Normalised Difference Vegetation Index (NDVI) (Carlson & Ripley, 1997; Goward et al., 1991; Houborg & McCabe, 2018b; Massetti et al., 2016; Valderrama-Landeros et al., 2017; Van Leeuwen et al., 2006; Wicaksono & Hafizt, 2018; Xiao et al., 2003; Yang et al., 2019). The ratio of the NIR and Red bands, as shown in Equation 2, is normalised and provides a numerical range of vegetation vigour (Rouse et al., 1973), where pixels over open water approach -1 and vigorous vegetation approaches 1 (Yang et al., 2019). The index is a well-established indicator within remote sensing studies of both short- and long-term studies of vegetation change (Yang et al., 2019; Zhou et al., 2009) and has been utilised in studies for shoreline extraction (Mukhopadhyay et al., 2012).

Appendix 2: Python Scripts

TOA Radiance to TOA Reflectance

```
import arcpy
from xml.dom import minidom

# To allow overwriting the outputs change the overwrite option to true.
arcpy.env.overwriteOutput = True
#input files
inputImage = arcpy.GetParameterAsText(0)
metadataFile = arcpy.GetParameterAsText(1)
#output files
compositeBands = arcpy.GetParameterAsText(2)
scale = 10000
#extract individual bands
arcpy.MakeRasterLayer_management(in_raster=inputImage, out_rasterlayer="oNIR",
band_index="4")
arcpy.MakeRasterLayer_management(in_raster=inputImage, out_rasterlayer="oRed",
band_index="3")
arcpy.MakeRasterLayer_management(in_raster=inputImage, out_rasterlayer="oGreen",
band_index="2")
arcpy.MakeRasterLayer_management(in_raster=inputImage, out_rasterlayer="oBlue",
band_index="1")

#read metadata file looking for kwargs
xmlDoc = minidom.parse(metadataFile)
nodes = xmlDoc.getElementsByTagName("ps:bandSpecificMetadata")
# XML parser refers to bands by numbers 1-4
coeffs = {}
for node in nodes:
    bn = node.getElementsByTagName("ps:bandNumber")[0].firstChild.data
    if bn in ['1', '2', '3', '4']:
        i = int(bn)
        value = node.getElementsByTagName("ps:reflectanceCoefficient")[0].firstChild.data
        coeffs[i] = float(value)

#Scales TOP of Atmosphere radiance to TOA reflectance via metadata values
reflectanceNIR = arcpy.sa.Times("oNIR", coeffs[4])
scaledReflectanceNIR = arcpy.sa.Times(reflectanceNIR, scale)
reflectanceRed = arcpy.sa.Times("oRed", coeffs[3])
scaledReflectanceRed = arcpy.sa.Times(reflectanceRed, scale)
reflectanceGreen = arcpy.sa.Times("oGreen", coeffs[2])
scaledReflectanceGreen = arcpy.sa.Times(reflectanceGreen, scale)
reflectanceBlue = arcpy.sa.Times("oBlue", coeffs[1])
scaledReflectanceBlue = arcpy.sa.Times(reflectanceBlue, scale)

#output
arcpy.CompositeBands_management([scaledReflectanceBlue,scaledReflectanceGreen,scaledRefl
ectanceRed,scaledReflectanceNIR], compositeBands)
```

TOA Reflectance to Dark Object Subtraction Image

```
import arcpy
```

```
from arcpy import env
from arcpy.sa import *


# To allow overwriting the outputs change the overwrite option to true.
arcpy.env.overwriteOutput = True
#input images
inputImage = arcpy.GetParameterAsText(0)
arcpy.env.extent = inputImage
#takes input floats from ArcGIS Pro as text
dosValueNIR = float(arcpy.GetParameterAsText(1))
dosValueRed = arcpy.GetParameterAsText(2)
dosValueGreen = arcpy.GetParameterAsText(3)
dosValueBlue = arcpy.GetParameterAsText(4)
compositeBands = arcpy.GetParameterAsText(5)

#extracts bands, makes new layer
arcpy.MakeRasterLayer_management(in_raster=inputImage, out_rasterlayer="oNIR",
band_index="4")
arcpy.MakeRasterLayer_management(in_raster=inputImage, out_rasterlayer="oRed",
band_index="3")
arcpy.MakeRasterLayer_management(in_raster=inputImage, out_rasterlayer="oGreen",
band_index="2")
arcpy.MakeRasterLayer_management(in_raster=inputImage, out_rasterlayer="oBlue",
band_index="1")

#creates constant raster from Arcpy
outContRasterNIR = CreateConstantRaster(dosValueNIR, "FLOAT", 3)
outContRasterRed = CreateConstantRaster(float(dosValueRed), "FLOAT", 3)
outContRasterGreen = CreateConstantRaster(float(dosValueGreen), "FLOAT", 3)
outContRasterBlue = CreateConstantRaster(float(dosValueBlue), "FLOAT", 3)

#dark object subtraction
dosNIR = "oNIR" - outContRasterNIR
dosRed = "oRed" - outContRasterBlue
dosGreen = "oGreen" - outContRasterGreen
dosBlue = "oBlue" - outContRasterBlue

#output
arcpy.CompositeBands_management([dosBlue,dosGreen,dosRed,dosNIR], compositeBands)
```

Surface Reflectance image to Shoreline Vectors, Edge of Vegetation and Water Line

```
import arcpy

from xml.dom import minidom
from arcpy import env
from arcpy.sa import *


# To allow overwriting the outputs change the overwrite option to true.
arcpy.env.overwriteOutput = True
#environment
arcpy.env.workspace = r"C:\Workspace\NDVI\NDVI.gdb"
```

```
#input Image
inputImage = arcpy.GetParameterAsText(0)
#output shorelines
outputNDVIline = arcpy.GetParameterAsText(1)
outputWaterline = arcpy.GetParameterAsText(2)

#extracts image, 5 bands per RapidEye.Planet has same process with changed code here for 4
layers
arcpy.MakeRasterLayer_management(in_raster=inputImage, out_rasterlayer="oNIR",
band_index="5")
arcpy.MakeRasterLayer_management(in_raster=inputImage, out_rasterlayer="oRedEdge",
band_index="4")
arcpy.MakeRasterLayer_management(in_raster=inputImage, out_rasterlayer="oRed",
band_index="3")
arcpy.MakeRasterLayer_management(in_raster=inputImage, out_rasterlayer="oGreen",
band_index="2")
arcpy.MakeRasterLayer_management(in_raster=inputImage, out_rasterlayer="oBlue",
band_index="1")



# Extract by mask to shoreline area
arcpy.gp.ExtractByMask_sa("oNIR", "ShorelineExtractFinal", "NIR")
arcpy.gp.ExtractByMask_sa("oRedEdge", "ShorelineExtractFinal", "RedEdge")
arcpy.gp.ExtractByMask_sa("oRed","ShorelineExtractFinal", "Red")
arcpy.gp.ExtractByMask_sa("oGreen", "ShorelineExtractFinal", "Green")
arcpy.gp.ExtractByMask_sa("oBlue", "ShorelineExtractFinal", "Blue")
arcpy.CopyRaster_management("NIR","NIRcopy1")
#scales values to make float
NIR = arcpy.sa.Times("NIR", 1.0)
RedEdge = arcpy.sa.Times("RedEdge", 1.0)
Red = arcpy.sa.Times("Red", 1.0)
Green = arcpy.sa.Times("Green", 1.0)
Blue = arcpy.sa.Times("Blue", 1.0)
#NIR Binary Thresholding based off Otsu

#steps back to access Raster Function
arcpy.env.workspace = r"C:\Workspace\NDVI"

#access raster function
Binary_Thresholding_Function = "Binary Thresholding.rft"
#must take input as mosaic dataset
arcpy.management.CreateMosaicDataset(r"C:\Workspace\NDVI\NDVI.gdb", "NIRMDS",
"PROJCS['WGS_1984_UTM_Zone_54S',GEOGCS['GCS_WGS_1984',DATUM['D_WGS_1984',S
PHEROID['WGS_1984',6378137.0,298.257223563]],PRIMEM['Greenwich',0.0],UNIT['Degree',0.01
74532925199433]],PROJECTION['Transverse_Mercator'],PARAMETER['False_Easting',500000.0]
,PARAMETER['False_Northing',10000000.0],PARAMETER['Central_Meridian',141.0],PARAMETE
R['Scale_Factor',0.9996],PARAMETER['Latitude_Of_Origin',0.0],UNIT['Meter',1.0]]", None, None,
"NONE", None)
arcpy.management.AddRastersToMosaicDataset(r"C:\Workspace\NDVI\NDVI.gdb\NIRMDS",
"Raster Dataset", r"C:\Workspace\NDVI\NDVI.gdb\NIR", "UPDATE_CELL_SIZES",
"UPDATE_BOUNDARY", "NO_OVERVIEWS", None, 0, 1500, None, None, "SUBFOLDERS",
"ALLOW_DUPLICATES", "NO_PYRAMIDS", "NO_STATISTICS", "NO_THUMBNAILS", None,
"NO_FORCE_SPATIAL_REFERENCE", "NO_STATISTICS", None, "NO_PIXEL_CACHE",
r"C:\Users\dasi0027\AppData\Local\ESRI\rasterproxies\NIRMDS")
#sets workspace back to GDB
```

```
arcpy.env.workspace = r"C:\Workspace\NDVI\NDVI.gdb"
#utilises ArcGIS pro raster function Binary Thresholding
arcpy.management.EditRasterFunction("NIRMDS", "EDIT_MOSAIC_DATASET", "INSERT",
r"C:\Workspace\NDVI\Binary Thresholding.rft.xml", "Mosaic Function")
arcpy.management.CopyRaster("NIRMDS", "NIRcopy", None, None, 255, "NONE", "NONE",
None, "NONE", "NONE", "GRID", "NONE")
#reclassifies water as nodata and land as 1
arcpy.ddd.Reclassify("NIRcopy", "VALUE", "1 1", "NIR1", "NODATA")
#cleans up excess noise
arcpy.gp.MajorityFilter_sa("NIR1","NIR2","FOUR","HALF")
arcpy.gp.BoundaryClean_sa("NIR2","NIR3","NO_SORT", "TWO_WAY")
arcpy.gp.MajorityFilter_sa("NIR3","NIRMajFilt","FOUR","HALF")
#converts to polygon
arcpy.RasterToPolygon_conversion("NIRMajFilt", "NIRpolygonFeature", "SIMPLIFY","VALUE",
"SINGLE_OUTER_PART", "")
arcpy.cartography.SmoothPolygon("NIRpolygonFeature", "NIRpolygonFeature1" , "PAEK", "20
Meters", "FIXED_ENDPOINT", "NO_CHECK", None)
arcpy.PolygonToLine_management("NIRpolygonFeature1",
"waterLineRE","IGNORE_NEIGHBORS")

#NDVI
ResultOfMinusNDVI = arcpy.sa.Minus(NIR, Red)

#Add it together
ResultOfPlusNDVI = arcpy.sa.Plus(NIR, Red)

#Divide the two: NDVI output
NDVI_RawOutput = arcpy.sa.Divide(ResultOfMinusNDVI, ResultOfPlusNDVI)

# Process: Copy Raster
arcpy.CopyRaster_management(NDVI_RawOutput,"NDVITest")
arcpy.CopyRaster_management(NDVI_RawOutput,"NDVIEVeg")
## Process: Reclassify

arcpy.gp.ExtractByMask_sa("NDVITest", "NIR3", "NDVIExtracted")
arcpy.gp.IsoClusterUnsupervisedClassification_sa("NDVIExtracted","4","IsoClusterUnsup","20","10
","sigFile")




arcpy.Reclassify_3d("IsoClusterUnsup","VALUE","1 NODATA;2 2;3 2;4
2","Reclass_NDVI","NODATA")
## Process: Majority Filter
arcpy.gp.MajorityFilter_sa("Reclass_NDVI","Majorit_Recl2","FOUR","HALF")

## Process: Boundary Clean (2)

## Process: Raster to Polygon (2)
arcpy.RasterToPolygon_conversion("Majorit_Recl2", "polygonFeature", "SIMPLIFY","VALUE",
"SINGLE_OUTER_PART", "")

##Adds field, calculates area, eliminates those below threshold.
arcpy.AddField_management("polygonFeature","Area", "Long")
arcpy.CalculateGeometryAttributes_management("polygonFeature", [["Area", "AREA"]], "",
"SQUARE_METERS")
arcpy.EliminatePolygon_topographic("polygonFeature", "polygonFeature", "30000 SquareMeters" )
```

```
arcpy.cartography.SmoothPolygon("polygonFeature", "polygonFeature1" , "PAEK", "20 Meters",
"FIXED_ENDPOINT", "NO_CHECK", None)

arcpy.PolygonToLine_management("polygonFeature1", "NDVILine","IGNORE_NEIGHBORS")


arcpy.management.SplitLineAtPoint("waterLineRE", "splitPoint",  "WaterLineSplit", "10 Meters")
arcpy.management.SplitLineAtPoint("NDVILine", "splitPoint", "NDVILineSplit", "10 Meters")

arcpy.MakeFeatureLayer_management("NDVILineSplit", "NDVIFLayer")
arcpy.MakeFeatureLayer_management("WaterLineSplit", "waterFLayer")

arcpy.management.SelectLayerByAttribute("NDVIFLayer", "NEW_SELECTION", "Shape_Length >
500", None)
arcpy.management.SelectLayerByAttribute("waterFLayer", "NEW_SELECTION", "Shape_Length >
500", None)

arcpy.CopyFeatures_management("NDVIFLayer", "outputNDVILineSplit")
arcpy.CopyFeatures_management("waterFLayer", "outputWaterLineSplit")

arcpy.management.UnsplitLine("outputNDVILineSplit", "NDVIFinalLine", None, None)
arcpy.management.UnsplitLine("outputWaterLineSplit", "waterFinalLine", None, None)


arcpy.CopyFeatures_management("NDVIFinalLine", outputNDVIline)
arcpy.CopyFeatures_management("waterFinalLine", outputWaterline)
```

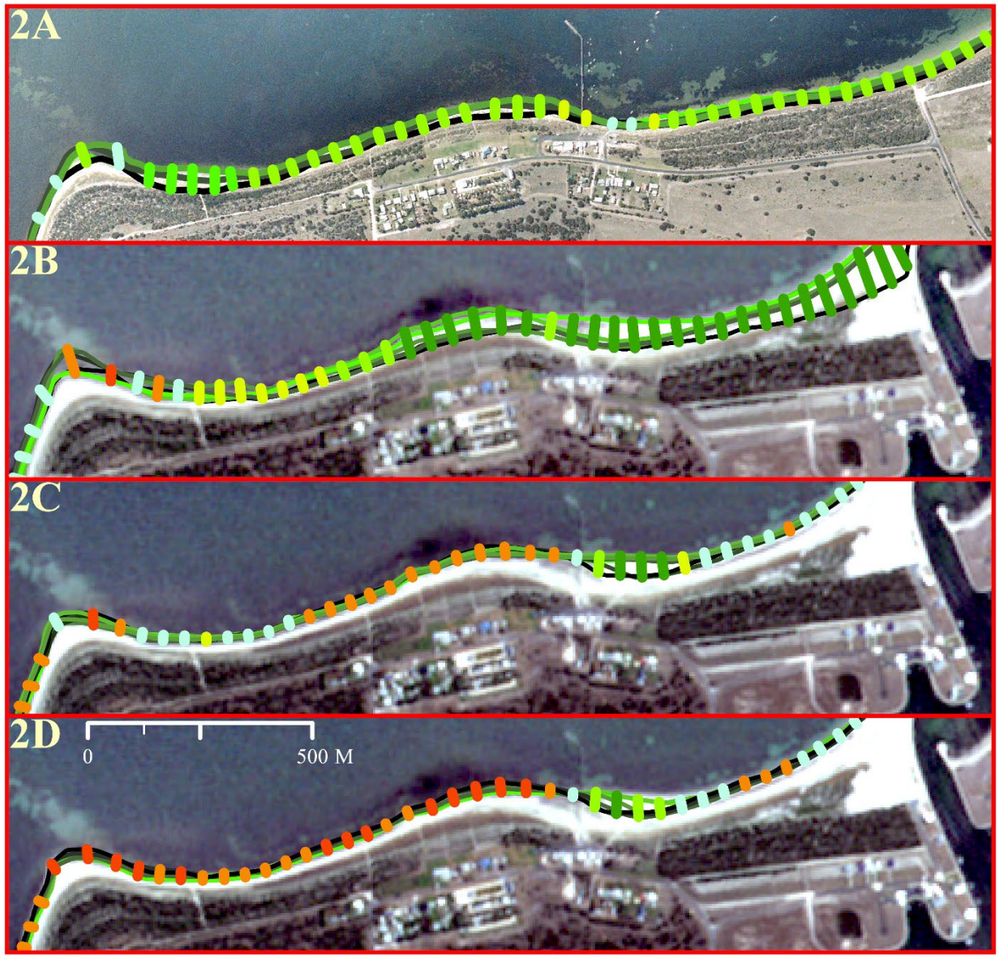
2A
2B
2C
2D
0
500 M

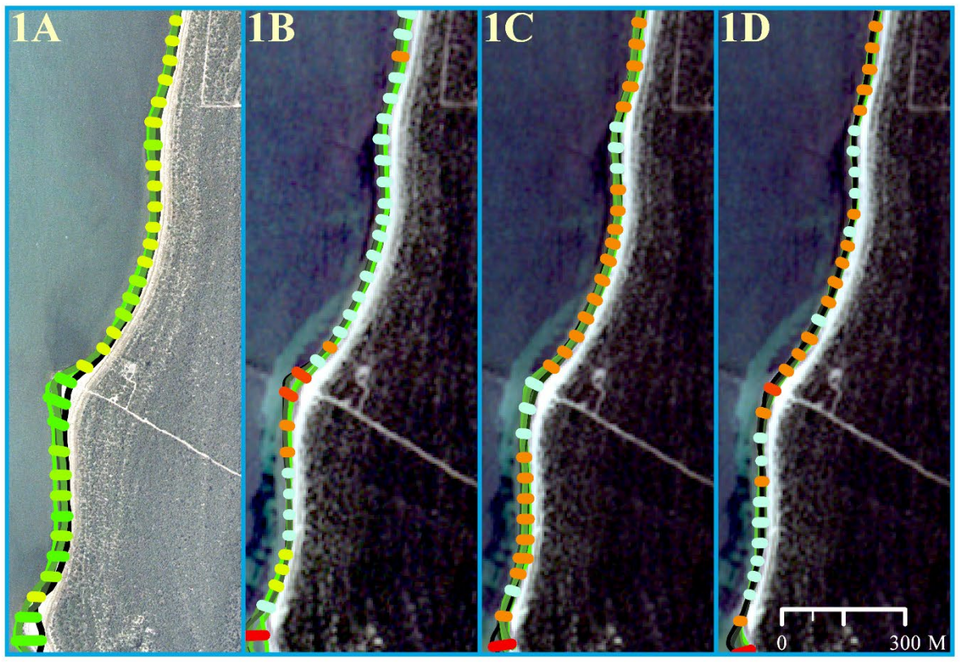
1A
1B
1C
1D
0
300 M

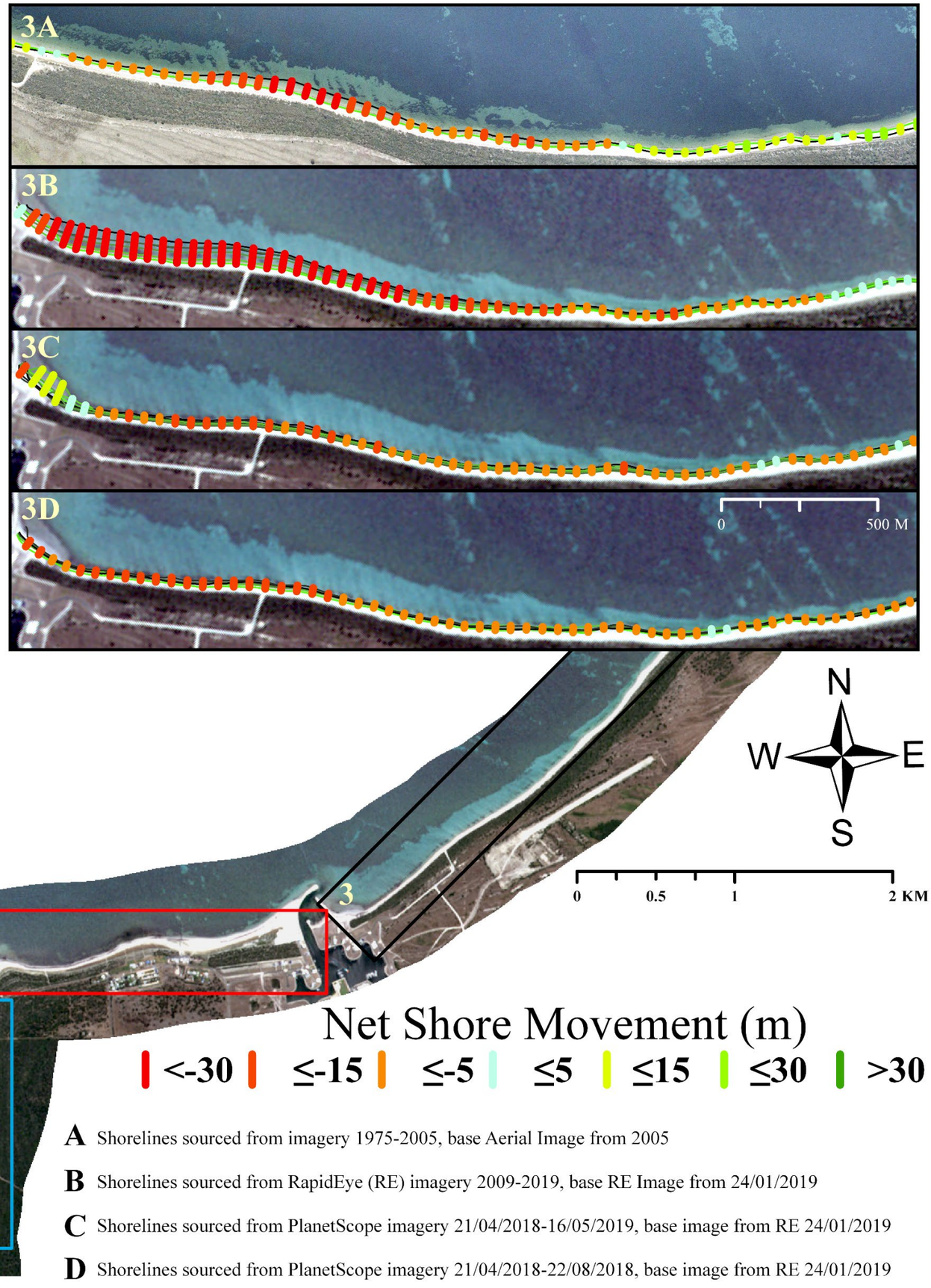
3A
3B
3C
3D
0
500 M
N
W
E
S
0
0.5
1
2 KM
1
2
3
Net Shore Movement (m)
<-30
≤-15
≤-5
≤5
≤15
≤30
>30
A Shorelines sourced from imagery 1975-2005, base Aerial Image from 2005
B Shorelines sourced from RapidEye (RE) imagery 2009-2019, base RE Image from 24/01/2019
C Shorelines sourced from PlanetScope imagery 21/04/2018-16/05/2019, base image from RE 24/01/2019
D Shorelines sourced from PlanetScope imagery 21/04/2018-22/08/2018, base image from RE 24/01/2019